2024

# Neuron-astrocyte calcium dynamics in fear learning and memory

BOSTON UNIVERSITY

ARAM V. CHOBANIAN & EDWARD AVEDISIAN SCHOOL OF MEDICINE

Dissertation

# NEURON-ASTROCYTE CALCIUM DYNAMICS IN FEAR LEARNING AND MEMORY

by

**REBECCA L. SUTHARD**

B.S., Boston College, 2019

Submitted in partial fulfillment of the

requirements for the degree of

Doctor of Philosophy

2024

Approved by

First Reader

Steve Ramirez, Ph.D.
Assistant Professor of Psychological & Brain Sciences

Second Reader

Hengye Man, M.D. Ph.D.
Professor of Biology
Professor of Pharmacology & Experimental Therapeutics

Third Reader

Heidi Meyer, Ph.D.
Assistant Professor of Psychological & Brain Sciences

## ACKNOWLEDGMENTS

I would like to express my deepest gratitude to my advisor Dr. Steve Ramirez for his unwavering support, kindness, and trust in me throughout my doctoral journey. Thank you for fostering a safe, welcoming and comedic environment that made my academic journey genuinely enjoyable, I am so grateful for your mentorship. Thank you for taking a chance on me as a graduate student and allowing me to pursue astrocyte research in your lab, it truly changed the trajectory of my career for the better and pushed us both our of our comfort zones. A special thank you to the entire Ramirez Lab for all of your science advice, moral support, conference antics and laughs over the past few years.

I am also grateful to the members of my dissertation advisory committee: Dr. Hengye Man, Dr. Heidi Meyer, Dr. Mark Howe and Dr. Michael McDannald for your insightful feedback on my projects and manuscripts, as well as your ongoing encouragement. Further, I would like to thank the Graduate Program for Neuroscience community, including my cohort (Jackie, Joselyne, Will, Quan, Naomi, Ellie, Nicole, Caroline, Zinong), Dr. Shelley Russek, Dr. Sandra Grasso and all of the administrative staff over the years for their support, guidance and friendship – especially over Zoom during the pandemic. I would like to express my appreciation to the funding agencies, institutions, and organizations that have supported my research, specifically the Ludwig Family Foundation.

Thank you to all of the amazing undergraduate students and technicians I have worked with over the years, Michelle Buzharsky, Angela Pyo, Alex Jellinger, Michelle

Surets, Mia Diep, Siria Coello. You are all such amazing people and scientists, and I cannot thank you enough for your time, hard work and for being some of the funniest people I have ever met. It has been an absolute honor being your mentor and I will miss you all immensely.

I would like to thank my roommates, Shannon and Kaitlyn, for being the most amazing friends and support system outside of work, and my cat Rory, for keeping us all on our toes. Thank you to my family, specifically my Dad, my aunt Susan and uncle Scott, my aunt Karen and my brother, for the lifelong investment in me as a person and constant support during my academic journey. Finally, a special thank you to Ryan, for being my astrocyte partner-in-crime, the computational other half of these projects and my partner in life – I am so grateful for you. And to the rest of your household, Zach and the cats, Glia, Jeff and Frasier, thank you for listening to us talk about science all the time and for providing emotional support.

Most importantly, I want to acknowledge the use of animals as part of this work, and I wholeheartedly thank each and every mouse for sacrificing their lives to science. It was a pleasure taking care of them and ensuring their time with us was full of as much comfort and joy as possible.

**NEURON-ASTROCYTE CALCIUM DYNAMICS IN FEAR LEARNING AND MEMORY**

**REBECCA L. SUTHARD**

Boston University Aram V. Chobanian & Edward Avedisian School of Medicine, 2024

Major Professor: Steve Ramirez, Ph.D., Professor of Psychological and Brain Sciences

## ABSTRACT

Memory is one of the most extensively-studied phenomenon in neuroscience as it provides the basis for our day-to-day human experience. A continued unmet need is understanding how memory processing can go wrong, whether in the degeneration of our ability to form or access memories (i.e. dementia) or in maladaptive memory processing (i.e. Post-Traumatic Stress Disorder). Animal models have enabled tremendous insight into the molecular and systems-level underpinnings of healthy and pathological memory states that advance our understanding of the human condition. Within the memory field, the primary focus has traditionally been on how neuronal activity within regions such as the hippocampus enable the formation, consolidation, maintenance, and extinction of episodic memories, i.e. the memories of our personally experienced events defined along what-where-when dimensions. While the majority of this work has focused on neurons despite extensive work indicating that memories recruit heterogenous cell types, recent work has supported the idea that astrocytes, a type of glial cell, are active modulators of learning and memory processes ranging from fear encoding to spatial navigation. To expand upon this growing literature, we investigated the role of astrocytic calcium dynamics using multiple imaging modalities within the amygdala and hippocampus, in an effort to understand how

they may be intimately interacting with neurons to enable higher-level cognitive processing.

To that end, my thesis puts forth three experiments that link the activity of neurons and astrocytes to cognition and behavior. In the first experiment, we recorded real-time astrocytic calcium dynamics in the basolateral amygdala (BLA) across contextual fear conditioning (CFC), recall and extinction using single-color fiber photometry. We showed that BLA astrocytes robustly responded to foot shock during CFC, resulting in persistent changes in calcium activity across subsequent days compared to controls. Additionally, astrocytic calcium dynamics became correlated with freezing epochs during CFC and recall only in mice that received foot shocks, and this activity became uncoupled across extinction days. Further, chemogenetic inhibition of BLA fear ensembles had no effect on astrocytic calcium activity or freezing behavior. The results of our first experiment revealed that astrocytes play a real-time role in the acquisition and maintenance of contextual fear as it relates to behavior. Our second experiment then sought to understand how artificial stimulation of fear affects intra-hippocampal neuron-astrocyte dynamics as well as their behavioral consequences. Here, we utilized a combination of activity-dependent labeling strategies in the dentate gyrus (DG) and *in vivo* fiber photometry of neurons and astrocytes in ventral CA1 of the hippocampus (vCA1) across fear acquisition, natural recall and artificial reactivation of a fear memory or *engram*. In line with our first experiment, both cell types in vCA1 displayed shock-responsiveness during CFC, with astrocytic calcium events uniquely modulated. Optogenetic activation of a DG-mediated fear engram was sufficient to induce calcium dynamics in neurons and astrocytes that were akin to those

displayed during natural recall. Further, these dynamics in both cell types were coupled to fear-related behaviors, such as freezing, during both natural and artificial reactivation of fear. These findings provide the first evidence of neuron-astrocytic coupling as a shared mechanism that enables both natural and artificially-induced memory retrieval, as well as the behavioral expression of fear. The final experiments sought to investigate how astrocytes contribute to contextual fear learning and memory at the single-cell level, enabling a higher-resolution understanding of our previous findings. To accomplish this, we performed freely-moving one-photon calcium recording of dorsal CA1 (dCA1) astrocytes as mice underwent CFC and a subsequent day of contextual recall (Context A; Cxt A) or novel context exposure (Context B; Cxt B). Further, we performed the first longitudinal registration of astrocytes using one-photon imaging to enable analysis of their dynamics across learning. We showed that astrocytes respond to aversive foot shock with sequential calcium activity, akin to that displayed by hippocampal time cells. Notably, these sequences reappear during contextual recall (Cxt A) but not novel exposure (Cxt B), and seem to be driven by reactivated astrocytes across days. Our ongoing work will characterize these sequences across days and explore how they may be coupled with the behavioral expression of fear. These preliminary findings suggest that astrocytes may be involved in temporal coding and provide the first evidence that sequential activity during recall may serve as a memory-specific retrieval process. In summary, my dissertation work presents evidence for the active role of amygdalar and hippocampal astrocytic calcium in the real-time processing of fear learning and memory as it relates to behavior.

## TABLE OF CONTENTS

## LIST OF FIGURES

## LIST OF ABBREVIATIONS

A1Rs…….……Adenosine 1 Receptor

A2ARs…….……Adenosine 2A Receptor

ACC…….Anterior Cingulate Cortex

AIC……..Akaike Information Criterion

AMY…….Amygdala

ANOVA…….....Analysis of Variance

AP……...……..Anteroposterior

Arc…….Activity-Regulated Cytoskeleton-Associated Protein

ArchT……..Archaerhodopsin

ATP……Adenosine Triphosphate

AUC……....Area Under the Curve

BA…….....Basal Amygdala

BLA……Basolateral Amygdala

BM…….Basomedial Amygdala

BNST……Bed Nucleus of the Stria Terminalis

CA1……..Cornu Ammonis 1

CA2……..Cornu Ammonis 2

CA3……..Cornu Ammonis 3

CeA…….....Central Amygdala

CeL……...Central Lateral Amygdala

CeM……Central Medial Amygdala

ChR2……Channelrhodopsin

CFC……Contextual Fear Conditioning

CI…….....Confidence Interval

CNO…….....Clozapine-N-Oxide

CPP…….Conditioned Place Preference

CR……..Conditioned Response

CREB…….cAMP-Response Element Binding Protein

CreER$^{T2}$……Tamoxifen-Inducible Cre recombinase

CS……....Conditioned Stimulus

Cxt A…….....Context A

Cxt B…….....Context B

DAPI…….4',6-diamidino-2-phenylindole

dCA1……...Dorsal CA1

DG……...Dentate Gyrus

dF/F, DF/F……Change in Fluorescence/Baseline

DH, dHPC……Dorsal Hippocampus

DMSO……Dimethyl Sulfoxide

dnSNARE……...Dominant-Negative SNARE Domain

Dox…….....Doxycycline

DREADDs……..Designer Receptors Exclusively Activated by Designer Drugs

DT…….....Diptheria Toxin

DV……..……..Dorsoventral

EC…….Entorhinal Cortex

eCBs…….Endocannabinoids

eYFP……..Enhanced Yellow Fluorescent Protein

fMRI…….Functional Magnetic Resonance Imaging

FOV……Field of View

FP……...Fiber Photometry

F-RAM……..*Fos*-dependent Robust Activity Marking

FWHM…….……...Full Width Half Maximum

GECI…….Genetically-Encoded Calcium Indicators

GFAP……Glial Fibrillary Acidic Protein

GLAST……..Glutamate-Aspartate Transporter

GLT-1…….Glutamate Transporter 1

GPCR……...G-Protein Coupled Receptor

GFP……....Green Fluorescence Protein

GLM……....Generalized Linear Model

GPe……...Globus Pallidus

GRIN……Gradient Reflective Index

HPC…….Hippocampus

hPMCA2w/b……Human Plasma Membrane Calcium Pump PMCA2; CalEx

Hz…….....Frequency

IACUC…….Institutional Animal Care and Use Committee

iBAPTA……Intracellular 1,2-bis(o-aminophenoxy)ethane-N,N,N′,N′-tetraacetic acid)

ißARK……122-Residue Inhibitory Peptide ß-Adrenergic Receptor Kinase 1

IC…….....Insular Cortex

ID……..Identification

IEG……...Immediate Early Genes

IP……....Intraperitoneal

IP3R……Inositol 1,4,5-triphosphate (IP3) Receptor

IHC……Immunohistochemistry

LA…….....Lateral Amygdala

LH……...Lateral Hypothalamus

LTM……...Long-term Memory

LTP……...Long-term Potentiation

MB…….Mammillary Bodies

MeA……..…….....Medial Amygdala

MEC…….....Medial Entorhinal Cortex

ML……...……..Mediolateral

MLRT……Maximum Likelihood Ratio Test

mPFC…….Medial Prefrontal Cortex

MTL……..Medial Temporal Lobe

NAc……...Nucleus Accumbens

NIH……...……National Institutes of Health

NMDAR……..N-methyl-D-aspartate Receptor

N-RAM…… *Npas4*-dependent Robust Activity Marking

NREM…….Non-Rapid Eye Movement

OB…….....Olfactory Bulb

OptoXRs……...Light-Activated GPCR

PAG……...Periaqueductal Gray

PAPs……Perisynaptic Astrocytic Processes

PBS……...…...Phosphate Buffered Saline

PBST……...PBS with 0.2% Triton X-100

PET……..Positron Emission Tomography

PFA……...Paraformaldehyde

PP…….Perforant Pathway

PTSD……Post-Traumatic Stress Disorder

PVT…….....Paraventricular Nucleus of the Thalamus

REM……Rapid Eye Movement

RM …….Repeated Measures

ROIs……Regions of Interest

ROUT……..Robust Regression Followed by Outlier Identification

RSC……...Retrosplenial Cortex

SC……...Schaffer Collaterals

SQ…….....Subcutaneous

TAM…….....Tamoxifen

tCI……....t-Confidence Interval

TRAP…….Targeted Recombination in Activated Populations

TRE…….Tetracycline Response Element

tTA…….Tetracycline Transactivator

US……...Unconditioned Stimulus

vCA1…….....Ventral CA1

VH, vHPC……...Ventral Hippocampus

vlPAG……..Ventral Lateral Periaqueductal Gray

VTA……Ventral Tegmental Area

Zif268……..Zinc Finger-Containing Transcription Factor 268

1p……One-Photon

2p……Two-Photon

# CHAPTER ONE: INTRODUCTION

## *1.1) Astrocytes – Function*

Astrocytes are a star-shaped glial cell type that rivals the number of neurons in the brain (von Bartheld, 2016), yet remain vastly understudied in neuroscience. In the past, the main focus of experiments has been neuronal in nature, largely excluding the role of astrocytes and their fellow glial cells, microglia, and oligodendrocytes. Early studies provided foundational evidence that astrocytes are unique in that they maintain metabolic homeostasis (Alberini et al 2018; Steinman et al 2016), actively support the blood-brain-barrier (Giaume et al, 2010), modulate neurotransmitter release, and release their own gliotransmitters in complex, bidirectional communication with their neuronal neighbors (Araque et al 2014; Bezzi & Volterra, 2001; Covelo & Araque, 2018). Further, they actively contribute to synaptic plasticity (Navarette et al 2012; Papouin et al 2012; Henneberger et al 2020) through uptake and binding of neurotransmitters and release of these gliotransmitters, such as glutamate (Fellin et al 2004; Parpura et al 1994), adenosine triphosphate (ATP)(Zhang et al 2003; Koizumi, Fujishita & Inoue, 2005), endocannabinoids (eCBs) (Navarette & Araque, 2014) and D-serine (Papouin et al 2017) at the tripartite synapse. This is composed of the pre- and postsynaptic neurons, as well as perisynaptic astrocytic processes (PAPs) (Araque et al 1999; Porter & McCarthy, 1997; Haydon, 2001; Perea, Navarette & Araque, 2009; Volterra & Meldolesi, 2005). Here, astrocytes rapidly change their morphology in response to internal and external state changes, and make or break contact with neurons to dynamically control synaptic transmission. Astrocytes exhibit dynamic changes in calcium in response to their external

environment, as well as exhibit calcium-independent responses to release of gliotransmitters **(**Bazargani & Attwell, 2016; Perea & Araque, 2005; di Castro et al, 2011**;** Shigetomi, Patel & Khakh, 2016; Goenaga et al 2023). Like neurons, they respond to their external environment via a wide variety of receptors and transporters, such as NMDARs, AMPARs, glutamate transporter 1 (GLT-1) and glutamate-aspartate transporter (GLAST), all of which are involved in modulation of glutamatergic signaling.

Because astrocytes do not demonstrate 'typical' action potentials as neurons do, these calcium dynamics and gliotransmitter release are common read-outs of their 'activity' and changes during behavior, disease, and injury (Santello, Toni & Volterra, 2019). However, recent work has shown that astrocytes undergo rapid, focal membrane voltage changes at PAPs in response to neuronal activity, unlocking a novel mechanism by which astrocytes and neurons communicate in the brain (Armbruster et al, 2022). Future work will continue to elucidate novel mechanisms that explain how astrocytes and neurons work together to modulate healthy and disease states.

Recently, a boom in imaging and genetic strategies has conferred much finer temporal and spatial resolutions to study astrocytic functioning and their role in cognition and behavior in animal models. In the following sections, I will dive into how these novel tools have built upon the foundational cellular and molecular work described in this section.

*1.2) Astrocytes – Chemogenetics*

Knowledge of astrocytic functioning has grown in recent years due to the implementation of chemogenetic, optogenetic and pharmacological perturbation in various behaviors, disease-states, and brain regions. The use of Designer Receptors Exclusively Activated by Designer Drugs (DREADDs) (Roth, 2016; Armbruster et al 2007) has enabled G-protein coupled receptor (GPCR) activation specifically in astrocytes via selective expression through the glial fibrillary acidic protein (GFAP) promoter**.** Importantly, recent work has shown that chemogenetic activation in astrocytes is not quite as straightforward as manipulation of these receptors in neurons. Specifically, stimulation of Gi/o and Gq-coupled receptors both stimulate release of glutamate from astrocytes that increases neuronal excitability, thus suggesting that inhibition with Gi may be a unique property to neurons and must be considered in perturbation experiments involving astrocytes (Durkee et al, 2019). Further, Gi and Gq activation of astrocytes *in vitro* induces synaptic potentiation, but each pathway utilizes a different mechanism to achieve the same outcome. Gq- and Gi-activation drives these synaptic changes in calcium-dependent and independent mechanisms, respectively (Van Den Herrewegan et al., 2021). These results suggest that astrocytic perturbation with chemogenetic methods may induce similar or different neuronal responses via unique mechanisms. This may provide different outcomes depending on the brain region, GPCR pathway targeted, or behavior monitored due to these nuanced changes in how and when they bidirectionally communicate with neurons.

Chemogenetic experiments have revealed that astrocytes have the ability to modulate local and projection-specific neuronal activity. Gi activation of astrocytes in

dorsal hippocampus (DH) during learning impairs remote, but not recent fear memory recall via projection-specific inhibition of dorsal CA1 (dCA1)-anterior cingulate cortex (ACC) neurons (Kol et al, 2020). More recently, Gi activation of astrocytes were capable of disrupting dCA1-ACC projecting neurons and their engagement during memory schema development in rodents, further supporting their evolving role in projection-specific modulation of neural circuits (Liu et al, 2022). Additionally, Gq activation of astrocytes in the basolateral amygdala (BLA) was shown to modulate BLA-medial prefrontal cortex (mPFC) projecting neurons during fear learning, increasing auditory but not contextual recall of fear (Lei et al, 2022). Further, Gq activation of astrocytes via chemogenetics or endogenous endocannabinoids (eCBs) in the central medial amygdala (CeM) exerted projection-specific effects on neurons within the AMY. Specifically, this activation depressed excitatory synapses from the BLA to the CeM via adenosine 1 receptors (A1Rs) and enhanced excitatory synapses from the lateral CeM via adenosine 2A receptors (A2ARs) to reduce auditory cued fear responses (Martin-Fernandez et al., 2017). Finally, Gq activation of BLA astrocytes after cued fear extinction was shown to maintain low levels of fear during extinction recall a day later (Shelkar et al 2021). Together, these findings suggest that modulation of astrocytes, although less straightforward than neurons, provides ample evidence that they are vital players in learning and memory processes.

Although the above studies have primarily focused on astrocytes' role in learning and memory in canonical brain regions like the amygdala (AMY), hippocampus (HPC) and prefrontal cortex (PFC), their involvement in other realms of behavior are just as informative. Within the striatum, Gi activation of astrocytes increased hyperactivity in the

open field, reduced attentional focus, and induced deficits in novel object detection (Nagai et al, 2019). These findings further validated the idea that astrocytic Gi-coupled signaling pathways, such as $GABA_B$ receptors, can increase astrocytic intracellular calcium levels and fail to 'inhibit' them as occurs in neurons. Astrocytes are also involved in the processing of pain signals, as indicated by their modulation in the ventrolateral periaqueductal gray (vlPAG). Gq activation of these cells induced neuropathic pain and pain-related aversion, while Gi activation alleviated sensations of pain and promoted pain-related preference behaviors (Yang et al, 2022), showing their bidirectional control in chronic pain. Astrocytic modulation has been shown to have an effect on cocaine conditioned place preference (CPP) in dCA1 via Gi-activation (Nam et al, 2019), as well as inhibition of cue-induced reinstatement of cocaine-seeking through Gq activation in the nucleus accumbens (NAc), indicating their possible role in positive emotional valence (Scofield et al, 2015). Additionally, Gq activation of astrocytes in the ACC promotes oligodendrogenesis and remyelination in a rat model of visceral hypersensitivity. Interestingly, this activation rescues decision-making deficits and desynchronization in neurons projecting from ACC-BLA (Hasan et al, 2023). Further, Gi activation of cortical astrocytes alone does not evoke spontaneous glutamate or GABA release, but when coupled with a visual-stimulus it does increase extracellular glutamate (Vaidyanathan et al, 2022). This suggests that astrocytic activity is primarily modulated by salience or behavioral state, with lower levels of 'baseline' activity during home cage or context exposure, an emerging theme in recent literature (Adamsky et al, 2018; Suthard & Senne et al, 2023; 2024). This plethora of astrocytic modulation protocols across attentional, pain

and reward processing provides a unique perspective on how these cells may complete the picture that neurons already exist within diverse brain processes.

*1.3) Astrocytes – Optogenetics*

As described previously, DREADDs have primarily been used in astrocytes to perturb function, as they take advantage of native GPCR signaling mechanisms compared to other techniques like optogenetics, that were developed primarily with neuronal action potentials in mind (Boyden et al, 2005). Specifically, the light-gated ion channel, channelrhodopsin-2 (ChR2) (Nagel et al, 2003) functions to excite neurons via rapid membrane depolarization that is not as physiologically relevant to increases in astrocytic intracellular calcium. However, optogenetic tools have been developed to enable selective activation of GPCR signaling pathways in astrocytes with spatial and temporal precision, such as melanopsin (Mederos et al 2019) and OptoXRs (Airan et al 2009), such as Optoα1AR (Adamsky 2018) that are coupled to astrocytic Gq pathways. A comparative study observed that both ChR2-variants and OptoARs (Gq- and Gs-coupled) in astrocytes induced reliable intracellular calcium elevations in an ATP and P2YR-dependent manner (Figuierdo et al 2014), suggesting that these adapted methods are useful for understanding astrocytic functioning.

A recent study used both Optoα1AR and Gq-DREADDs to activate astrocytes during memory acquisition in dCA1 and observed enhanced contextual, but not cued memory recall (Adamsky et al, 2018). This study shows that a similar elevation of neuronal activity in this region induced an impairment in memory recall, providing evidence that astrocytes are likely responding to neurons in a tailored, task-dependent manner. This idea

of astrocytes responding in a task or stimulus-dependent manner has been supported by other work that showed Gi activation of cortical astrocytes alone does not elicit glutamate or GABA release, it must be paired with a meaningful visual stimulus (Vaidyanathan et al 2022). Interestingly, optogenetic activation of astrocytes with ChR2 in dCA1 within a defined time window after a traumatic experience disrupts memory consolidation and reduces subsequent contextual memory recall in an ATP/adenosine-dependent manner (Li et al, 2020). This provides evidence that the timing (e.g. acquisition, recall, consolidation) of astrocytic manipulation in the same brain region may produce different, task-dependent changes in behavior. This sheds light on the dynamic nature and precise timing of astrocytic involvement in higher cognitive processes like memory formation and retrieval.

In addition to regulating memory, astrocytes have been shown to be crucial for a suite of behaviors and brain states, such as anxiety, depression, sleep, and wakefulness, using optogenetic techniques. Recent work elevating astrocytic intracellular calcium levels using ChR2 in DH induced anxiolytic effects in the elevated plus maze and open field (Cho et al, 2022). Complementary studies have elucidated the role of astrocytes in sleep and wake states in multiple regions of the brain (Pelluru et al, 2016; Yamashita et al, 2014; Peng et al, 2023). Pelluru et. al. argues that ChR2 activation of astrocytes in the posterior hypothalamus at varying stimulation frequencies increases both non-REM (NREM) and REM sleep during the dark period where mice are typically active (Pelluru et al, 2016). Yamashita et. al. defines astrocytic involvement in sleep disturbances through ChR2 activation in the ACC, which reduces NREM sleep and promotes wakefulness (Yamashita 2014).

*1.4) Astrocytes – Alternatives to DREADDs or Optogenetics to Modulate Activity*

Many of the tools developed to modulate electrical and cellular activity in the brain have been targeted towards neurons. As astrocytes have been shown to primarily communicate primarily with changes in calcium dynamics and gliotransmitter release, efforts have been made to repurpose and develop new techniques to modulate these unique cells in order to uncover their role in brain functioning. As discussed above, chemogenetics can have varying effects on astrocytic calcium signaling, gliotransmitter release and behavioral outcome. This is especially noted in Gi-coupled modulation, where this would normally inhibit neuronal action potentials, but has been shown to increase astrocytic calcium levels (Nagai et al 2019; Durkee et al 2019). Other studies have added to the complexity of astrocytic modulation, showing that Gi activation initially increases astrocytic calcium and then transiently decreases levels over time (Kol et al, 2020). Earlier efforts showed that astrocyte calcium signaling is dependent on inositol 1,4,5-triphosphate (IP3) receptor (IP3R) signaling in vivo and in vitro (Petravicz, Fiacco & McCarthy, 2008; Di Castro et al 2011; Takata et al 2011). Mouse models of genetic knockout of astrocytic IP3R to modulate calcium signaling have yielded complex behavioral results (Petravicz, Boyt & McCarthy, 2014; Pinto-Duarte et al 2019; Tanaka et al 2013), suggesting the idea that astrocyte calcium signaling and gliotransmitter release can also be IP3R-independent (Srinivasan et al 2015; Agulhon et al 2010). Further, selectively blocking gliotransmitter release from astrocytes using a transgenic mouse line expressing dominant-negative SNARE domain (dnSNARE) showed that the release of ATP and adenosine is vital for synaptic transmission and plasticity (Pascual et al 2005). Further, using dnSNARE to

impair gliotransmission desynchronizes dCA1-PFC theta oscillations, but supplemental D-serine rescues this phenotype and accompanying cognitive deficits (Sardinha et al, 2017). These methods provide alternatives to non-selective modulation of astrocytes using chemo- or optogenetics with very specific changes to aspects of functioning (intracellular calcium stores; gliotransmission, etc.)

More modern efforts to modulate astrocytic functioning have targeted astrocytic calcium using application of intracellular BAPTA (iBAPTA), a calcium chelator, in addition to the IP3R2 knockout (IP3R2-/-) mouse model discussed previously. For example, IP3R2-/- mice *in vivo* and iBAPTA application *ex vivo* change astrocytic calcium in a similar manner to a corticosterone model of major depressive disorder, providing insight into the dysfunction present in brain disorder (Gonzalez-Arias et al 2023). Further, the human plasma membrane calcium pump PMCA2 (hPMCA2w/b; "CalEx") was modified to selectively extrude calcium from astrocytes using viral expression and was shown to increase excessive grooming behaviors in mice (Yu, Nagai et al 2020). Further, reduction of cortical astrocytic calcium using CalEx during development resulted in impairments in social interaction, increases in depression-like behaviors and aberrant synaptic structure and transmission (Luo et al 2023). Most recently, the same researchers developed 122-residue inhibitory peptide ß-adrenergic receptor kinase 1 (ißARK) to selectively attenuate Gq-, but not Gs- or Gi-coupled, calcium signaling in astrocytes and demonstrated meaningful changes in behavior when used in the striatum and visual cortex (Nagai et al 2021). This tool allowed researchers to not only modulate astrocytic calcium,

but do so in a cell-type and GPCR pathway-specific manner, allowing for greater interpretability of results.

*1.5) Astrocytes – Cellular and Molecular Modulation*

These systems-level modulations of astrocytes *in vivo* have provided meaningful evidence that these cells are actively involved in complex brain function. Building upon these findings, many studies have performed more targeted molecular and cellular manipulations in vivo to understand how these changes are occurring. For example, conditional knockout of Rac1, a cytoskeletal remodeling protein, in astrocytes before fear learning was able to improve fear memory acquisition, as well as contextual and cued recall (Liao et al 2017). This finding was further supported by findings that fear acquisition alone can downregulate Rac1 protein levels and facilitate the formation of a conditioned fear memory in mice (Fan et al 2021). Further, connexin-43, an astrocytic gap junction protein, was shown to be necessary for fear memory consolidation in the BLA. Inhibition of this protein during memory consolidation decreased auditory cued fear memory during recall (Stehberg et al 2012). These findings, amongst many others, show that astrocytic functioning at the cellular level is vital to the acquisition, consolidation, and retrieval of memory-related information in the rodent brain.

*1.6) Astrocytes – Imaging*

DREADDs and optogenetics only allow for perturbation without any real-time understanding of their natural state during behavior. Like neurons, astrocytes display complex intracellular calcium dynamics that can be spontaneous or triggered by responses

to external stimuli, such as neurotransmitter binding of astrocytic receptors. Importantly, some astrocytic release of gliotransmitters occurs in a calcium-independent manner, making even these methods incomplete analysis of their unique functioning. Genetically-encoded calcium indicators (GECIs), such as GCaMP, RCaMP, and jRGECO allow for recording of these calcium dynamics in real-time with unique kinetics, signal-to-noise ratios, and fluorescence excitation spectra. These GECIs can be specifically expressed in astrocytes through the use of astrocyte-specific promoters, like GFAP, in the form of viral vectors expressed in the brain region of interest or transgenic mouse lines with ubiquitous expression. Researchers have used these tool developments to image and record from astrocytes in mice, rats, zebrafish and more, using fiber photometry (FP), one-photon (1p) and two-photon (2p) imaging methods. Bridging this gap, studies have begun using a combination of modulatory techniques like opto- and chemogenetics and imaging to understand the real-time effects of astrocytic calcium disruption. Building upon work showing that astrocytes are essential for sleep-wake regulation in the basal forebrain and brainstem (Pelluru et al 2016; Yamashita et al 2014), optogenetic-evoked elevations in astrocytic calcium were not able to increase extracellular adenosine, as measured by an ATP sensor and FP (Peng et al 2023). The use of imaging techniques like FP, 1p and 2p imaging will be described in the subsequent sections, as well as how these tools unlock our ability to monitor real-time astrocytic involvement in cognition and behavior.

### *1.6.1) Fiber Photometry*

To begin, FP is an optical recording technique that measures the population-level fluorescence changes of GECIs in a cell type of choice during freely moving behavior. FP was originally developed to answer questions about how specific projections in the brain are actively involved in animal behavior (Gunaydin et al, 2014; Cui et al, 2014). For example, original use of this method showed that ventral tegmental area (VTA) to NAc-projecting neurons can modulate social interaction in combination with optogenetics in freely-moving mice (Gunaydin et al, 2014). This technique has a low barrier of entry, as the implants are relatively simple to localize to the brain region of interest and are less invasive than other imaging methods. Due to the nature of the implant, calcium recordings from deep and superficial brain regions can be obtained with ease. These implants are lower in weight, less stressful and thus, easier to record freely-moving behavior from an animal during complex tasks. FP is compatible with other techniques, such as optogenetics and chemogenetics, allowing for perturbation of circuits during recordings.

Only in recent years has FP been used to record bulk calcium dynamics from astrocytes rather than neurons. Similar to its use in Gunaydin et al, a novel study showed that fiber photometry recordings of astrocytic calcium dynamics in the NAc are directly modulated by synaptic dopamine release from the VTA and this is amplified by administration of amphetamine (Corkrum et al., 2020). Astrocytic calcium has also been recorded within the DH and cortex, with previous work showing delayed-onset peak events in response to locomotion onset and foot shock ranging from 5-10 seconds (Qin et al, 2020). Recent work has also utilized astrocytic population-level calcium recordings to

understand their involvement in the sleep-wake cycle across the cortex, HPC, hypothalamus, cerebellum, and pons (Tsunematsu et al, 2020). These experiments have demonstrated significant decreases in astrocytic calcium during REM sleep and increases with the onset of wakefulness across all brain regions, but dynamics in NREM sleep were dependent on brain region. These findings altogether show that astrocytes are involved in a diversity of behaviorally-relevant states (e.g. sleep, wake, locomotion, stimulus-response) and this activity differs across brain regions.

FP can also be used to record multiple cell types (e.g. neurons and astrocytes) simultaneously using non-overlapping GECIs (e.g. jRGECO and GCaMP) within the same brain region to understand their functioning within neural circuits. For example, dual-color recordings in dCA1 using FP have shown a strong, correlated, and antagonistic relationship between neurons and astrocytes during the encoding and retrieval phases of a working memory task (Lin et al, 2022). Specifically, this antagonistic relationship shows a rise in astrocytic calcium that is coupled with a decrease in neuronal calcium, which they speculate may involve the release of ATP/adenosine and GABA to inhibit nearby neuronal activity with a 3-second delay. As these imaging methods have advanced in astrocytes, the field has been able to combine FP with modulation tools described previously. For example, recent work used FP to measure astrocytic calcium in the globus pallidus (GPe) and its temporal dynamics across habit- and goal-directed learning. Here, they showed that there is an inverse relationship between neurons and astrocytes in the region, with chemogenetic Gq activation of astrocytes or Gi inhibition of neurons in GPe facilitating the transition from habitual to goal-directed reward seeking behaviors (Kang et al, 2023).

This combination of calcium imaging and chemogenetic tools enabled a more nuanced understanding of how astrocytes and neurons in reward circuits are changing across learning and working with one another to enable habit formation in healthy and maladaptive (addiction, obsessive-compulsive disorder) brains.

### *1.6.2) One- and Two-Photon Imaging*

FP has provided foundational insight into astrocytic calcium dynamics in freely-moving animals. As with any technique, FP has its limitations, specifically its low cellular and spatial resolution. This tool only allows for recording of aggregated activity within a specific brain region, thus providing only 'bulk' population-level changes in fluorescent signal. However, 1p and 2p imaging of astrocytes has enabled unprecedented analysis of their calcium dynamics on the single-cell level, in both head-fixed and freely-moving animals.

Microendoscopes ("miniscopes") are light-weight, head-mounted, miniature microscopes that enable monitoring of GECI fluctuations within individual cells during freely-moving behavior in rodents. These miniscopes enable both deep and superficial 1p imaging when coupled with either gradient-refractive-index (GRIN) lenses or cortical windows. Like FP, this imaging technique allows for recording of genetically-defined cell populations (e.g. astrocytes, CaMKII+ neurons, PV+ interneurons), with the advantage of high spatial resolution (e.g. single cells vs. population-level). However, this technique has low sensitivity and high noise, as 1p imaging produces lower spatial resolution compared to multi-photon methods like 2p microscopy that may be necessary to answer specific research questions. 2p imaging alternatively offers higher cellular resolution, allowing for

investigation of calcium dynamics even at the subcellular level (e.g. dendrites, axonal boutons, astrocytic processes). This method requires the assistance of an optical cannula or GRIN lens to image deeper into the brain, like 1p, but alone can penetrate much deeper with only a cortical window. Typically, 2p imaging requires that the animal remains head-fixed during behavior, but recent developments have melded the benefits of miniscopes and 2p imaging into the Mini-2p (Zong et al, 2022). This tool is open-source and will likely lead to the rapid adoption across many labs, as it provides higher-resolution imaging during naturalistic behaviors that are necessary for many experimental questions.

In astrocytes, most work investigating their *in vivo* calcium dynamics has utilized two-photon recordings, capturing their unique morphology at higher spatial resolution, and enabling subcellular analysis of their somas vs. processes. Fundamental questions about the properties of astrocytic calcium signaling have been rigorously investigated using 2p imaging. Astrocytic calcium dynamics in different subcellular compartments (processes, somas, end feet) have been shown to display distinct spontaneous and stimulus-evoked signaling characteristics (Stobart et al, 2018). Early work showed that cultured cerebellar astrocytes required synchronous calcium release from three or more subcellular sites in order to trigger a global calcium response (Croft et al, 2015). Further *in vitro* and *in vivo* imaging of astrocytes in response to sensory stimuli or locomotion have shown that their calcium signals originate in the distal processes and propagate towards the soma once a spatial threshold (>23%) is surpassed (Lines et al, 2023; Fedotova et al, 2023), suggesting how these cells may integrate local synaptic activity into a summed neuromodulatory response. Interestingly, this previous work (Fedotova et al, 2023) also showed that neuronal

calcium peaks at the onset of locomotion, while astrocytes lagged behind by 2.5 seconds, further suggesting that astrocytic calcium may be slower as they're integrating sensory information via filtering, processing, and comparison to past experiences.

With this growing knowledge about astrocytic calcium functionality, understanding their complex role in animal behavior using high-resolution imaging has become an important next step. *In vivo* imaging of cortical astrocytes has demonstrated that their calcium signals precede switches into a slow-oscillation state characterized by synchronized neuronal firing (i.e. local field potential recordings) that is important for sleep and memory (Poskanzer & Yuste, 2016). Further, 2p recordings of dCA1 astrocytes have shown that they ramp their calcium activity towards reward in familiar, but not novel environments (Doron et al 2022). Further, they find no evidence of 'place astrocytes' in dCA1 that tile the entire virtual environment, only that ~30% of cells contained significant spatial information. Other dCA1 2p imaging work has demonstrated that both astrocytes and neurons contain spatial information, working together in a complementary and synergistic manner (Curreli et al, 2022). Interestingly, they claim that single astrocytes can encode spatial information from more than one 'place field'. Reconciling these findings, it may be possible that astrocytes are representing the environment in a way that is unique from neurons, but still contain important spatial information within the circuit. To fully understand the role of astrocytes in spatial representations, it will be important to perform imaging in freely-moving rather than head-fixed animals, in line with foundational work on neuronal place cells.

Very few experiments have utilized this freely-moving 1p imaging of astrocytes to dissect their functioning during behavior. Work from Ingiosi et al 2020 demonstrated that cortical astrocytic calcium displays dynamic changes at the boundary between REM sleep and wakefulness using head-mounted miniscopes. However, these findings assessed gross calcium activity within the cortical field-of-view (FOV) rather than single astrocytic regions-of-interest (ROIs). In order to quantify subcellular somatic and process calcium, they instead utilized 2p microscopy, in line with previous work (Ingiosi et al, 2020). Further, GRIN lens imaging has been used in the striatum to monitor calcium signals from GCaMP+ medium spiny neurons and CalEx-expressing astrocytes, but this analysis focused on neuronal dynamics during behavior when astrocytes were depleted of calcium (Yu et al, 2018). These experiments shed light on a major gap in the field, where the role of astrocytes in freely-behaving mice is yet to be explored at the single-cell level.

As my research in this dissertation focuses on the role of astrocytes and neurons in learning and memory processes, I will pivot to exploring the foundational roles of the HPC and AMY.

### *1.7) Hippocampus*

The hippocampus is a region within the medial temporal lobe (MTL) that is responsible for processing context and temporal information, two domains that provide the basis for episodic memory (Squire et al 2009; Scoville & Milner, 1957; Eichenbaum, 2004). Early work in Patient H.M. showed that lesioning regions within the MTL, such as the HPC and portions of the AMY, resulted in retrograde amnesia or the inability to form new episodic memories (Scoville & Milner, 1957). This idea of episodic memory was first

described by Endel Tulving as “receiv[ing] and stor[ing] information about temporally-dated episodes or events, and temporal-spatial relations among these events,” representing “a more or less faithful record of a person’s experiences” (Tulving, 1972). We now understand episodic memory as a vivid, detailed representation of an experience as described by a specific time and place, as well as the accompanying external sensory and internal context. Tulving proposes a particularly poignant idea that remembering is just a form of “mental time travel,” where we are able to replay events as if reliving them in real-time (Tulving, 1983; Eichenbaum & Cohen, 2001).

### *1.7.1) Subregions*

The HPC is composed of four main subregions: the dentate gyrus (DG), CA1, CA2 and CA3. The DG receives inputs conveying cortical sensory information via the perforant pathway (PP) from the entorhinal cortex (EC). It is thought that the DG performs a function called *pattern separation*, working to reduce the overlap between similar input patterns that are communicated to downstream CA3 (McNaughton & Morris, 1987; Leutgeb et al 2007). The *molecular layer* of the DG is almost entirely lacking cell bodies, and contains primarily the dendrites of granule cells, where the PP fibers enter the hippocampus from the EC. The *granule cell layer* contains densely-packed granule cell bodies in the DG that perform the complex computations of this region. Finally, the *polymorphic layer* of the DG is primarily mossy cells that project and communicate information to the CA3 region of the hippocampus.

Once CA3 receives this disentangled information from the DG, it performs *pattern completion* to associate linked components of an episodic memory and trigger successful

retrieval. A retrieval cue, such as an odor, texture, or visual stimulus, can activate a subset of CA3 cells and cascade into activation of an entire episodic experience, akin to smelling a candle that reminds you of baking cookies with family in your childhood home (Marr, 1971). CA3 sends projections via the Schaffer collaterals (SC) to CA1, the main output region of the hippocampus that compares this current experience with those you've previously encountered. Specifically, CA1 compares the current reconstructed version of an experience from CA3 to the existing sensory information provided by EC (Levy, 1989; Eichenbaum & Buckingham, 1990). In summary, sensory information from primary and association cortices are funneled into the EC (Amaral & Witter, 1989; Lipton & Eichenbaum, 2008), where similar information is separated by the DG into unique representations. Here, this information is sent to CA3 for reactivation of the experience and CA1 compares this representation to the existing sensory environment that EC is conveying to the HPC.

For many years, astrocytes were viewed largely as a homogenous group of cells, unlike neurons that display genetically, structurally and functionally-defined subtypes across brain regions. However, recent work has shown that within hippocampal subregions, astrocytes display heterogeneity in the complexity of their morphology that is maintained across the dorsoventral axis (Viana et al, 2023). Further, single-cell RNA sequencing analysis of astrocytes within the cortex and hippocampus revealed transcriptionally-distinct subtypes that display similarly unique morphological and physiological properties (Batiuk et al, 2020). Ongoing work in the field aims to uncover more about astrocytic

diversity within and across brain regions, and how it relates to functional differences during cognition and behavior.

In Chapters Three and Four, I will explore how astrocytes are engaged in memory processing within the DH and ventral (VH) hippocampus, and will describe how these regions are unique in the subsequent section.

### *1.7.2) How are the dorsal and ventral hippocampus structurally, functionally, and genetically diverse?*

The hippocampus is a single structure that has been traditionally understood as two distinct functional divisions: DH and VH (Moser & Moser, 1998; Fanselow & Dong, 2010), with unique inputs and outputs (Swanson & Cowan, 1977; Amaral & Witter, 1989). Structurally, DH and VH share many inputs, but differ in how they receive this information via distinct local organization of incoming projections (Tao et al 2021). However, DH receives stronger intrahippocampal inputs from CA2 and CA3, while VH receives information from CA3 and EC. Further, DH receives projections from sensory cortices via the EC, while VH receives more direct olfactory and amygdalar nuclei inputs that DH does not (Burwell and Amaral, 1998; Witter et al 1989**;** Tao et al 2021). Both subdivisions project to the hypothalamus via the septum, but interestingly, DH and VH project to the dorsal and ventral lateral septum, respectively, showing some level of topographical mapping (Risold & Swanson, 1996). VH projects monosynaptically to regions like the prefrontal cortex (PFC), AMY, NAc, and hypothalamus, and these projection-specific neurons differ in their gene expression profiles (Pitkanan et al 2000; Gergues et al 2020; Strange et al 2014). Further, DH projects to the mammillary bodies (MB), retrosplenial

cortex (RSC), anterior cingulate cortex (ACC), NAc and the anterior thalamic nuclei (Trouche et al 2019; Opalka et al 2020). Over time, the anatomical connectivity patterns of the DH and VH have evolved drastically, uncovering new and unique ways that these brain regions communicate with the rest of the brain.

Early functional studies in rodents demonstrated that the DH, but not VH, is necessary for spatial memory and navigation (Moser et al 1993; 1995; Bannerman et al 1999; Pothuizen, 2004). On the other hand, lesions of the VH alter stress response and emotional behaviors (Henke, 1990), whereas DH lesions do not. Further, VH manipulations have been shown to impact fear, anxiety, motivation, and reward responses (Kjelstrup, 2002; Maren & Holt, 2004; Ferbinteanu and McDonald, 2001; Bannerman et al 2002; McHugh et al 2004). Place cells, first discovered in region CA1, even show functional differences across the HPC long-axis (O'Keefe & Dostrovsky, 1971; O'Keefe & Speakman, 1987; McNaughton, 2006). VH has a lower density of place fields and increased place field size, resulting in a coarser representation of space that is paralleled by a reduction in theta rhythm, vital for spatial learning (Jung, Wiener, & McNaughton, 2004; Royer et al 2010). In humans, these DH and VH differences are mirrored across the anterior-posterior axis of the brain. In the famous London taxi driver experiment, the posterior HPC (analogous to dorsal) was significantly larger compared to control participants as measured by functional magnetic resonance imaging (fMRI), suggesting that this region is vital for spatial representations and navigation behaviors (Maguire et al 2000).

Early work showed molecular evidence for a dorsal-ventral pattern of gene expression within the HPC that supported the structural and functional dissociation previously observed in rodents and humans (Lein et al 2007; Fanselow & Dong 2010). The HPC could be divided along this longitudinal axis into the dorsal, intermediate, and ventral domains based on shared gene expression profiles (Dong et al 2009). Interestingly, VH gene expression was more correlated with extra-hippocampal regions like the AMY, lateral septal nucleus, bed nucleus of the stria terminalis (BNST) and hypothalamus, suggesting shared genetic characteristics between the input/output regions of HPC subregions. However, there were early signs that the HPC may not vary across the axis quite as neatly as anticipated, with greater genetic and functional heterogeneity (Leonardo et al 2006). In light of this, there has been movement away from these strict functional, structural, or genetic subdivisions of the HPC over the past two decades. Instead, researchers have found evidence of both gradients and discrete transitions in HPC connectivity and gene expression in rodents, primates, and humans alike (Cembrowski et al 2016; Vogel et al 2020; Strange et al 2014).

### *1.8) Amygdala*

The AMY is an essential limbic structure in the brain that has been evolutionarily conserved across species for emotional processing (Jarvis, 2005; Johnston, 1923; Kappers, 1936). This region is composed of multiple subnuclei that are heavily interconnected and receive inputs from cortical and subcortical regions (Sun et al 2020). The BLA is composed of the lateral amygdala (LA), basal amygdala (BA) and the basomedial amygdala (BM) and is the primary region (Maren & Quirk, 2004). Next, the medial amygdala (MeA)

houses both glutamatergic excitatory and GABAergic inhibitory interneurons (Maren & Quirk, 2004). The central amygdala (CeA) is composed of the central lateral amygdala (CeL) and central medial amygdala (CeM) and contains GABAergic interneurons that locally project from CeL to CeM. The CeA is the main output region of the AMY and projects to autonomic (blood pressure, heart rate), behavioral (freezing, aggression, avoidance) and endocrine centers (midbrain, pons, BNST, hypothalamus)(Ressler et al 2011; Davis, 1992; LeDoux, 1992). From the external environment, multimodal sensory information is sent from the sensory cortices and thalamus to these deep nuclei. From here, the AMY bidirectionally communicates with the PFC, HPC, striatum, brainstem, and other widely distributed areas to signal behavioral outputs (Roozendaal, McEwen and Chattarji, 2009).

Specifically, the amygdala has been shown to be actively involved in fear, reward, social and anxiety-related behavioral processing (Tye & Janak, 2015). Interestingly, the amygdala contains genetically-defined subpopulations across the anterior-posterior axis of the BLA (Kim et al, 2016; 2017). Rspo2+ (anterior) and Ppp1r1b+ (posterior) neurons in the BLA bidirectionally drive behaviors when optogenetically stimulated. Specifically, Rspo2+ neurons drive defensive responses, while Ppp1r1b+ neurons drive appetitive responses (Kim et al, 2016). Both of these defined cell types project to the NAc and CeA. Further, optogenetic stimulation of projections from BLA→ CeA increased anxiety, BLA→ CeL decreased anxiety-related behaviors and BLA→ VH stimulation decreased social interaction propensity, showing how unique projections from amygdalar nuclei can

have complex and differing effects on emotion-related and motivated behaviors (Feliz-Ortiz et al 2014; Tye et al 2011).

*1.9) Conditioned Fear*

Conditioned fear is widely used to study how the brain acquires, maintains, and retrieves memories, a phenomenon that is observed in rodents, primates, and humans alike (Janak & Tye, 2015). Fear conditioning couples a conditioned stimulus (CS), like a tone or context, with an unconditioned stimulus (US), like a foot shock, that is inherently aversive. When paired multiple times, the CS and US become associated and the CS alone becomes sufficient to drive a conditioned response (CR), such as freezing, darting or escape behavior (Maren, 2001). During extinction, subsequent presentations of the CS without the US will decrease fear as it no longer predicts an aversive outcome. Extinction is understood as not eliminating the CS-US association, but instead producing a new inhibitory CS-no-US association and simultaneously weakening the original to prevent its reactivation. This paradigm allows us to study how memory systems behave under normal conditions and understand how changes in circuit functioning can lead to debilitating disorders of maladaptive fear like Post-Traumatic Stress Disorder (PTSD).

*1.10) Conditioned Fear - Amygdala*

The AMY is critical for encoding, storing, and retrieving the associations between contexts or cues and emotional stimuli (Maren & Quirk, 2004; LeDoux, 2000; Davis & Whalen, 2001). This is evident as lesions of the AMY impair acquisition of fear when a tone or context (CS) is paired with an aversive foot shock (US) (Philips & LeDoux, 1992).

Conditioned fear relies on the convergence of CS-US information onto single neurons within the LA, resulting in local N-methyl-D-aspartate receptor (NMDAR)-dependent synaptic plasticity (Romansky et al 1993; Malenka & Nicoll, 1993; Goosens & Maren, 2004; Fanselow & Dong, 1999). Modulation of long-term potentiation (LTP) within these inputs to the BLA can induce or prevent memory acquisition (Nabavi et al 2014). Auditory CS inputs to the LA primarily originate from the thalamus and cortex (LeDoux et al 1990; Romanski et al., 1993), while contextual CS inputs are first routed through the HPC and then converge onto the LA (LeDoux, 2000). From here, this tone-context CS information is conveyed to the CeA, a region that is well-positioned to mediate conditioned fear responses via auditory and contextual cues (Pitkanen, Savander & LeDoux, 1997). The CeA projects to regions such as the hypothalamus, midbrain, and lateral hypothalamus to control the expression of fear responses (LeDoux, 1988; Kapp 1992). Interestingly, selective lesioning of CeA→ lateral hypothalamus (LH) projections disrupts blood pressure changes, while CeA→ periaqueductal gray (PAG) projections disrupts freezing behaviors, shedding light on the nuanced projection-specificity involved in mediating complex expression of fear (LeDoux, 1988). Importantly, the AMY can also modulate incoming sensory information from the cortex, playing a vital regulatory role (Turner, Mishkin & Knapp, 1980). Disruption of neurons in the BLA or CeA has detrimental effects on the encoding and expression of conditioned fear (Maren et al., 1996; Campeau & Davis, 1995).

Plasticity in the AMY is also important for the retrieval and extinction of conditioned fear (Quirk & Mueller, 2008; Herry et al 2010). Neurons in the AMY increase

their firing in response to presentation of the CS (tone or context) during retrieval and this response decreases in magnitude after extinction (Repa et al 2001; Maren, Poremba & Gabriel, 1991; Maren 2000; Quirk, Repa & LeDoux, 1995). However, some neurons in the AMY increase their firing in response to the CS in the extinguished context (Herry et al 2008; Goosens, Hobin, & Maren, 2003), suggesting that there are multiple populations of cells that dynamically encode a new extinction memory (CS-no-US) and decrease the strength of the original (CS-US).

*1.11) Human amygdala and fear*

A classic study in nonhuman primates demonstrated that broad amygdalar lesions from temporal lobe resection resulted in reduced aggression, fear, and defensive behaviors, that were typically observed in these animals when intact **(**Kluver & Bucy, 1937). Further, lesioning of the AMY impaired an animal's ability to learn positive and negative reinforcing stimuli (Weiskrantz, 1956). In humans, positron emission tomography (PET) and fMRI has shown increased amygdalar activity in response to fearful faces, images, and cues (LaBar, 1998; Morris, Ohman, & Dolan, 1998). In patients with PTSD, where there is a more severe stress response, there is increased amygdalar activation in response to fearful stimuli compared to controls (Liberzon & Sripada, 2007). Human amygdalar damage results in impaired processing of emotionally-salient stimuli, such as recognition of facial emotion and tone of speech (Adolphs, 1995; Calder et al., 1996). Patient S.M., an individual with genetic bilateral degeneration of the AMY, showed severe deficits in conditioned fear response via skin conductance measures despite being able to describe the fearful events (Bechara et al 1995).

*1.12) Conditioned Fear - Hippocampus*

Contextual fear conditioning (CFC) requires both the HPC and AMY (Blanchard & Blanchard, 1972; Maren, Aharonov, & Fanselow, 1997; Kim & Fanselow, 1992). As mentioned previously, the HPC is responsible for routing information related to the CS (context) to the AMY where it converges with other CS's (tone) and the US (shock) to generate an associative memory. This information is routed to the AMY directly via connections between the VH and the BLA or indirectly through the medial entorhinal cortex (MEC) (Kim & Cho, 2020). Inhibition of these HPC pathways providing contextual information to the AMY during conditioning prevents learning (Kim & Cho, 2020; Maren & Fanselow, 1995). Interestingly, lesioning the HPC before acquisition impairs an animal's ability to form and store the contextual information about the environment, requiring more shock trials or pre-exposure to the context to overcome this deficit (Wiltgen et al 2006; Young, Bohenek & Fanselow, 1994). This ties in nicely with the idea that the AMY is forming the CS-US association and the HPC is providing information about the context.

Memory consolidation occurs after acquisition, with reorganization of the memory from its initial encoding sites to a widely-distributed network of brain regions (Takehara-Nishiuchi, 2021). Canonically, during consolidation of a contextual memory, there is a shift from the HPC to the PFC and other regions like the paraventricular nucleus of the thalamus (PVT), insular cortex (IC) and PAG from recent to remote memory (Denny et al 2014; Kitamura et al 2017; Penzo et al 2015; Johansen et al., 2010). This is supported by findings that post-training lesions of the HPC have a greater effect when performed immediately

after conditioning compared to later time points (Kim & Fanselow, 1992; Maren, Aharonov and Fanselow, 1997; Anagnostaras, Maren and Fanselow, 1999). This phenomenon is observed in human HPC lesions as well (Bayley, Gold, Hopkins, & Squire, 2005).

Activity within the AMY-HPC circuit is vital for fear extinction memory formation, as evidenced by inhibition of BLA→ VH projections (Nguyen et al, 2023). This suggests that the AMY instructs the formation of contextual and tone safety representations in the VH to enable extinction memory generation. Even after a memory is extinguished, this AMY-HPC communication is vital for fear renewal and involves regions like the PFC as well. Lesions of the HPC disrupt this reinstatement of fear after extinction (Wilson, Brooks, & Bouton, 1995). Further, VH projections to the BLA and mPFC are essential for fear renewal after extinction, with the HPC and mPFC modulating amygdalar output on the expression of fear in response to an extinguished CS (Corcoran & Quirk, 2007; Orsini et al 2011).

### *1.13) Neuronal ensembles or 'engrams'*

#### ***1.13.1) What is an engram?***

In the early 20th century, Richard Semon proposed that memories are encoded as physical changes in the brain resulting from a specific experience (Semon, 1921; 1923). Lesioning of various cortical regions impaired spatial memory only after a large area was removed, providing the first evidence that memories may not be stored in discrete locations and are instead widely-distributed throughout the brain, which came to be known as the Mass Action Principle (Lashley & Franz, 1917; Lashley, 1950; Josselyn, 2010). Further

work in humans showed that damage within cortical regions produced very little effect on memory, mirroring early findings by Lashley and colleagues, and providing evidence for Hebb's 'cell assembly' theory where there is a widely distributed neural substrate of memory (Hebb & Penfield, 1940; Hebb, 1949). Experimental evidence of synaptic plasticity via LTP sparked the idea that synaptic strengthening within these cell assemblies during an experience may provide the basis for long-term memory (LTM) and recapitulation of this activity provides basis for retrieval (Josselyn, Kohler & Frankland, 2017; Bliss & Lomo, 1973; Collingridge, Kehl & McLennan, 1983). Digging deeper into the mechanisms behind neuronal ensemble formation, DG engram cells that were tagged during CFC had greater intrinsic cellular capacitance and dendritic spine density than non-engram cells, providing evidence for increased structural plasticity between memory-bearing cells (Ryan et al 2015).

### *1.13.2) How do we study engrams?*

To understand the nature of memory engrams, research over the past two decades has used the Tet-tag and Targeted Recombination in Activated Populations (TRAP) systems to label and manipulate neurons activated during an experience. Both systems rely on the expression of immediate early genes (IEGs) like *cfos*, *arc* and *zif* that encode for the proteins c-Fos, activity-related cytoskeletal protein (Arc) and zinc finger-containing transcription factor 268 (Zif268) which are all upregulated when neurons are sufficiently activated and express on different timescales (Guzowski et al 1999; 2001; Flavell & Greenberg, 2008; Greenberg & Ziff, 1984). Specifically, the Tet-tag system relied on the *cfos* promoter to drive transcription of an actuator like ChR2 or green fluorescent protein

(eYFP) in active neurons. This process occurs when activation of the *cfos* promoter drives expression of the tetracycline transactivator (tTA) which binds to the downstream tetracycline response element (TRE) and drives expression and labeling of the actuator in cells. The binding of tTA-TRE is blocked by the presence of doxycycline (Dox) in the animal's diet, allowing for temporally-specific 'tagging' of active neurons when removed (Reijmers et al, 2007; Liu et al, 2012). The TRAP system relies on a tamoxifen (TAM)-inducible Cre recombinase ($CreER^{T2}$) that is expressed under control of an IEG promoter with a *loxP-flanked* STOP signal. In the presence of TAM, Cre recombinase translocates to the nucleus, cleaves the *loxP* sites and removes the STOP signal, allowing for expression of the transgene in active cells within a more precise temporal scale than the Tet-tag system allows (Guenther et al, 2013; Denny et al, 2014; DeNardo et al, 2019). Both of these systems have enabled labeling of active engram cells during the encoding of a salient experience (i.e. fear conditioning) and analysis of those cells that are preferentially reactivated during retrieval in the HPC, AMY and many other brain regions.

### *1.13.3) Foundational insights from engram work*

Foundational work using the Tet-tag system showed that there is an overlapping population of cells in the AMY that are activated during the acquisition and retrieval of a fear memory (Reijmers et al, 2007). This is in line with work in humans showing stark similarities between the neural correlates of memory encoding and recall (Polyn, 2005; Rugg, 2008). Further, selective ablation or inhibition of an amygdalar fear ensemble interfered with recall of the memory (Han et al 2008**;** Zhou et al 2009). Building upon this, researchers showed that optogenetic reactivation of fear engram cells in the hippocampal

DG was sufficient to drive freezing response and memory recall (Liu & Ramirez, 2012). This suggested that the activation of these memory-bearing cells was able to act as a retrieval cue. Interestingly, labeling DG cells active in a neutral environment (Cxt A) and subsequently optogenetically reactivating them during CFC (Cxt B) increased freezing when the mice were placed back into the original Cxt A, showing that these cells can serve as a CS for the formation of an artificial CS-US association (Ramirez et al 2013; Ohkawa et al, 2015). The cells become active in this new fearful environment and take on that information to become part of the original ensemble, essentially transferring this fear to a never-shocked-before environment. In human epilepsy patients, focal stimulation of the brain can also artificially induce memory recall (Penfield & Perot, 1963). Importantly, the necessity of engram cells was shown with optogenetic inhibition of fear-bearing cells in hippocampal DG, CA1 and CA3 impairing contextual fear memory during retrieval using both the Tet-Tag and TRAP systems (Tanaka et al, 2014; Denny et al, 2014). Foundational work has even used engram labeling techniques to elucidate the progression from encoding to consolidation to recent and remote memory recall across the brain. When a contextual fear memory was labeled in both the HPC and PFC during encoding, recent recall only reactivated the HPC portion of the ensemble, while remote recall resulted in the opposite (Kitamura et al, 2017). More recent work has built upon this finding to show that encoding involves strengthening of connections within HPC ensembles, but through consolidation, excitatory connections between PFC engram cells become progressively strengthened, allowing for decreased reliance on the HPC representation for recall (Lee et al 2023).

### *1.13.4) The allocation hypothesis*

Seminal work has shown that neurons expressing high levels of cAMP-response element binding protein (CREB), a transcription factor, are more likely to 'outcompete' their neighboring cells to become allocated to the engram (Han et al, 2007; Josselyn, 2010). Further, these high-CREB neurons were demonstrated to be more excitable than their neighbors (Zhou et al 2009; Yiu et al, 2014). Using this principle, neurons could be artificially allocated to the engram by increasing their activity before conditioning via optogenetics or chemogenetics in the LA (Han et al, 2007; Hsiang et al, 2014; Yiu et al, 2014; Park et al, 2016). The necessity of these allocated cells to memory retrieval was shown with ablation of CREB-overexpressing neurons with diphtheria toxin (DT) in the amygdala after conditioning decreasing expression of fear (Han et al 2009). With this knowledge that manipulating neuronal excitability can allocate cells to a memory-bearing ensemble, recent work has shown that dCA1 cells are also endogenously more active before an experience (Mocle et al, 2024). Interestingly, they also found that these allocated ('engram') cells ramp in activity at the onset of freezing bouts compared to non-engram cells, in line with our findings from astrocytes and neurons in the BLA and ventral CA1 (vCA1) (Mocle et al 2024; Suthard & Senne, 2023; 2024).

### *1.13.5) Extinction engrams*

One of the major outstanding questions in the engram field was what happens to these neuronal ensembles after the fear is extinguished? Does the original memory inherently change or get erased? Does a new extinction memory form that competes or inhibits the original? Early work demonstrated that pharmacological or optogenetic

reactivation of engram cells tagged during learning was able to 'bring back' the memory after being extinguished, suggesting that some portion of the original memory trace remains even after extinction (Yoshii, Hosokawa & Matsuo, 2017; Lacagnina et al, 2019). Further, repeated optogenetic stimulation of an original fear ensemble was able to accelerate extinction in the training environment, showing that these original cells do undergo changes during the extinction process, becoming more weakly coupled to the aversive stimulus (Khalaf et al, 2018). Interestingly, even repeated optogenetic stimulation of a fear ensemble in the absence of exposure to the training context could induce extinction of the memory (Chen et al, 2019). More recently, calcium imaging in the BLA and DG revealed that fear ensembles decrease their activity in real-time during extinction and are re-engaged during relapse or spontaneous recovery, supporting this idea that the original ensemble is changing throughout extinction but maintains some representation of the fear memory (Zaki & Mau et al, 2022). This further supports earlier work showing that silencing of the fear ensemble was sufficient to impair extinction and maintain maladaptive levels of fear (Khalaf et al, 2018). In parallel, optogenetic inhibition of a newly-formed 'extinction ensemble' in the DG increased fear after extinction and produced spontaneous recovery, showing that a competing extinction engram is generated that co-exists with the original conditioning engram (Lacagnina et al, 2019).

Building upon previous work from the BLA described above, *Ppp1r1b*+ neurons are uniquely activated by contextual fear extinction and inhibited by aversive stimuli during conditioning and recall, while *Rspo2*+ neurons are the opposite (Kim et al, 2016; Zhang, Kim & Tonegawa, 2020). As these *Rspo2*+ cells in the anterior BLA drive

defensive behaviors, while *Ppp1r1b+* cells in the posterior BLA drive appetitive responses, this finding sheds light on 'positive' valenced ensembles dampening the 'negative' aspects of a fear memory during extinction. Specifically, they show that these *Ppp1r1b+* cells are necessary and sufficient to drive fear extinction, suggesting that shifting from fear to safety learning requires a 'positive' valenced extinction ensemble to inhibit the original 'negative' *Rspo2+* fear conditioning ensemble within the BLA.

### *1.13.6) Engrams outside of freezing*

While engram tagging strategies have been mainly utilized to uncover the basis of fear learning and memory, many researchers have used the tagging and manipulation of neuronal ensembles to study their roles in internal and external states, such as reward, anxiety-related behaviors, body regulation (feeding, temperature, etc.), social interaction, and more. Early work showed that optogenetic stimulation of DG engram cells that were labeled during a rewarding experience was sufficient to suppress depression-like behaviors, showing the modulatory power of valenced cellular ensembles in the brain on behavioral state (Ramirez et al, 2015). Interestingly, optogenetic stimulation of fear or reward engrams in the BLA and HPC was sufficient to drive approach or avoidance, respectively, showing that these ensembles can drive behavioral changes outside of freezing (Redondo et al, 2014). With greater specificity, inhibition of vCA1 projections to the NAc, olfactory bulb (OB) and BLA show selective recruitment of vCA1-NAc during social discrimination behavior and recognition of familiar conspecifics (Okuyama et al, 2016). Researchers have further utilized engram strategies to understand the underlying circuits of reward learning and how these undergo maladaptive changes in addiction. For

example, cocaine CPP relies on recruitment of ensembles within the AMY and HPC, where inhibition of neurons labeled during CPP training disrupted memory recall (Hsiang et al, 2014; Trouche et al, 2016; Zhou et al, 2019). Strategic use of engram tagging has enabled projection-specific understanding of addiction circuits, such as preferential strengthening of vCA1-NAc communication being necessary for cocaine CPP memory retrieval (Zhou et al 2019).

*1.14) Organization of dissertation*

The remainder of the dissertation has been organized into three chapters. In Chapter Two, I sought to record real-time astrocytic calcium dynamics in the AMY to understand how these cells are actively involved in the acquisition, retrieval, and extinction of contextual fear. To accomplish this goal, we performed FP recordings of astrocytes within the BLA as mice underwent CFC, recall and extinction. Here, we show that BLA astrocytes are robustly responsive to negative stimuli, such as foot shock, and display changed calcium activity patterns through fear learning and memory. Additionally, astrocytic calcium responses become time locked to the initiation and termination of freezing bouts during fear learning and recall, and become uncoupled from behavior during extinction. We find that astrocytes display calcium dynamics unique to a fear-conditioned context, and chemogenetic inhibition of BLA fear ensembles does not have an impact on freezing behavior or calcium dynamics. These findings show that astrocytes play a key real-time role in fear learning and memory and will allow future investigation into the mechanism behind this coupling of calcium to behavioral responses.

Chapter Three sought to expand the engram field by exploring the real-time role of astrocytes and neurons in the hippocampus across both natural recall and artificial reactivation of a fear memory. Combining these activity-dependent labeling strategies with *in vivo* FP, we studied the interplay between neurons and astrocytes across fear acquisition, natural recall and optogenetic activation of a fear memory or 'engram'. Most excitingly, we find that optogenetic activation of a fear memory is sufficient to induce cellular calcium signatures in neurons and astrocytes that are akin to those seen during natural recall, and these are coupled to meaningful retrieval behavior, such as freezing. These findings will help to advance our understanding of how neurons and astrocytes cooperatively drive behavior during fear recall and provide evidence that optogenetic activation of memories may meaningfully recapitulate hippocampal dynamics during natural fear.

Chapter Four pivoted to higher spatial resolution imaging of astrocytes in the dorsal hippocampus during fear acquisition and retrieval using one-photon calcium imaging. Here, we showed that astrocytes at the single-cell level are shock-responsive, recapitulating our previous findings in other limbic regions of the brain. However, we showed that astrocyte sequences are triggered by foot shock onset during fear acquisition in a similar manner to activity displayed by hippocampal time cells. Further, these sequences reappeared during contextual retrieval only in mice that were re-exposed to the aversive context, but not a novel environment. Finally, these reactivated sequences appear to be driven by reactivated astrocytes that were present across days. Together, these findings provide a novel role for astrocytes in temporal coding within contextual fear conditioning and these sequences may provide functional information that allows for context-specific

retrieval of fear. For all of the experimental chapters described above, I formulated the research plan, designed, and performed experiments, interpreted, and analyzed experimental data, and wrote the published manuscript with my co-authors, where applicable. An in-depth summary of the findings, limitations and future directions are located at the end of each Chapter within the Discussion subheadings.

# CHAPTER TWO: BASOLATERAL AMYGDALA ASTROCYTES ARE ENGAGED IN THE ACQUISITION AND EXPRESSION OF A CONTEXTUAL FEAR MEMORY

Data and portions of the text in this chapter were originally published as:

Suthard, R. L., Senne, R. A., Buzharsky, M. D., Pyo, A. Y., Dorst, K. E., Diep, A. H., Cole, R. H., & Ramirez, S. (2023). Basolateral Amygdala Astrocytes Are Engaged by the Acquisition and Expression of a Contextual Fear Memory. *The Journal of Neuroscience.* 43(27), 4997–5013. https://doi.org/10.1523/JNEUROSCI.1775-22.2023.

## Abstract

Astrocytes are key cellular regulators within the brain. The basolateral amygdala (BLA) is implicated in fear memory processing, yet most research has entirely focused on neuronal mechanisms, despite a significant body of work implicating astrocytes in learning and memory. In the present study, we used *in vivo* fiber photometry in C57Bl/6J male mice to record from amygdalar astrocytes across fear learning, recall, and three separate periods of extinction. We found that BLA astrocytes robustly responded to foot shock during acquisition, that their activity remained remarkably elevated across days in comparison to unshocked control animals, and that their increased activity persisted throughout extinction. Further, we found that astrocytes responded to the initiation and termination of freezing bouts during CFC and recall, and this behavior-locked pattern of activity did not persist throughout the extinction sessions. Importantly, astrocytes do not display these changes while exploring a novel context, suggesting that these observations are specific to

the original fear-associated environment. Chemogenetic inhibition of fear ensembles in the BLA did not affect freezing behavior or astrocytic calcium dynamics. Overall, our work presents a real-time role for amygdalar astrocytes in fear processing and provides new insight into the emerging role of these cells in cognition and behavior.

## 2.1) Introduction

Memory acquisition, recall, and extinction are critical phases for information processing in the brain; disruption of any of these processes can lead to pathological states of cognition and behavior. Fear memories are one of the most well studied forms of memory, and have been shown to recruit numerous brain areas including the hippocampus (HPC) and basolateral amygdala (BLA). Specifically, during Pavlovian fear conditioning, the CA1 and CA3 subregions of the HPC relay information broadly to the amygdala via the ventroangular pathway or through the entorhinal cortex (EC), which also projects to the prefrontal cortex (PFC). The amygdala then is thought to send output to the central medial amygdala (CeM) which in turn sends output to the lateral hypothalamus or periaqueductal gray (PAG) to alter the sympathetic nervous system and gate freezing behavior, respectively. This complex fear circuitry is necessary for proper memory processing and these regions each differentially contribute to the behavioral expression of fear.

Recent work has demonstrated the active involvement of astrocytes in cognition and behavior by regulating synaptic plasticity, supporting metabolic homeostasis, modulating neurotransmitter action, and releasing their own gliotransmitters to exert wide-

ranging effects on the brain (Araque et. al., 2014; Bezzi et. al., 2001; Araque et. al., 2001; Araque et. al., 1999; Haydon et. al., 2001; Perea & Araque, 2005; Perea et. al., 2009; Parpura et. al., 1994; Porter et. al., 1997; Volterra & Meldolesi, 2005; Koizumi, Fujishita & Inoue, 2005; Covelo et. al., 2018; Di Castro et. al., 2011; Fellin et. al., 2004; Durkee et. al., 2019). Broadly, chemogenetic and optogenetic perturbations of astrocytic functioning have been shown to impair or enhance both recent and remote memory in the HPC, amygdala, and PFC (Kol et. al. 2020; Adamsky et. al., 2018; Li et. al. 2020; Martin-Fernandez et. al., 2017; Liao et. al., 2017; Fan et. al., 2021). The effects of these manipulations depend heavily on the brain region of interest, the signaling pathways perturbed and the time point of manipulation during behavior. Mounting evidence suggests that astrocytes may modulate local and projection-specific network activity in memory processes (Kol et. al., 2020; Martin-Fernandez et. al., 2017). For example, a recent study demonstrated that hippocampal dorsal CA1 (dCA1) astrocytic Gq activation during contextual fear conditioning is sufficient to promote long-term potentiation and enhance subsequent recall in mice, whereas neuronal activation does not (Adamsky et. al., 2018). Further research in the BLA has shown that fear conditioning itself downregulates astrocytic Rac1 to facilitate the formation of a conditioned fear memory (Liao et. al., 2017; Fan et. al., 2021). Additionally, BLA astrocytic Gq pathway activation during fear conditioning increased auditory memory, but not contextual memory retrieval, dissociating the role of these cells in multiple types of aversive learning (Lei et. al., 2022). Finally, Gq activation of astrocytes in the BLA after cued fear extinction training decreases freezing levels during extinction recall 24 hours later (Shelkar et. al., 2021). This evidence supports

bidirectional astrocyte-neuron communication in multiple subdivisions of the amygdala and suggests their active control over the functional connectivity of the amygdala with other canonical fear-learning ‘hubs’.

Despite the recent interest in astrocytic contributions to memory, these studies predominantly use perturbation approaches (e.g. cell-type-specific activation or inhibition of cellular activity), whereas neuronal investigations may now multiplex these causal approaches with optical imaging to gain real-time insight on cellular activity during behavior. Still, there are relatively few studies utilizing these approaches, even with newer genetically-encoded calcium indicators (GECIs) and transgenic mouse lines that are capable of preferentially targeting astrocytes for dynamic calcium recordings across behavior (Corkrum et. al., 2020; Lin et. al., 2021; Qin et. al., 2020; Lines et. al., 2020; Tsunematsu et. al., 2021). Understanding the activity of astrocytes in real-time is essential for understanding cognition, especially given that the brain predominantly consists of glia.

The BLA is a key hub for valence-specific memories. Prior work has shown that the BLA is necessary for the encoding and retrieval of the emotional component of fearful experiences, and lesioning experiments have shown that its disruption strongly inhibits proper emotional responses (Zhang & Li, 2018; Maren, Ahranov, & Fanselow 1996; Maren 1999). Furthermore, the BLA has also been shown to be necessary for the acquisition and extinction of contextual fear memory in mice, suggesting it plays a key role in every stage of fear learning. Despite the relatively large body of literature implicating the BLA in fear conditioning, almost all of this work has focused on neuronal responses, and there is currently a limited understanding on how astrocytic calcium responses in the BLA manifest

across fear acquisition, recall, and contextual extinction. Furthermore, previous work suggests that perturbation of BLA neurons during fear recall is capable of diminishing freezing behaviors (Han et al. 2009, Gore et al. 2015; Liu et. al., 2022; Redondo et. al., 2014), although coupled activity at the astrocyte-neuron interface remains relatively understudied activity.

To address this, we use freely-moving fiber photometry (Gunaydin et. al., 2014; Cui et. al., 2014) to record population-level astrocytic calcium dynamics across the classic contextual fear conditioning (CFC) paradigm. First, we find that astrocytes in the BLA are shock-responsive, which suggests that astrocytes in this amygdalar sub-region process salient and/or aversive-related stimuli. Next, we find that astrocytes in the shock condition displayed unique calcium events across fear learning compared to the unshocked control group. Then we observed calcium peri-events at the initiation and termination of freezing bouts during recall, but this did not persist into extinction sessions. We then utilized activity-dependent and chemogenetic-mediated inhibition of BLA cells to determine if this affected animal behavior and/or astrocytic signaling, and found no change in freezing or real-time dynamics. Finally, astrocytic changes were associated with the fear conditioned environment, as in a novel context we observed no differences in exploratory behaviors, nor any changes in calcium event characteristics across the shock and no-shock groups.

Together, our experiments provide a more comprehensive understanding of the contributions of glial cells to learning and memory processes. Perturbation of these cells during extinction memory formation and maintenance may pave the way for more

successful therapeutic interventions in humans with disorders of maladaptive fear learning, such as Post-Traumatic Stress Disorder (PTSD).

## 2.2) Materials and Methods

### *2.2.1) Subjects*

Wild type, male C57BL/6J mice (P29-35) weight 17-19g; Charles River Laboratories) were housed in groups of 4-5 mice per cage at the time of surgery. The animal facilities (vivarium and behavioral testing rooms) were maintained on a 12:12 hour light cycle (0700-1900). Mice received food and water *ad libitum* before and after surgery. Following surgery, mice were group-housed with littermates and allowed to recover for 3 weeks before experimentation. All subjects were treated in accord with protocol 201800579 approved by the Institutional Animal Care and Use Committee (IACUC) at Boston University. All n-values for each experimental group (shock, no-shock) can be found within the legends of each figure.

### *2.2.2) Stereotaxic Surgery*

For all surgeries, mice were anesthetized with 3.0% isoflurane inhalation during induction and maintained at 1-2% isoflurane inhalation through stereotaxic nose cone delivery (oxygen 1L/min). Ophthalmic ointment was applied to the eyes to provide adequate lubrication and prevent corneal desiccation. The hair on the scalp above the surgical site was removed using Veet hair removal cream and subsequently cleaned with alternating applications of betadine solution and 70% ethanol. 2.0% lidocaine hydrochloride (HCl) was injected subcutaneously as local analgesia prior to midsagittal

incision of the scalp skin to expose the skull. 0.1mg/kg (5mg/mL) subcutaneous (SQ) dose of meloxicam and 0.1-0.2 mL of sterile saline were administered at the beginning of surgery. For fiber photometry implant surgeries, animals received a unilateral craniotomy with a 0.5-0.6 mm drill-bit for basolateral amygdala (BLA) injections. A 10μL airtight Hamilton syringe with an attached 33-gauge beveled needle was slowly lowered to the coordinates of BLA: -1.40 anteroposterior (AP), -3.20 mediolateral (ML) and -4.80 dorsoventral (DV). All coordinates are given relative to bregma (mm). A volume of 500nL of AAV-GfaABC1D-cyto-GCaMP6f-SV40 (Penn Vector Core) was injected at 50nL/min using a micro-infusion pump for the BLA coordinate (UMP3; World Precision Instruments). After the injection was complete, the needle remained at the target site for 5-7 minutes post-injection before removal. Following viral injection, a unilateral optic fiber (200μm core diameter; 1.25mm ferrule diameter) was implanted at the site of injection. The implant was secured to the skull with a layer of adhesive cement (C&M Metabond) followed by multiple layers of dental cement (Stoelting). Following surgery, mice were injected with a 0.1mg/kg intraperitoneal (IP) dose of buprenorphine for pain management. They were placed in a recovery cage with a heating pad on medium heat until fully recovered from anesthesia. To allow for recovery and viral expression, we waited 3 weeks before beginning our behavioral paradigm. Histological assessment verified viral targeting and data from off-target injections were not included in further analyses.

For activity-dependent (‘engram’) virus surgeries, mice were placed on doxycycline (Dox) diet for 72 hours prior to surgery. The same injection, viral volume and fiber photometry implantation methods were used as described above, with the addition of

200-250nL AAV9-c-fos-tTA-TRE-hM4Di-mCherry or AAV9-c-fos-tTA-TRE-mCherry virus in bilateral BLA to allow for inhibition of the neuronal fear engram during recall.

*2.2.3) Fiber Photometry*

A 470-nm LED (Neurophotometrics; FP3002) delivered an excitation wavelength of light to astrocytes expressing GCaMP6f via a single fiber optic implant. The emitted 530-nm signal from the indicator was collected via this same fiber, spectrally-separated using a dichroic mirror, passed through a series of filters, and was focused on a scientific camera. Calcium-independent isosbestic signals were simultaneously captured by alternating excitation with 415-nm LED to dissociate motion, tissue autofluorescence, and photobleaching from true changes in fluorescence. All wavelengths were interleaved and collected simultaneously using Bonsai (**Lopes et. al., 2015**). The sampling rate for the signals was 28Hz (28 frames per second). Time series were analyzed using an in-house pipeline and fluorescence signals were normalized to the median for comparison of event amplitude (peak height; % dF/F), frequency (Hz), total fluorescence (area under the curve; AUC) and duration (full-width half maximum; FWHM). Statistical analyses were performed using Python and data reported as Mean ± SEM.

*2.2.4) Behavioral Testing*

*Fear Conditioning, Recall, Extinction Experiments:*

On Day 1, mice were placed into the shock context (Cxt A) where they underwent a 360s contextual fear conditioning session. Foot shocks (1.5mA, 2s duration) were

administered at the 120, 180, 240 and 300 second time points at 1.5mA intensity. On Day 2, mice were placed back in Cxt A for 360s of recall where they received shock on the previous day. There were no shocks administered during this session. On Days 3- 5, mice were placed back in Cxt A for 900s without shock administration to extinguish the fear memory across days. On Day 6, mice underwent a 360s session of exploration in a novel open field context (Cxt B) to assess the context-dependent nature of astrocytic calcium changes, if present. At the completion of testing, mice in the no-shock group were administered a single 1.5mA foot shock to confirm the presence of calcium signal.

Days 1-5 took place in mouse conditioning chambers (18.5 x 18.5 x 21.5cm)(Coulbourn Instruments) with metal-panel side walls, plexiglass front and rear walls and a stainless-steel grid floor composed of 16 grid bars that were connected to a precision animal shocker that delivered the four foot shocks. A video camera was mounted on a tripod in a front-facing orientation to the conditioning chamber for fear conditioning, recall and extinction. Day 6 took place in an open field arena (61cm x 61cm) with black plastic walls and a taped area (45cm x 45cm) in the middle delineating a "center" region. For this session, a top-down camera was used to record behavioral video during the session. The chambers were cleaned with 70% ethanol solution prior to each animal placement. All behavioral testing was performed during the animal's light-cycle.

*Neuronal engram behavioral experiments:*

Mice were separated into two groups: hM4Di (experimental) and mCherry (control). On Day 1, mice were taken off of their Dox diet for 48 hours to open the 'tagging

window'. On Day 3, mice were placed in the same contextual fear conditioning (CFC) chamber described above, where they received four, 1.5mA foot shocks for 360 seconds. All mice were placed immediately back on Dox after this session. On Day 4, mice were placed back in the same conditioned context for a 360 second session of recall. Both groups of mice received a single I.P. injection (3 mg/kg) of clozapine-N-oxide (CNO) 30 minutes prior to the session to inhibit the 'tagged' fearful experience. 90 minutes after the start of recall, mice were transcardially perfused to capture peak cFos protein levels in the BLA due to inhibition of the tagged neuronal ensemble. Mice had calcium dynamics recorded across all three sessions using fiber photometry. For these sessions, a front-facing video camera was used to obtain behavioral videos during fear conditioning and recall, and a top-down facing video camera was used to obtain home cage video.

*Chemogenetic Parameters:*

For chemogenetic silencing of bilateral BLA fear engram neurons, we used the inhibitory Designer Receptor Exclusively Activated by Designer Drugs (DREADDs), hM4Di. hM4Di drives inhibition of infected neurons when bound to the ligand, CNO (Sigma-Aldrich). A 0.6 mg/mL solution of CNO was prepared in sterile saline and 0.5% dimethyl sulfoxide (DMSO). All mice were I.P. injected with sterile saline for five days prior to experimentation for habituation. On the day of contextual recall, mice were injected with a 3 mg/kg dose of CNO solution 30 minutes prior to the start of the session to capture peak drug concentration.

*2.2.5) Immunohistochemistry*

On Day 6, mice were overdosed with 3% isoflurane and perfused transcardially with cold (4°C) phosphate-buffered saline (PBS) followed by 4% paraformaldehyde (PFA; pH = 7.4) in PBS. Brains were extracted and kept in PFA at 4°C for 24-48 hours and transferred to a 30% sucrose in PBS solution. Brains were sectioned into 50µm thick coronal sections with a vibratome and collected in cold PBS or 0.01% sodium azide in PBS for long-term storage. Sections were washed three times for 10-15 minutes with PBS to remove 0.01% sodium azide used for storage. Vibratome sections were incubated for 2 hours in PBS combined with 0.2% Triton (PBST) and 5% bovine serum albumin (BSA) on a shaker at room temperature. Sections were incubated in the primary antibodies (1:1000 mouse monoclonal anti-GFAP [NeuroMab]; 1:1000 rabbit polyclonal anti-Iba1 [Wako]; 1:500 guinea pig anti-NeuN [SySy]) diluted in PBST/1% BSA at 4°C for 24 or 48 hours. The slices were washed three times for 10-15 minutes each in 1xPBS. The secondary antibodies were diluted in secondary antibody solution (PBST/1% BSA) and incubated for 2 hours at room temperature. The following secondary antibodies were used: 1:1000 Alexa 555 anti-mouse [Invitrogen], 1:1000 Alexa 555 anti-rabbit [Invitrogen], 1:200 Alexa 555 anti-guinea pig [Invitrogen]. The sections were then washed three times with 1xPBS or PBST for 10-15 minutes each and mounted using Vectashield Mounting Medium with DAPI (Vector Laboratories). Once dry, slides were sealed with clear nail polish on each edge and stored in a slide box in the fridge (4°C). Mounted slices were imaged using a confocal microscope (Zeiss LSM800, Germany).

For activity-dependent (‘engram’) experiments, immunohistochemistry was performed as described above with the use of the following primary (1:1000 chicken anti-GFP [Invitrogen], 1:1000 guinea pig anti-RFP [SySy]) and secondary (1:200 Alexa 488 goat anti-chicken [Invitrogen], 1:200 Alexa 555 goat anti-guinea pig [Invitrogen]) antibodies to confirm co-expression of hM4Di-mCherry (RFP) and GfaABC1D-GCaMP6f (GFP) in the BLA. cFos protein counts across hM4Di and mCherry groups were performed using the additional primary antibody (1:1000 rabbit polyclonal anti-cFos [SySy]) and secondary antibody (1:200 Alexa goat anti-rabbit 647 [Invitrogen]).

Brains from all mice used in fiber photometry experiments were analyzed to check adequate fiber location and proper and selective viral expression. Animals that did not meet the criteria for proper fiber location and virus expression were discarded.

*2.2.6) Imaging and Cell Counting*

Imaging was performed using a Zeiss LSM 800 epifluorescence microscope with 10x and 20x objectives using the Len2.3 software. Full slice images of BLA GfaABC1D-GCaMP6f (green) and DAPI (Figure 1C) were captured with a 10x objective (6554 x 9319 pixels) along with a zoomed-in (1024 x 1024 pixels) single-tile z-stack at 20x magnification (Figure 1B).

The cellular specificity and penetrance of the GCaMP6f viral vectors (Figure 1D-F) was tested by immunohistochemical analysis of the BLA. These images of NeuN, Iba-1 and GFAP were captured in z-stacks of the BLA at 20x magnification. 20x magnification, single-tile (1024 x 1024 pixels) representative images are shown (Figure 1B). Cell counts

for NeuN, Iba-1, GFAP and overlaps were performed using Ilastik, a machine-learning-based image analysis tool (Berg et. al., 2019). Of the 2256 cells expressing GCaMP6f (n = 3 mice; 3 slices), 2242 were astrocytes (identified by GFAP), resulting in a specificity of 99.4%. Of the 662 cells expressing GCaMP6f (n=3 mice; 3 slices), 4 were microglia (identified by Iba-1), resulting in a specificity of 0.6%. Of the 1064 cells expressing GCaMP6f (n = 3 mice; 3 slices), 0 were neurons (identified by NeuN), resulting in a specificity of 0%. Finally, of 2381 GFAP+ astrocytes, 2251 were GCaMP6f+ (n=3 mice; 3 slices), resulting in a penetrance of 98.49%.

For engram experiments, bilateral BLA was imaged at 20x magnification to confirm expression of neuronal hM4Di and mCherry and single-tile (1024 x 1024 pixels) images were shown (Figure 7B; Left). For cFos counts, bilateral BLA was imaged at 20x magnification for n = 3 mice/group x 6 ROIs each. In FIJI (ImageJ), the images were maximum z-projected, each ROI of the BLA was manually isolated and cropped using the polygon tool, and the DAPI and cFos channels were separated for automated counting in Ilastik. cFos+ cells were normalized to the DAPI+ cells for each ROI and averaged across each mouse to generate an average %cFos/DAPI+ (Figure 7B; Right).

*2.2.7) Behavioral Analysis*

An automated video tracking system, Any-Maze, was used for supervised analysis of freezing bout initiation and termination in the shock context (Cxt A), as well as the total distance traveled, mean speed, number of entries into the center and total time spent in the center of the open field (Cxt B). Additionally, the pose estimation algorithm, DeepLabCut,

was used to perform unbiased animal behavioral evaluation of kinematics (position, acceleration, velocity) for use in generalized linear modeling (GLM) (Mathis et. al., 2018). This behavioral data was time locked to our fiber photometry time series data for all analyses.

*2.2.8) Statistical and Fiber Photometry Analysis*

All statistical analysis and subsequent photometry analysis was performed via custom python scripts freely available at https://github.com/rsenne/RamiPho. Our environment was built off of scipy (ver. 1.7.3), statsmodels (ver. 0.13.2), numpy (ver. 1.22.3), pandas (ver. 1.4.2), matplotlib (ver. 3.5.1), numba (ver. 0.55.2), and seaborn (ver. 0.11.2).

All photometry signals were baseline corrected using an adaptive iteratively reweighted penalized least squares method (Zhang, Chen, & Liang, 2010). We then performed a simple kernel smoothing to increase the signal to noise ratio. For “event detection” we used a method published in prior literature (Howe et al. 2019). DF/F was calculated by subtracting the median of the trace from the current fluorescence value and then dividing by the median, giving a percent difference from the median or “baseline”. We then found any peaks greater than 1 standard deviation away from the mean, in both the positive and negative direction. We then determined the minimum width such that the ratio of positive to total transients (negative and positive) was greater than or equal to 0.99. Any transients below this width were subsequently discarded.

For peri-event analysis, we used a tCI method as proposed previously (Jean-Richard-dit-Bressel, Clifford & McNalley, 2020). For each window of interest, we calculated a 95%, 99% and 99.9% confidence interval. If the CI did not contain the null assumption (dF/F = median of the event window), for a period greater than 0.5 s we concluded that a significant peri-event occurred. This type of method does not allow an exact p-value and thus is omitted from the text.

For generalized linear modeling (GLM), we fit a model using a Gaussian family and identity link function. We hypothesized that the calcium activity (dF\F) could be explained by a combination of the isosbestic signal, velocity, and acceleration (up to the third degree), the binary freezing values, the animal identification number, and an interaction effect between the animal and a series of basis spline functions for: the 10 seconds following shock presentation, and 5 seconds following initiation of freezing behavior, and 5 seconds following the termination of freezing. We chose to fit a singular model as opposed to individuals models for each model because we wanted to maximize the number of samples to get better fits for coefficients that should be shared across animals (e.g. the contribution of velocity to the trace) while still including the animal specific terms to account for individual variability within the SNR of each trace (e.g. the interaction effect between the animals and splines will give unique coefficients for each animal helping to model discrete events better). Thus, our model can be summarized as follows:

$$y_i = \beta_o + \beta_1 I + \beta_2 F + \sum_j^{\beta_{fin}} \sum_n^{An_{tot}} \beta_j An_n + \sum_j^{\beta_{fin}} \sum_{k=1}^{3} \beta_j A^k +$$

$$\sum_j^{\beta_{fin}} \sum_{k=1}^{3} \beta_j V^k + \sum_j^{\beta_{fin}} \sum_n^{An_{tot}} \sum_i^{Sp} \beta_j An_n * P_i + \epsilon$$

Where I is the isosbestic channel, F is the freezing (binary: 1 is freezing, else 0), An is a dummy variable encoding animal ID, A is acceleration, V is velocity, P is our polynomial spline functions, k degree of the polynomial function applied to the kinematic variables, An_tot is the total number of animals, Sp is the total number of splines, and \beta_fin is the final index for the specific summation. Or more simply stated:

dF/F ~ Isosbestic + Freezing + Animal + Acceleration Functions + Velocity Functions + Animal Specific Splines + Error.

The above model is now considered the "full model" such that this is the highest order model possible for our analysis. To do model selection, simpler models were tested, and when nested, a maximum likelihood ratio test was performed (MLRT) to determine the final model. If comparing two models that were not nested, the Akaike Information Criterion (AIC) was used.

**2.3) Results**

Astrocytes in the basolateral amygdala are actively involved in fear memory (Liao et. al., 2017; Fan et. al., 2021; Lei et. al., 2022; Shelkar et. al., 2021; Stehberg et. al., 2012), but their real-time dynamics during the acquisition and maintenance of conditioned fear in mice is relatively unknown. We monitored astrocyte calcium levels in the BLA using fiber-photometry in freely behaving mice across the acquisition, retrieval, and extinction of conditioned fear. Wild type mice were injected unilaterally with AAV-GfaABC1D-cyto-GCaMP6f to express the genetically-encoded calcium indicator GCaMP6f selectively in astrocytes (Figure 1A-C). To quantify the penetrance and specificity of our viral system,

we co-labeled GCaMP6f+ cells with GFAP, Iba-1 and NeuN, markers for astrocytes, microglia, and neurons, respectively (Figure 1D-F). Of 2381 GFAP+ cells, 2251 were GCaMP6f+ (n=3; 4 slices/mouse), resulting in a penetrance of 98.49% (Figure 1D, F). Of 662 GCaMP6f+ cells, 4 were Iba1+, resulting in a specificity of 0.604% for microglia (Figure 1E-F). Of 1064 GCaMP+ cells, 0 were NeuN+, resulting in a specificity of 0.0% for neurons (Figure 1E-F). Finally, of 2256 GCaMP+ cells, 2242 were GFAP+, resulting in a specificity of 99.4% for astrocytes (Figure 1E-F).

To test the hypothesis that astrocytes play an active role in the acquisition and maintenance of contextual fear, we used *in vivo* fiber photometry to record their activity across all experimental days of our behavioral task (Figure 1G-H). Recent literature using calcium imaging in ventral hippocampus (vHPC) has shown that a subset of BLA-vHPC projecting neurons were responsive to aversive shock during CFC (Jimenez et. al., 2020). This provides ample evidence that BLA neurons and astrocytes are also likely to be shock-responsive. On Day 1, mice underwent contextual fear conditioning with the administration of 1.5mA foot shocks at 120, 180, 240 and 300 second timepoints (Figure 1H). To assess whether BLA astrocytes responded specifically to footshock, we performed peri-event analysis to determine if calcium transients were temporally locked to footshock. We used a tCI confidence interval method to classify significant peri-events around a time-point of interest as previously described (Jean-Richard-dit-Bressel, Clifford & McNalley, 2020; *See Methods*). Astrocytes in the shock group displayed robust increases in population-level calcium at the onset of each foot shock during the session compared to the no-shock condition, as shown by a representative calcium time series (% dF/F) from each group

(Figure 2A) and raster plots (z-scored % dF/F) including all mice from each group (Figure 2D-E). Further analysis revealed that the shock group had significantly increased % dF/F from baseline after the onset of each foot shock compared to the no-shock condition (Footshock peri-event analysis; 99% confidence interval (CI))(Figure 2B). Specifically, the shock group had an increase of 44.6% dF/F from baseline after the onset of each footshock, on average, compared to 1.6% increase dF/F for the no-shock condition (Independent samples t-test; Welch's correction, $p=0.0022$) (Figure 2C).

We next tested the hypothesis that astrocytes modulate their behavior in response to the initiation and/or termination of freezing. There were significant peri-events, where the event started prior to the initiation of freezing (Freeze initiation peri-event analysis; 99% CI)(Figure 2F) and the termination of freezing (Freeze termination peri-event analysis; 99% CI), which indicates that astrocytic signaling becomes coupled to freezing behavior during fear memory acquisition (Figure 2G). Behaviorally, mice in the shock group had a higher freezing across the 360s session, compared to the no-shock group that did not experience a foot shock (Independent t-test; $p<0.0001$)(Figure 2H). The shock group successfully acquired fear across the CFC session compared to the no-shock condition (Two-way ANOVA with repeated measures (RM); Interaction: $F (5, 80) = 10.14$, $p<0.0001$; Time bin: $F (1.750, 28.00) = 13.02$, $p=0.0002$; Group: $F (1, 16) = 23.59$, $p=0.0002$; Subject: $F (16, 80) = 4.593$, $p<0.0001$)(Figure 2H). *Post-hoc* analysis demonstrated significant group differences in freezing at the 180, 240, 300 and 360 second time bins (Sidak's multiple comparisons: 180s: $p=0.0167$; 240s: $p=0.0015$; 300s: $p<0.0001$; 360s: $p<0.0001$)(Figure 2H).

We calculated event metrics such as peak height, full-width half max (FWHM), area under the curve (AUC), and frequency (events/minute) for shock and no-shock groups. The shock group had significantly increased event peak height, increased AUC, and decreased full-width half max (FWHM) compared to no shock during CFC ([Peak height: Independent t-test; Welch's correction, p=0.0019][AUC: Independent t-test; Welch's correction, p=0.0011][FWHM: Independent t-test; p<0.0001][Frequency: Independent t-test; p=0.069 (ns)](Figure 2I-L).To further supplement these analyses, we tested if the astrocytic calcium signals could be decoded as a linear combination of the isosbestic channel, freezing, animal identification number (ID), kinematics, and a set of polynomial spline functions to model the shock response, and the initiation and termination of freezing bouts. For a full elaboration of the model and model selection, see *Methods Section 2.8*. We found that during fear conditioning, the most parsimonious model that could explain the most variability in the dataset contained only the animal specific splines and kinematic information up to the third degree, meaning that these signals almost entirely encode the shock information and some amount of motion related output. ($R^2_{CS}$=0.9988)(Figure 2M). Together, the calcium events for the shock condition (i.e. higher amplitude, higher total fluorescence, shorter duration events) suggest that astrocytes become more active after the presentation of a salient stimulus, as suggested by previous literature demonstrating that these cells in dCA1 are responding in a stimulus-dependent manner (Adamsky et. al., 2018).

Recent studies have shown that manipulation of astrocytes during retrieval of a conditioned fear memory does not affect recent or remote memory recall, though their

activity within a given session remained unmeasured (Adamsky et. al., 2018; Kol et. al., 2020). To that end, we investigated the real-time dynamics of these cells in mice that received foot shock vs. neutral exposure to the same context. On Day 2 of our experiment, mice underwent contextual recall without the presence of the unconditioned stimulus (US; foot shock)(Figure 1H). When comparing population-level calcium activity across the shock and no-shock groups, we observed stark differences in the engagement of astrocytes (Figure 3A-B, D). Specifically, we observed that the presence of the US (i.e. footshock) during fear conditioning continued to engage astrocytes when placed back in the original context, while the no-shock group displayed low levels of calcium activity. As the US is the most salient manipulated variable between these two groups, we speculate that astrocytes may be engaged in a learning-dependent manner within the basolateral amygdala (BLA). We also tested the hypothesis that astrocytes modulate their behavior in response to the initiation and/or termination of freezing. There were significant peri-events, where the event started prior to the initiation of freezing (Freeze initiation peri-event analysis; 99% CI)(Figure 3C) and immediately after the termination of freezing (Freeze termination peri-event analysis; 99% CI)(Figure 3E). Behaviorally, mice in the shock group exhibited increased freezing compared to the no-shock condition that did not receive the CS-US pairing (Mann-Whitney U-test; $p<0.0001$)(Figure 3F). Across the recall session, mice in the shock group maintained higher levels of freezing compared to no-shock controls (Two-way ANOVA RM; Interaction: $F (5, 80) = 1.163$, $p=0.3346$; Time Bin: $F (5, 80) = 1.906$, $p=0.1024$; Group: $F (1, 16) = 93.18$, $p<0.0001$; Subject: $F (16, 80) = 8.924$, $p<0.0001$) (Figure 3G). *Post-hoc* analysis across groups supported significantly higher levels of

freezing in the shock condition during recall across all time bins (Sidak's multiple comparisons: 60s: $p<0.0001$; 120s: $p<0.0001$; 180s: $p<0.0001$; 240s: $p<0.0001$; 300s: $p<0.0001$; 360s: $p<0.0001$) (Figure 3G). Furthermore, to quantify these differences in the traces across groups, we calculated the same average event metrics mentioned above (i.e. peak height, FWHM, AUC, frequency). The shock group had increased average peak height, decreased FWHM, increased AUC, and there were no differences in frequency of events across the session ([Peak height: Independent t-test; Welch's correction, $p=0.0009$][AUC: Independent t-test; Welch's correction, $p=0.0156$][FWHM: Independent t-test; Welch's correction, $p=0.0005$][Frequency: Independent t-test; Welch's correction, $p=0.3642$).(Figure 3H-K). This suggests that after context-shock association, astrocytes retain similar calcium dynamics on the following day when placed back in the conditioned environment in the absence of shock. We then fit a Gaussian generalized linear model (GLM) as previously described, to determine which variables best accounted for our calcium signal. Interestingly we saw that the kinematic information, freezing, freezing initiation and termination splines, and animal information best accounted for the recall data ($R^2_{CS}=0.3059$)(Figure 3L). This indicates that during recall there does not seem to be any temporal encoding of the shock that we can detect with this analysis, and further suggests that the activity of these astrocytes is tethered to freezing bouts.

To further evaluate the experience-dependent role of astrocytic calcium across the extinction of contextual fear, mice underwent three days of extinction on Days 3-5 of our behavioral paradigm (Figure 1H). When comparing astrocytic calcium levels during extinction, we observed higher population activity in the shock group in the absence of the

original US compared to the no-shock condition across all three days (Figure 4A-I). This suggests that astrocytes are continuing to be engaged in the shock group, and perhaps in a memory-dependent manner as an extinction memory is being formed across days. The no shock group displayed minimal calcium activity, which may be due to continued exploration of a novel environment as it becomes familiar (Qin et. al., 2020). Furthermore, to quantify these differences across groups, we calculated event metrics for each extinction session. For extinction day 1, the shock condition had calcium events with increased peak height, increased AUC, decreased FWHM (i.e. duration of event), and decreased frequency ([Peak height: Independent t-test; Welch's correction, $p=0.0016$][AUC: Independent t-test; Welch's correction, $p=0.0036$][FWHM: Mann-Whitney U-test, $p=0.0019$][Frequency: Independent t-test, $p=0.0253$])(Figure 4J-M). For extinction day 2, the shock condition had calcium events with increased peak height, increased AUC, decreased FWHM and no difference in frequency ([Peak height: Independent t-test, $p=0.0001$][AUC: Independent t-test, $p<0.0001$][FWHM: Mann-Whitney U-test, $p=0.0043$][Frequency: Independent t-test, $p=0.2050$])(Figure 4J-M). Finally, for extinction day 3, the shock condition had calcium events with increased peak height, but no significant differences in FWHM, AUC or frequency compared to no-shock controls ([Peak height: Independent t-test, $p=0.0010$][AUC: Independent t-test; Welch's correction, $p=0.126$][FWHM: Independent t-test, $p=0.1447$][Frequency: Independent t-test, $p=0.3851$)(Figure 4J-M). Interestingly, this suggests that astrocytes are initially impacted by the presence of the foot shock during CFC, but do not adapt further across extinction days. To further investigate astrocytic calcium responses to freezing behaviors, peri-event metrics for the initiation and

termination of freezing were calculated as previously performed in contextual recall. Interestingly, astrocytic calcium in the shock group was not responsive to the initiation or termination of freezing behavior for all extinction sessions (Freeze initiation and termination peri-event analysis; ns)(Figure 5A-B, D-E, G-H). Behaviorally, mice in the shock group exhibited higher average levels of freezing than the no-shock condition group for all three days ([Extinction 1: Independent t-test; Welch's correction, $p<0.0001$][Extinction 2: Independent t-test; Welch's correction, $p=0.0042$][Extinction 3: Independent t-test; Welch's correction, $p=0.0123$])(Figure 5J). For each extinction session, shocked mice displayed higher levels of freezing at each time bin than no-shock controls ([Extinction 1: Two-way ANOVA RM; Interaction: $F (14, 210) = 1.140$, $p=0.3247$; Time bin: $F (4.530, 67.95) = 1.726$, $p=0.1467$; Group: $F (1, 15) = 22.92$, $p=0.0002$; Subject: $F(15, 210) = 18.83$, $p<0.0001$)][Extinction 2: Two-way ANOVA RM; Interaction: $F (14, 168) = 1.204$, $p=0.2765$; Time Bin: $F (4.306, 51.68) = 1.364$, $p=0.2574$; Group: $F (1, 12) = 18.86$, $p=0.0010$; Subject: $F (12, 168) = 30.92$, $p<0.0001$][Extinction 3: Interaction: $F (14, 168) = 0.9191$, $p=0.5395$; Time bin: $F (3.186, 38.23) = 1.160$, $p=0.3392$; Group: $F (1, 12) = 12.14$, $p=0.0045$; Subject: $F (12, 168) = 25.16$, $p<0.0001$])(Figure 5C, F, I). Specifically, *post-hoc* analysis for extinction days revealed specific time bin differences across groups, and this declines across extinction days ([Extinction 1: Sidak's multiple comparisons; 120s: $p=0.0470$; 180s: $p=0.0202$; 240s: $p=0.0016$; 300s: $p=0.0013$; 360s: 0.0002; 420s: $p=0.0003$; 480s: $p=0.0007$; 540s: $p=0.0020$; 600s: $p=0.0028$; 660s: $p=0.0094$; 720s: $p=0.0073$; 780s: $p=0.0155$; 900s: $p=0.0105$][Extinction 2: Sidak's multiple comparisons; 240s: $p=0.0039$; 300s: $p=0.0187$; 420s: $p=0.0181$][Extinction 3: Sidak's multiple

comparisons; 360s: p=0.0094])(Figure 5C, F, I). We again fit a GLM to determine if any variables could partially describe our calcium signals. We found that the best fit model included the isosbestic channel and kinematic information($R^2_{CS}$=0.1536)(Fig 5K). Interestingly, freezing initiation and termination splines no longer significantly explained any variance within the model, suggesting the astrocytic signals were becoming decoupled to these moments. Through repeated exposures to the context, while calcium events are still present, the amount of information that is able to be decoded from them decreases, suggesting that these signals are more relevant to internal states. Overall, our data suggest that astrocytic calcium remains elevated even as freezing levels decline naturally across extinction sessions.

To further explore the memory-dependent nature of the observed astrocytic calcium changes, a subset of mice from the shock and no-shock groups were placed into a novel open field context (Cxt B) on Day 6 of our behavioral paradigm while recording astrocytic calcium (Figure 1H; Figure 6A-C). Here, we did not observe any significant differences in distance traveled, mean speed, number of center entries or total time spent in the center of the open field across shock and no-shock conditions ([Distance: Independent t-test, p=0.2773][Mean speed: Independent t-test; p=0.2750 ][Center entries: Independent t-test, p=0.3681][Center time: Independent t-test; p=0.42547])(Figure 6D-G). Further, most mice in both groups did not freeze at all for the entirety of the open field session; thus, we did not further analyze freezing behavior between groups or perform peri-event analysis with astrocytic calcium for freezing initiation or termination, as performed with other sessions. Most importantly, we assessed calcium event metrics during this session to observe if

changes observed during contextual fear learning and extinction are due to an enhancement in activity maintained over time. Here, we did not observe any significant differences in the peak height, AUC, FWHM or frequency of calcium events across the shock and no-shock conditions ([Peak height: Mann-Whitney U-test, p=0.3429][FWHM: Independent t-test, p=0.7049][AUC: Independent t-test, p=0.6321][Frequency: Independent t-test, p=0.3262])(Figure 6H-K). This suggests that astrocytic calcium activity changes due to shock are context-dependent and these cells are storing information related to the memory of the aversive experience.

To further elucidate the role of astrocytes in context-dependent memory recall, we utilized the Tet-Tag activity-dependent labeling strategy to chemogenetically inhibit a fear memory while simultaneously performing astrocytic fiber photometry recordings (Figure 7A; left). This system relies on the coupling of the *cfos* promoter to the tetracycline transactivator (tTA), which in its protein form, binds directly to the tetracycline response element (TRE) in a doxycycline (Dox)-dependent manner and can drive expression of a protein of interest (e.g. hM4Di and/or mCherry)(Figure 7A; left). Moreover, the expression of the Designer Receptor Exclusively Activated by Designer Drugs (DREADDs), hM4Di, allows for chemogenetic silencing of the tagged experience (i.e., fear) during recall. To confirm successful perturbation of the hM4Di-expressing ‘engram’ neurons in bilateral BLA, we sacrificed mice 90 minutes after the start of the behavioral recall session to capture peak endogenous cFos protein levels. We found that across the groups, there was a significant increase in cFos+ cells in the hM4Di compared to the mCherry controls (Independent t-test; p=0.0023) (Figure 7B). This increase in cFos with inhibition of a

cellular population in the BLA may seem counterintuitive, but it has become clear in recent studies that modulation of neurons with chemogenetics results in differential effects on cFos and behavior. For example, inhibition of BLA engram cells during chronic hippocampal stimulation resulted in equivalent levels of cFos across the hM4Di and control groups (Chen et. al., 2019). This paper posits that CNO may have induced 'rebound' activity in the neighboring non-tagged cells of the BLA through local circuit mechanisms. Additionally, previous work from our lab has shown that chemogenetic inhibition of engram cells in dorsal CA1 of the HPC increased cFos in neighboring non-engram cells, which we also believe points to a local circuit "rebound" of neuronal activity in response to inhibition (Trouche et al. 2016; Grella et. al., 2020).

As shown in our experiments above, we began by performing simultaneous astrocytic calcium recordings with fiber photometry through the expression of AAV5-GfaABC1D-cyto-GCaMP6f in the unilateral BLA (Figure 7A; left). Prior literature has demonstrated that manipulation of the BLA with perturbation techniques impacts behavioral freezing levels typically associated with context-dependent recall (Han et. al., 2009; Gore et. al., 2015; Liu et. al., 2022). We hypothesized that bilateral inhibition of tagged BLA "engram" neurons expressing hM4Di during recall would disrupt astrocytic calcium dynamics that we observed in our first experiment. On Day 1, mice had Dox diet removed to 'open' the tagging window 48 hours later. On Day 3, mice underwent a 360 second contextual fear conditioning (CFC) session with the administration of 4, 1.5mA foot shocks, as described in our previous experiments while astrocytic calcium dynamics were recorded in BLA (Figure 7A; right). Immediately after this CFC session, mice were

placed back on their Dox diet to ‘close’ the tagging window (Figure 7A; right). On Day 4, mice underwent a 360 second contextual recall session in the absence of foot shocks. 30 minutes prior to this session, mice received intraperitoneal (IP) injection of clozapine-N-oxide (CNO) at 3 mg/kg to inhibit the ‘tagged’ fear neuronal ensemble during behavior (Figure 7A; right). Expression of hM4Di-mCherry in bilateral BLA with astrocytic GCaMP was confirmed in each animal prior to behavioral and calcium time series analysis (Figure 7B).

When comparing astrocytic calcium levels during CFC, both hM4Di and mCherry groups displayed robust increases at the initiation of each foot shock (120s, 180s, 240s, 300s), as previously described above (Figure 7C). This was expected, as no CNO was on board during the CFC session and we anticipated replication of our above findings. Additionally, in both groups there was time-locking to behavioral freezing initiation and termination epochs during CFC in both hM4Di and mCherry groups, further replicating our prior experiment (Freeze initiation and termination peri-event analysis; 99% CI)(Figure 7D-E). As expected, hM4Di and mCherry mice displayed the same freezing levels on average (Independent t-test; $p=0.2395$) and across time during CFC (Two-way ANOVA RM; Interaction: $F (5, 50) = 1.107$, $p=0.3688$; Time bin: $F (2.623, 26,23) = 82.43$, $p<0.0001$; Group: $F (1, 10) = 1.564$, $p=0.2395$; Subject: $F(10,50) =3.685$, $p=0.0010$)](Figure 7E). Finally, both groups displayed no significant differences in astrocyte calcium event characteristics (peak height, full-width half maximum, area under the curve, or frequency) during CFC, as expected ([Peak height: Independent t-test; Welch’s correction, $p=0.6532$][AUC: Independent t-test; Welch’s correction,

p=0.5351][FWHM: Independent t-test; p=0.7292][Frequency: Independent t-test; p=0.0623)(Figure 8G-J).

For fear memory recall, mice in the hM4Di and mCherry groups did not display detectable changes in astrocytic calcium dynamics (Figure 7K). This was further confirmed by peri-event analysis at the initiation and termination of freezing bouts during recall. As shown in our above experiments, astrocytic calcium becomes time-locked to each of these behavioral epochs for both hM4Di and mCherry groups compared to their respective medians (Freezing initiation/termination: peri-event analysis, 99% CI)(Figure 7L-M). This suggests that CNO does not have an effect on astrocytic calcium dynamics during contextual recall. Interestingly, we did not observe any significant differences in behavioral freezing levels between the two groups, suggesting that chemogenetic inhibition of a fear engram in the BLA does not lead to a decrease in freezing levels (Independent t-test; p=0.2028), nor the recall of fear across time within session (Mixed-effects model (REML); Interaction: F (5,60) = 0.7030, p=0.6234; Time bin: F(1,60) = 5.257, p=0.0254; Group: F(5,60) = 0.6997, p=0.6258)(Figure 7N).

Furthermore, to quantify any differences in astrocytic calcium event metrics, peak height, FWHM, AUC and frequency (Hz) were analyzed. There were no significant differences in any of these metrics, with both groups mirroring the results described in our initial shock group findings ([Peak height: Independent t-test; p=0.3921][AUC: Independent t-test; p=0.5271][FWHM: Independent t-test; p=0.6981][Frequency: Independent t-test; p=0.6860])(Figure 7O-R). Overall, our data suggests that inhibition of a neuronal fear engram in BLA does not impact behavioral freezing levels, nor does it

impact astrocytic calcium dynamics. It is important to note, however, that the freezing behavior and its tie to astrocytic calcium was maintained.

To address the possibility that reduced dF/F (%) we see was a function of non-experience related effects (i.e. photobleaching caused by repeated recordings), we assessed the peak dF/F (%) across days. We found that there were no significant changes in the no-shock group across days and only the fear conditioning session was significantly different from other days in the shock group (Two-way ANOVA; Interaction: $F(5, 74) = 4.924$, $p=0.0006$; Day: $F(5, 74) = 4.769$, $p=0.0008$; Group: $F(1,74) = 19.72$, $p<0.0001$)(Tukey's multiple comparisons: Shock [FC vs. Recall, $p<0.0001$; FC vs. EXT1, $p<0.0001$; FC vs. EXT2, $p<0.0001$; FC vs. EXT3, $p<0.0001$; FC vs. Cxt B, $p<0.0001$], all other comparisons across days for the Shock and No Shock groups were not significant)(Figure 8A). This is an unsurprising result, as a negative experience like shock could easily cause such robust differences for which we observed (Figure 2A). From this analysis we can conclude that after fear conditioning the peak dF/F did not change in the shock group and such alterations in event metrics were not caused by photobleaching or other technical considerations.

**2.4) Discussion**

Our results demonstrate that BLA astrocytes are differentially involved in the acquisition, recall, and extinction of a contextual fear memory. Strikingly, these astrocyte populations in the no-shock groups showed low levels of calcium dependent activity relative to the shocked group. These results corroborate previous research demonstrating that astrocytic populations are active specifically during salient experiences (Adamsky et.

al., 2018). Furthermore, this could be related to an increased demand for neuronal metabolic support due to cellular activity recruited during memory formation. Recent models suggest that astrocytes become active during metabolically taxing experiences to support memory encoding and consolidation by providing astrocytically derived lactate to neuronal populations to increase ATP production (Steinman et. al., 2016; Adamsky & Goshen, 2018; Alberini et al. 2018). In line with this possibility, in our study mice that did not associate a noxious stimulus to the context displayed less activity than the shocked group. This could indicate that during memory acquisition, where a CS is paired with a US, astrocytic populations become involved to maintain this memory association. As the BLA preferentially parses salient information (Sengupta et. al., 2018; Pryce et. al., 2018), this could explain the lack of strong calcium events in the no-shock group, whereas in a structure that processes both associations and emotional salience (Zheng et. al., 2017; Eichenbaum, Schoenbaum, Young & Bunsey, 1996), such as the HPC, we predict to see reliable but increased events during contextual exploration and after CS-US pairing. Relatedly, and given that astrocyte assemblies are remarkably disengaged before the onset of foot shock during CFC in our study, future experiments may test whether populations of astrocytes are necessary for proper fear expression, and if after such salient experiences, BLA neurons require glial participation for stable memory correlates.

Interestingly, we only observed differences in the calcium event characteristics (e.g. FWHM, peak height) in the shock group when animals are undergoing CFC. This could indicate there are two distinct populations of cells, one which becomes active for memory encoding and maintenance, whereas the other is there to process incoming sensory input

into the BLA or motor output. This hypothesis is supported by our modeling approach which reported significant contribution of kinematic related information as well as stimuli specific and relevant behavioral information. Furthermore, while the no-shock animals display minimal calcium transients these transients are significantly wider, possibly in response to exploring the novel context. This could be explained by the observation that AUC for these transients was also significantly lower for these animals, suggesting there was less overall calcium binding and subsequent recorded fluorescence, and thus indicating there may be cells that had sustained activity in response to non-discrete stimuli, in contrast to something well defined like foot-shock. Furthermore, peri-events were observed in the fear conditioning and recall sessions. Specifically, we observe an increase in activity prior to the initiation and termination of freezing during fear conditioning. During recall, the calcium response shifts, with the peak occurring simultaneously with the initiation of freezing. Further, during recall we see a shift to the calcium peak occurring after the termination of freezing. It is possible that astrocytes ramp up their activity to either induce a state of freezing or become active in response to increased neuronal activation immediately prior to bouts of freezing. Regarding the termination of a freezing bout specifically, it is possible that astrocytes play a functional role in suppressing fear or anxiety states within the BLA (Cho et. al., 2022), though it is important to note that separate studies have also implicated their role in modulating locomotion (Qin et. al., 2020)--thus, as termination of freezing by definition requires movement, these two explanations remain to be reconciled. Notably, we did not observe these elevations in calcium activity at the initiation or termination of freezing during extinction. Indeed, we lose our predictive power

in our GLM during extinction sessions, further evidencing this putative decoupling, and so it is likely these signals reflect internal physiological states that would be interesting to further investigate with higher spatial resolution. This could be due to the difference in session length causing changes to how these cells respond after the initial six-minutes, or it could be that after this initial exposure some subsequent learning has occurred causing these cells to respond to different local cues or internal states. While fiber photometry renders this possibility difficulty to test due to the lack of cell-specific granularity it affords, these hypotheses would be interesting to explore with higher resolution *in vivo* one-photon imaging approaches as it would allow us to visualize multiple subpopulations of BLA astrocytes, which could explain the diverse milieu of these signals.

Importantly, our findings that astrocytic calcium dynamics are modulated by salient stimuli were specific to the fear conditioned context, as supported by the lack of astrocytic calcium and behavioral changes in the neutral open field context. This is in line with previous findings showing that astrocytic manipulation enhances memory allocation in a task-specific manner during learning, but not in the home cage (Adamsky et. al., 2018). Astrocytic activity is heavily dependent on the presence of salient stimuli during a learning experience (i.e. foot shock) and that novel exploration of an environment is not sufficient to induce changes in the underlying calcium dynamics of astrocytes. This is congruent with data suggesting that the BLA shows sparse activity that is dependent on salient stimuli (i.e. reward) (Pratt & Mizumori, 1998).

Our findings suggest that chemogenetic-mediated neuronal engram inhibition in the BLA during recall does not abolish freezing behavior, nor affect astrocytic calcium

dynamics. While other work in the field suggests that BLA engram cells are necessary for fear recall (Han et. al., 2009), we speculate that both the behavioral schedules and inhibitory strategies implemented constrain whether or not a BLA-mediated engram becomes necessary for the behavioral expression of memory. Specifically, previous work directly inhibiting BLA engram cells using the inhibitory opsin, ArchT, shows a decrease in behavioral freezing during recall, in a light-dependent manner (Zaki & Mau et al., 2022). However, this work performed inhibition after the extinction, reinstatement, and recall of this reinstated memory. Thus, the differences in behavioral schedules and phases of learning during which inhibition occurs can influence whether or not engrams are necessary for the behavioral output of fear during recall. Another technical consideration is that we are using chemogenetics whereas this previous work utilized an inhibitory opsin. It is possible that the temporal specificity of the light-driven method was able to inhibit these engram cells more effectively in a behaviorally-relevant manner. Additionally, inhibition of a neuronal ensemble overexpressing CREB protein in the BLA resulted in decreased freezing behavior during recall (Han et al., 2009; Rashid et. al., 2016). Notably, this finding was in the context of auditory tone conditioning as opposed to contextual fear conditioning in our experiments, which have separate circuits that could explain these differential effects. We believe these differences point to boundary conditions under which BLA-mediated engrams are revealed to be necessary for memory.

Future work may seek to express a pan-neuronal inhibitor throughout the BLA to test if this global reduction in activity modulates astrocyte dynamics. It is possible that the number of engram cells tagged in the BLA is not sufficient to abolish the behavioral

expression of fear, or other brain regions may be compensating for or driving this behavior in coordination with the BLA. Astrocytes may still be intimately associated with engram cells in the BLA, but this perturbation is not sufficient to eliminate their activity. It would be interesting to label BLA engram cells and their associated astrocytes with chemogenetic tools to observe if the combination of cell inhibition (and thus, expanding the definition of an 'engram' to include glial cells) abolishes memory recall. Promisingly, such strategies that permit labeling and manipulation of both neurons and astrocytes will enable a better understanding of how heterogeneous cell types contribute to the overall memory engram as well as its behavioral expression. Broadly, since we are recording calcium dynamics from astrocytes in these experiments, it may be possible that neuronal calcium is being modified by hM4Di inhibition and our approach is unable to capture these changes. However, even if neuronal activity was decreased, astrocytes could be 'compensating' for the behavioral output of fear during recall. A general assumption of this mechanism is that neurons and astrocytes are correlated in their calcium activity (Zhao et. al., 2012; Agulhon et. al., 2008).

While our results demonstrate a functional role of astrocytes in fear learning, the BLA is known to process additional salient information including fear, reward, novelty, etc. For instance, recent studies have shown that there are heterogeneous, genetically defined, populations within the BLA which may preferentially respond to a variety of stimuli and valences (Kim et. al., 2016). While our experiments did not tease out any valence-specific contributions of astrocytic calcium activity, future studies may deliver multiple valence-specific stimuli (e.g. sweetened condensed milk, social interaction,

restraint stress) to animals while recording the corresponding calcium transients in the BLA. We posit that the BLA will display robust calcium dynamics to both positive and negative stimuli, albeit in partially separate populations of cells. This is consistent with recent literature showing that there are genetically-defined populations of cells along the anterior-posterior axis of the BLA that process fear and reward uniquely (Kim et. al., 2016).

While this work provides a role for astrocytes in conditioned fear, an ongoing issue surrounds whether astrocytes are mere support cells for neurons or if they actively encode information necessary for cognitive processes. Future experiments may concurrently record from neuronal populations to identify putative relationships between each cell type, and how real-time interplay between these populations supports learning and memory processes. A tantalizing possibility that combines neuron-glia relationships with neuromodulatory influences is that BLA astrocytes are necessary for proper adrenergic signaling which has been proposed in prior work (Gao et. al., 2016; Akther & Hirase, 2021). Also, it has been shown that CFC induces a downregulation of astrocytic Rac1 (Liao et. al., 2017; Fan et. al., 2021), promoting astrocytic plasticity, which may explain our observed differences in calcium events between our two groups in that this increased astrocytic plasticity could be necessary for remodeling synaptic connections for continued signaling. Further, astrocytes have been shown to contribute to remote memory formation via projection-specific modulation of hippocampal-cortical targets (Kol et. al., 2020). It would be interesting to explore astrocytic contributions to natural forgetting of a fear memory, rather than extinction, on a longer time scale. This could be performed with

longitudinal calcium recordings throughout a fear memory paradigm, with the addition of tracking throughout the decrease in freezing behavior that occurs over weeks.

Finally, future studies may causally dissect the role of astrocytes by Gq or Gi pathway activation in these populations during recall or extinction to determine if cellular manipulation is capable of inducing either a memory enhancing or amnesic response to fear learning. As astrocytes do not have typical "inhibition/excitation" properties which are more typically associated with neurons (Durkee et. al., 2019; Van Den Herrewegan et. al., 2021), future research may take its amore complex signaling pathways into account and yield crucial information in how astrocytes participate at the tripartite synapse to facilitate the learning of conditioned fear. Indeed, higher resolution single-cell and populating imaging methods, combined with causal perturbation strategies, could be used to further delineate the role of these cells in memory formation and expression. Overall, our results suggest an active role of astrocytes in contextual fear learning within the BLA and reveal their dissociable role in contributing to memory recall and extinction.

**2.5) Acknowledgements**

This work is supported by the NIH Early Independence Award DP5 OD023106-01, NIH Transformative Award, Brain and Behavior Research Foundation Young Investigator Grant, McKnight Foundation Memory and Cognitive Disorders Award, Pew Scholars Program in the Biomedical Sciences, Air Force Office of Scientific Research Grant FA9550-21-1-0310, and Center for Systems Neuroscience and Neurophotonics Center at Boston University

## 2.6) Author Contributions

R.L.S. and R.A.S contributed equally to this work. R.L.S., R.A.S., M.D.B., R.H.C., and S.R. designed research; R.L.S., R.A.S., M.D.B., A.Y.P., K.E.D., A.H.D., and R.H.C. performed research; R.L.S, R.A.S., M.D.B., A.Y.P., and S.R. analyzed data; R.L.S., R.A.S., and S.R. wrote the paper. This work is supported

## 2.7) Declaration of Competing Interests

The authors declare no competing financial interests.

## 2.8) Data Availability Statement

The data that support the findings of this study are available from the corresponding author upon reasonable request. All statistical analysis and subsequent photometry analysis was performed via custom python scripts freely available at https://github.com/rsenne/RamiPho.

## 2.9) Figures

### Figure 2.1

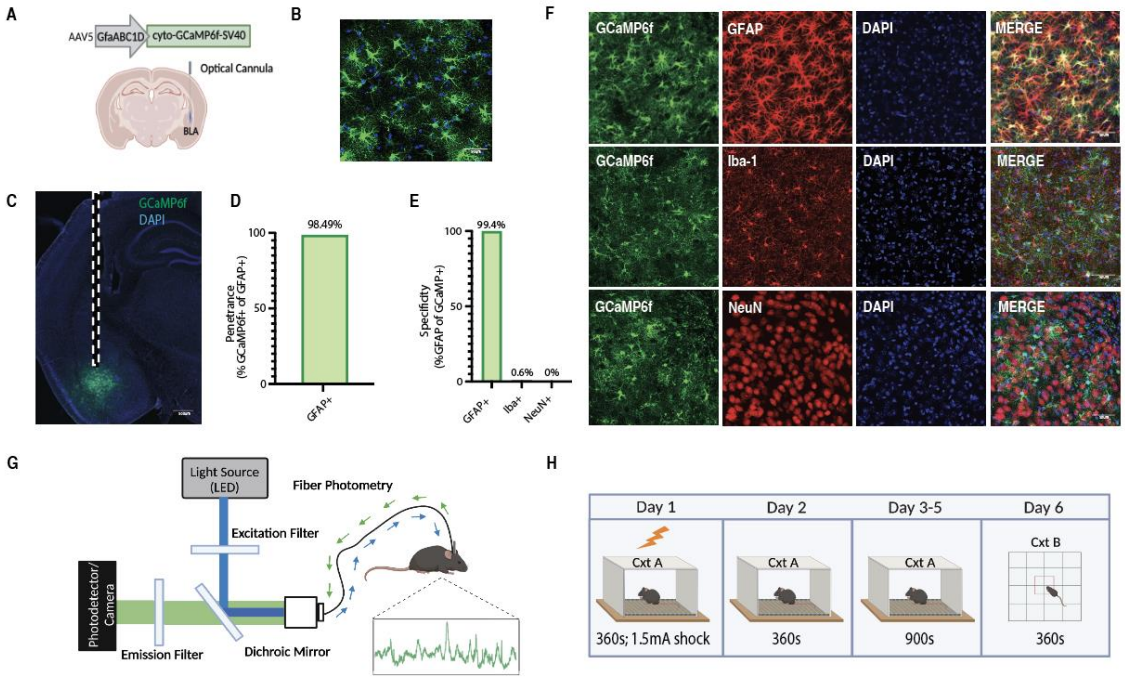


**Figure 2.1. Population-level calcium recordings of basolateral amygdala astrocytes across contextual fear conditioning, recall and extinction.** (A) Viral strategy and fiber implantation strategy for shock and no-shock conditions. The GECI AAV5-GfaABC1D-cyto-GCaMP6f-SV40 was unilaterally injected into the BLA region of wild-type mice**. (B-C)** Representative image of GFAPGCaMP6f1 (green) and DAPI1 (blue) cell expression within the BLA at 20 magnification (B) and 10 magnification (C). Scale bar, 500 mm. Dashed white lines indicate the approximate location of the unilateral fiber implantation. **(D)** Penetrance of GCaMP6f (2251 GCaMP6f1/2381 GFAP1 = 98.49%; n = 3; 4 slices/mouse). **(E)** Specificity of GCaMP6f (4 Iba-11/662 GCaMP6f1 = 0.604% microglia; 0 NeuN1/1064 GCaMP6f1 = 0.00% neurons; 2242 GFAP1/2256 GCaMP6f1 = 99.4% astrocyte; n = 3; 4 slices/mouse). **(F)** Representative expression of GCaMP6f expression

and overlap with microglial (Iba-1), astrocytic (GFAP), and neuronal (NeuN) markers. Scale bar, 50 mm. **(G)** In vivo fiber photometry setup. A 470 nM LED delivered an excitation wavelength to GCaMP6f-expressing astrocytes via a patch cord and single fiber optic implant in freely moving mice. The emitted 530 nM signal from the indicator was collected via the same patch cord and fiber, spectrally separated using a dichroic mirror, passed through a series of filters, and focused on a scientific camera. A representative calcium time series trace is shown for astrocytic calcium. Calcium-independent isosbestic signal was recorded simultaneously to account for motion, tissue autofluorescence, and photobleaching across time. **(H)** Behavioral paradigm; mice underwent CFC on day 1 in Cxt A for 360 s where they received four 1.5 mA foot shocks. On day 2, mice were placed back into Cxt A for contextual recall for 360 s in the absence of foot shock. On days 3–5, mice underwent three contextual extinction sessions for 900 s each. On day 6, mice were placed in Cxt B for 360 s. Mice were perfused and brains extracted for histologic assessment.

**Figure 2.2**

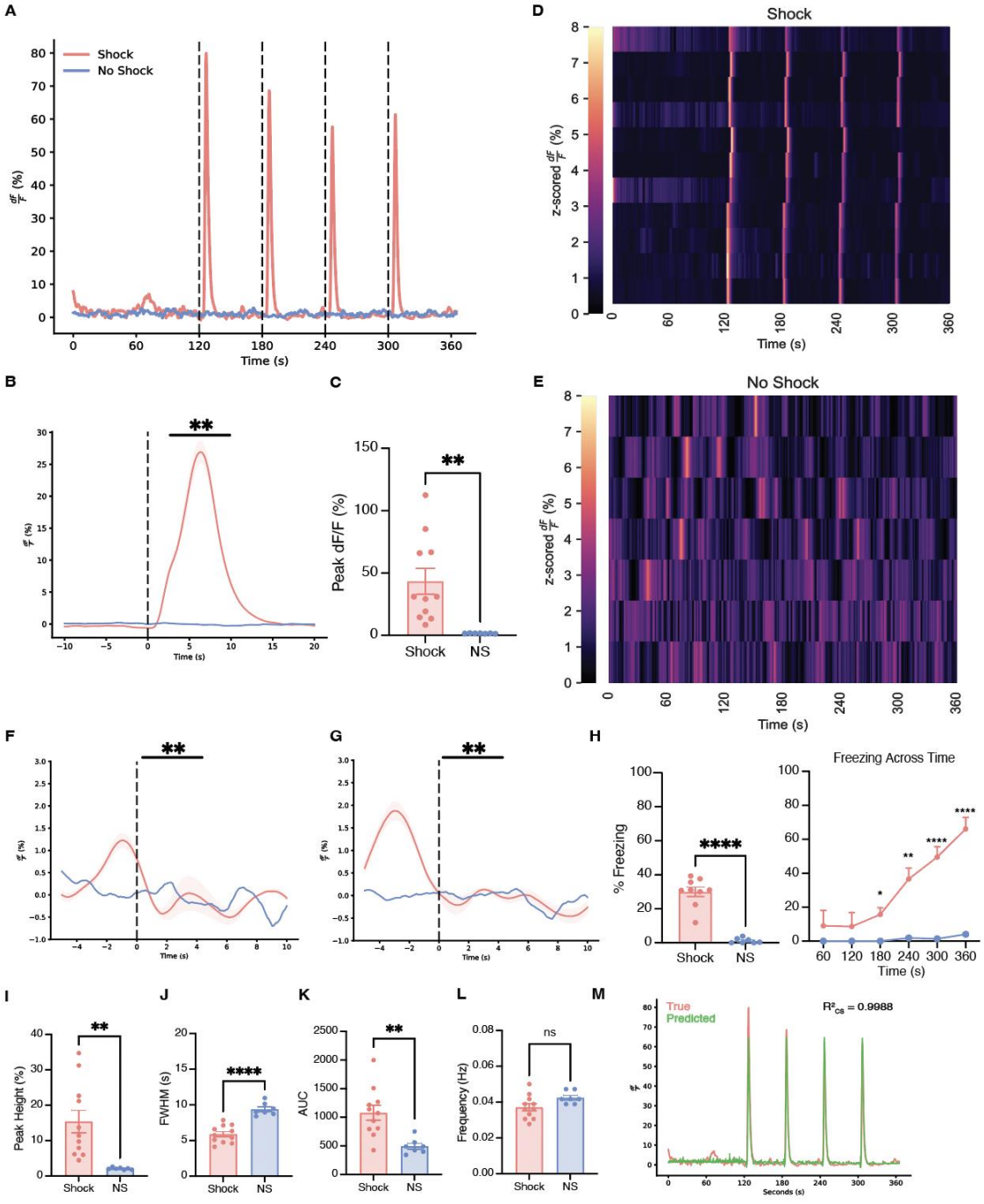
A
Shock
No Shock
Time (s)
B
C
Peak dF/F (%)
Shock
NS
D
Shock
z-scored dF/F (%)
Time (s)
E
No Shock
F
G
H
% Freezing
Freezing Across Time
I
Peak Height (%)
J
FWHM (s)
K
AUC
L
Frequency (Hz)
ns
M
True
Predicted
Seconds (s)

**Figure 2.2: Basolateral amygdala astrocytes robustly respond to foot shock during contextual fear conditioning and exhibit unique calcium event dynamics compared to no-shock controls. (A)** Representative calcium time series (dF/F percentage) for shock and no-shock conditions during the 360 s CFC session; 1.5 mA foot shocks occurred at the 120, 180, 240 and 300 s time points, as indicated by vertical dashed lines. **(B)** Peri-event analysis for 1.5 mA foot shock, with the onset of foot shock occurring at the dashed line (time = 0). **(C)** Quantification of the average percentage change in peak dF/F at the onset of foot shock. **(D-E)** The z-scored dF/F (percentage) across CFC for shock (D) and no-shock conditions (E); each row represents a single subject across time within the session. **(F-G)** Peri-event analysis for the initiation (F) and termination (G) of freezing behavior, with each event occurring at the dashed line (time = 0). **(H)** Average percentage freezing (left) and freezing across time within the CFC session (right). **(I–L)** Calcium event metrics; peak height (I), full-width half-maximum (J), area under the curve (K), and frequency (L). **(M)** True (pink) and predicted (green) calcium time series produced from a generalized linear model. All error bars and bands indicate standard error of the mean (SEM). For t tests and ANOVAs, *p <0.05, **p<0.01, ***p<0.001, ****p<0.0001; ns, not significant. For peri-event metrics, *95% CI, **99% CI; ns. For t tests and ANOVAs, shock n = 11, no shock n = 7. For foot shock peri-events, shock n = 11, no shock n = 7. For freezing peri-events, shock n = 11, no shock n = 2 because of mice not freezing during this session.

**Figure 2.3**

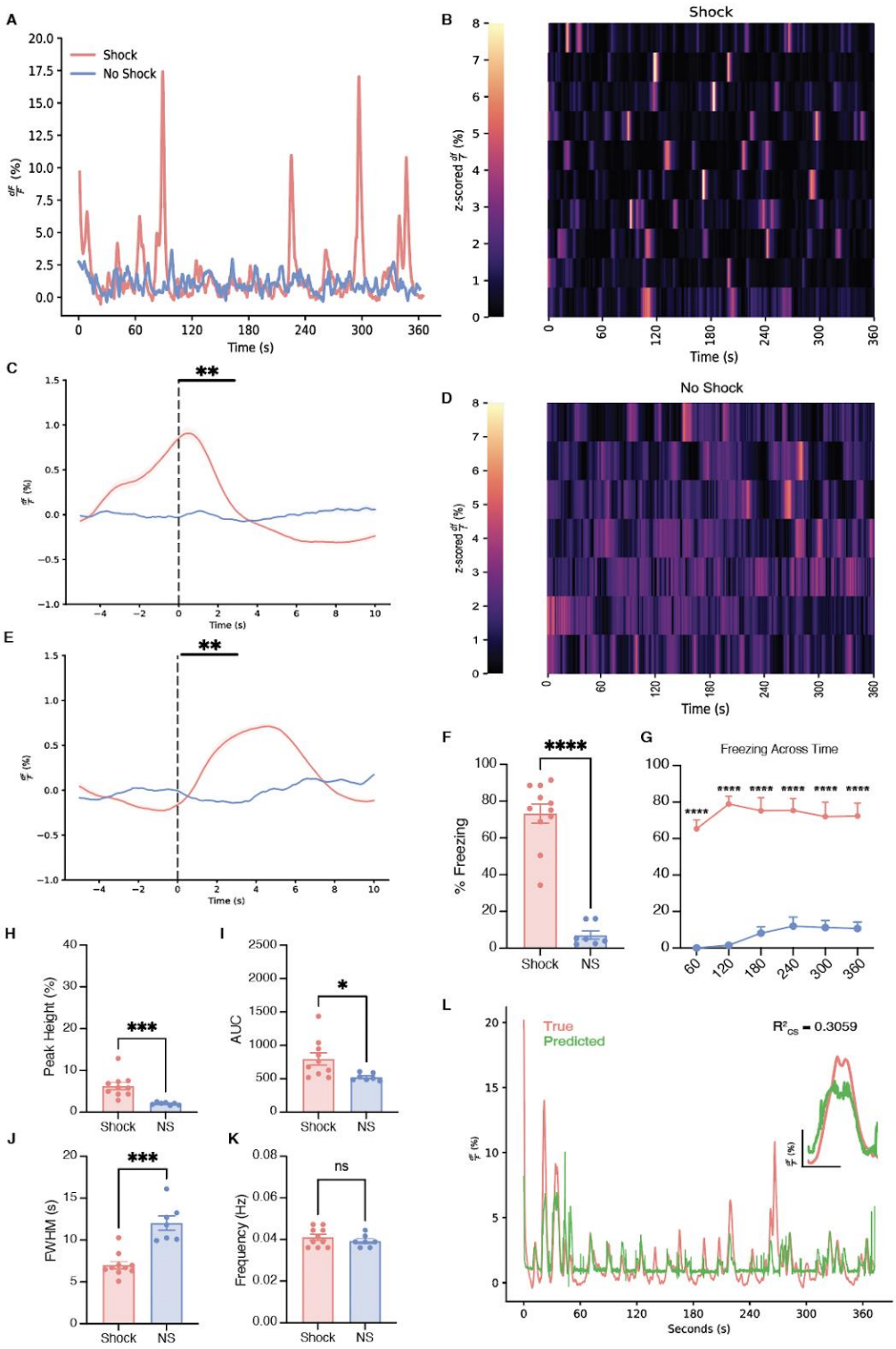
A
Shock
No Shock
Time (s)
B
Shock
z-scored
Time (s)
C
**
Time (s)
D
No Shock
z-scored
Time (s)
E
**
Time (s)
F
****
% Freezing
Shock
NS
G
Freezing Across Time
H
***
Peak Height (%)
Shock
NS
I
*
AUC
Shock
NS
J
***
FWHM (s)
Shock
NS
K
ns
Frequency (Hz)
Shock
NS
L
True
Predicted
$R^2_{cs}$ = 0.3059
Seconds (s)

**Figure 2.3: BLA astrocytes respond reliably to the initiation and termination of freezing behavior during contextual recall. (A)** Representative calcium time series (dF/F percentage) for shock and no-shock conditions during the 360 s recall session in the absence of foot shock. **(B, D)** z-scored dF/F (percentage) across recall for (B) shock and (D) no-shock conditions; each row represents a single subject across time within the session. **(C, E)** Peri-event analysis for the initiation (C) and termination (E) of freezing behavior, with each event occurring at the dashed line (time = 0). **(F-G)** Behavioral analysis; average percentage freezing (F) and freezing across time within the recall session (G). **(H-K)** Calcium event metrics; peak height (H), area under the curve (I), fullwidth half-maximum (J), and frequency (K). **(L)** True and predicted calcium time series produced from a generalized linear model. Error bars indicate SEM. For t tests and ANOVAs, *p<0.05, **p<0.01, ***p<0.001, ****p<0.0001; ns, not significant. For peri-event metrics, *95% CI, **99% CI; ns. For t tests and ANOVAs, shock n = 11, no shock n = 7. For freezing peri-events, shock n = 11, no shock n = 6 because of a mouse not freezing during the recall session.

**Figure 2.4**

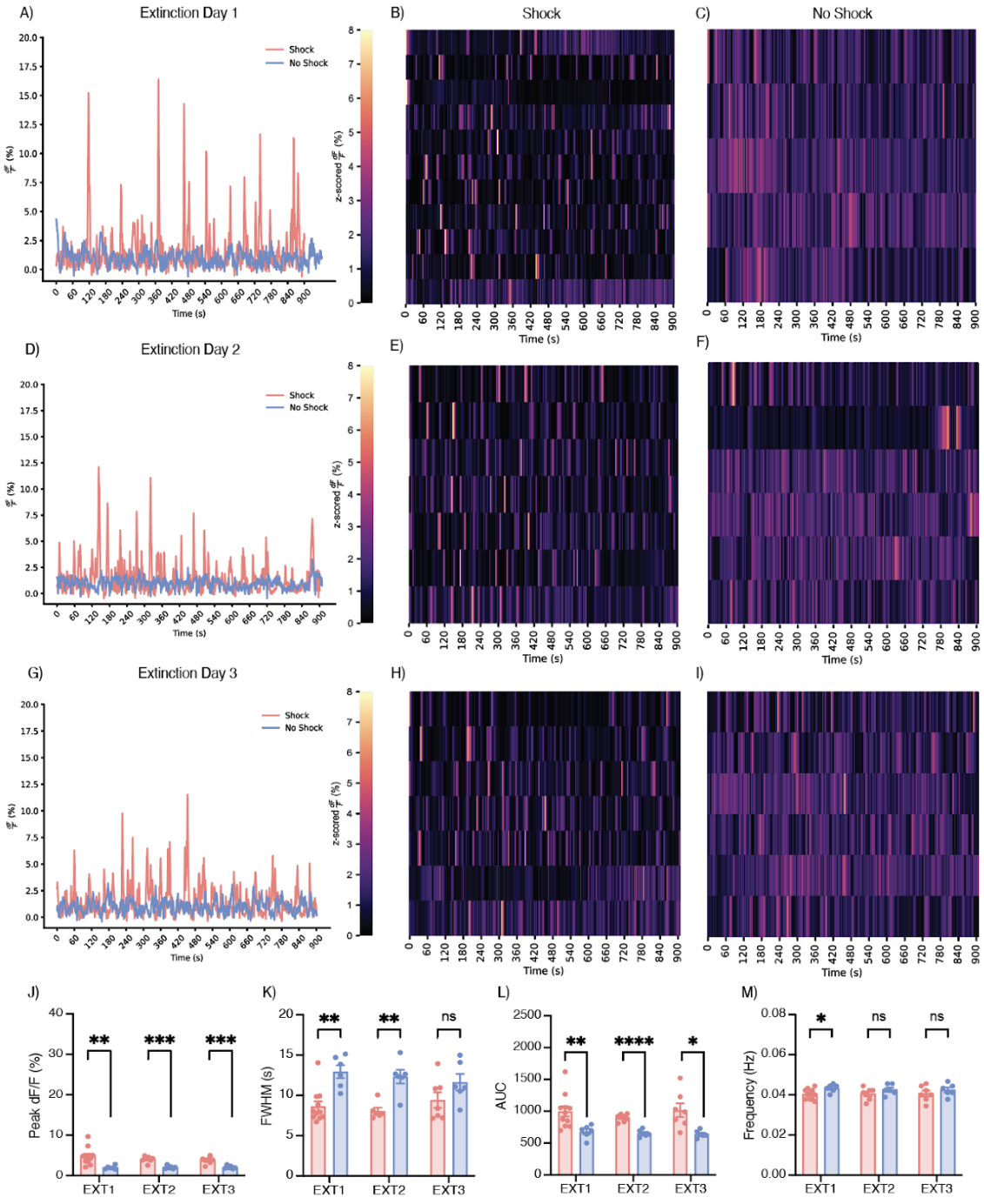
A)
Extinction Day 1
Shock
No Shock
dF/F (%)
Time (s)
z-scored dF/F (%)
B)
Shock
C)
No Shock
D)
Extinction Day 2
E)
F)
G)
Extinction Day 3
H)
I)
J)
Peak dF/F (%)
EXT1
EXT2
EXT3
K)
FWHM (s)
L)
AUC
M)
Frequency (Hz)
ns

**Figure 2.4: BLA astrocytes in the shock condition exhibit increased peak height, decreased duration, and increased total fluorescence of events compared to no-shock, but these do not change across extinction days. (A, D, G)** Representative calcium time series (dF/F percentage) for shock and no-shock conditions during the 900 s contextual extinction sessions; extinction day 1 (EXT1) (A), extinction day 2 (EXT2) (D), extinction day 3 (EXT3) (G). **(B, E, H)** z-scored dF/F (percentage) across extinction for shock condition; each row represents a single subject across time within the session. **(C, F, I)** z-scored dF/F (percentage) across extinction for the no-shock condition; each row represents a single subject across time within the session. **(J–M)** Calcium event metrics; peak height (J), full-width half-maximum (K), area under the curve (L), and frequency across all three d of extinction (M). Error bars indicate SEM. For t tests, *$p<0.05$, **$p<0.01$, ***$p<0.001$, ****$p<0.0001$; ns, not significant. Extinction 1, shock n = 11, no shock n = 6 (For the no-shock group, recording for one animal was 90 s short. This animal was excluded from the raster plot and behavioral analysis but still used for event metric calculations). Extinction 2, shock n = 7, no shock n = 6. Extinction 3, shock n = 7, no shock n = 6.

**Figure 2.5**

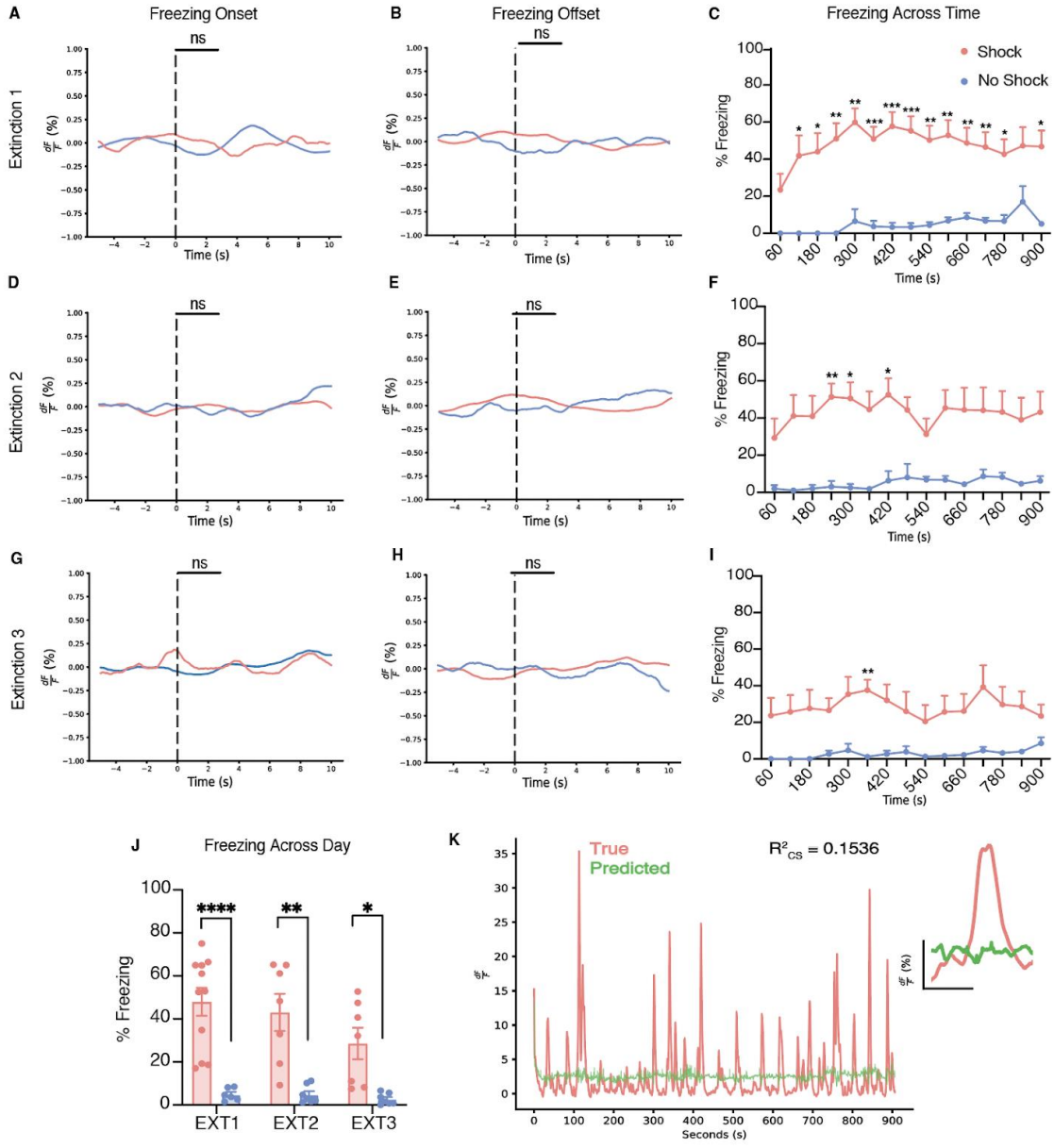
A
Freezing Onset
B
Freezing Offset
C
Freezing Across Time
Extinction 1
Extinction 2
Extinction 3
ns
Time (s)
Shock
No Shock
% Freezing
D
E
F
G
H
I
J
Freezing Across Day
EXT1
EXT2
EXT3
K
True
Predicted
$R^2_{CS}$ = 0.1536
Seconds (s)

**Figure 2.5: BLA astrocytic calcium does not respond to the initiation or termination of freezing behavior during extinction sessions. (A–B)** Peri-event analysis for the initiation (A) and termination (B) of freezing behavior, with each event occurring at the dashed line (time = 0) for extinction day 1. **(D-E)** Peri-event analysis for the initiation (D) and termination (E) of freezing behavior, with each event occurring at the dashed line (time = 0) for extinction day 2. **(G-H)** Peri-event analysis for the initiation (G) and termination (H) of freezing behavior, with each event occurring at the dashed line (time = 0) for extinction day 3. Percentage freezing across time within extinction day 1 **(C)**, extinction day 2 **(F)**, and extinction day 3 **(I)**. **(J)** Average percentage freezing across 3 d of extinction for shock and no-shock conditions. **(K)** True and predicted calcium time series produced from a generalized linear model. Error bars indicate SEM. For t tests and ANOVAs, *p<0.05, **p<0.01, ***p<0.001, ****p<0.0001; ns, not significant. For peri-event metrics, *95% CI, **99% CI; ***99.9; ns. Extinction 1, shock n = 11, no shock n = 6. (For the no-shock group, the recording for one animal was 90 s short. This animal was excluded from the raster plot and behavioral analysis but still used for event metric calculations). Extinction 2, shock n = 7, no shock = 6. Extinction 3, shock n = 7, no shock n = 6.

**Figure 2.6**

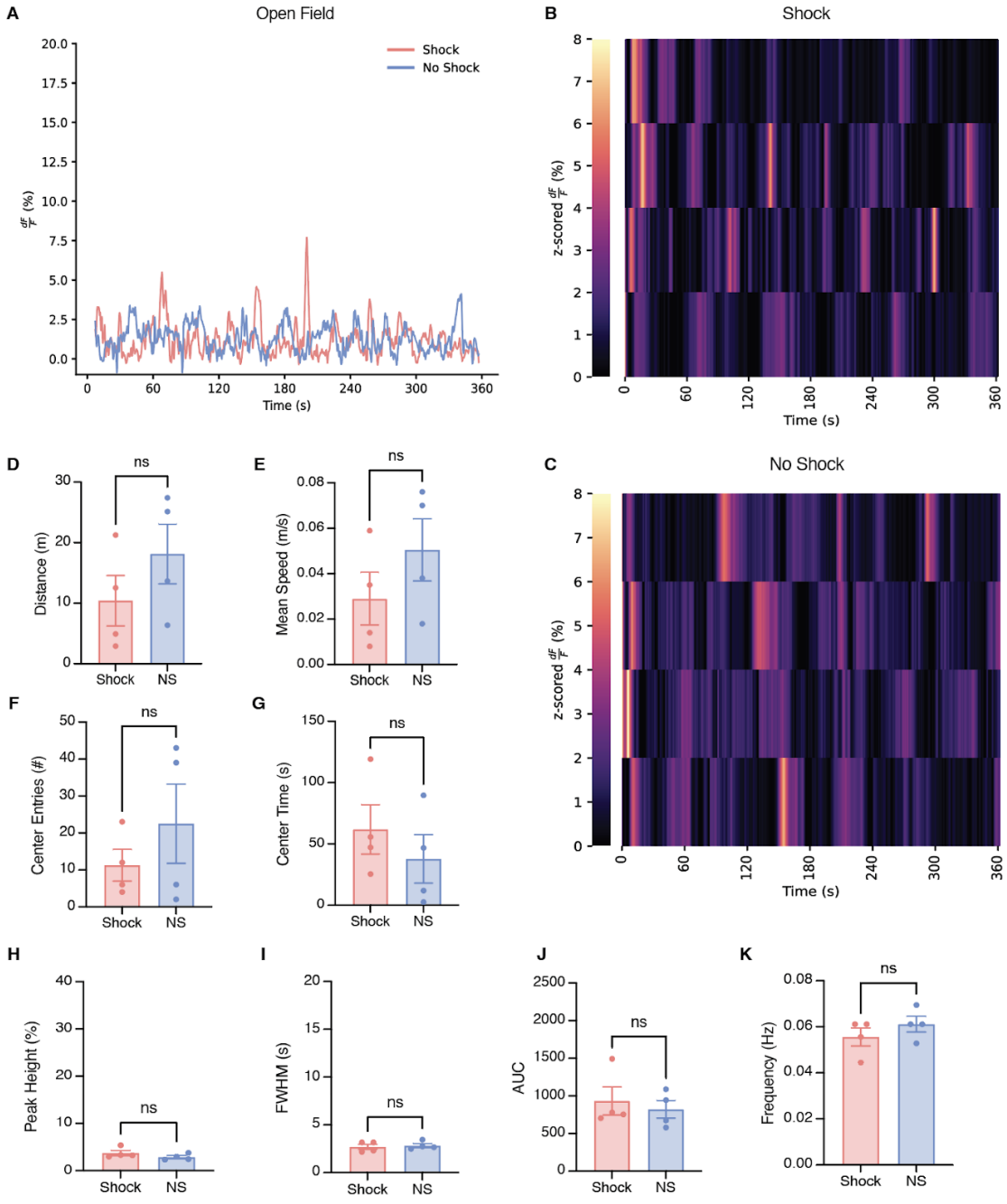
A
Open Field
Shock
No Shock
Time (s)
B
Shock
z-scored dF/F (%)
Time (s)
C
No Shock
z-scored dF/F (%)
Time (s)
D
Distance (m)
ns
Shock
NS
E
Mean Speed (m/s)
ns
Shock
NS
F
Center Entries (#)
ns
Shock
NS
G
Center Time (s)
ns
Shock
NS
H
Peak Height (%)
ns
Shock
NS
I
FWHM (s)
ns
Shock
NS
J
AUC
ns
Shock
NS
K
Frequency (Hz)
ns
Shock
NS

**Figure 2.6: Astrocytic calcium event characteristics and behavior in a novel open field environment do not differ between shock and no-shock groups. (A)** Representative calcium time series (dF/F percentage) for shock (coral) and no-shock (blue) conditions during the 360 s novel open field Cxt B session. **(B-C)** z-scored dF/F (percentage) in Cxt B for shock and no-shock conditions; each row represents a single subject across time within the session. **(D–G)** Behavioral measures; distance traveled (meters; D), mean speed (m/s; E), number of center entries (# entries; F), and time spent in the center (seconds; G). **(H–K)** Calcium event metrics; peak height (%; H), full-width half-maximum (seconds; I), AUC (J), and frequency (Hz; K). Error bars indicate SEM. For t tests, *p<0.05, **p<0.01, ***p<0.001, ****p<0.0001; ns, not significant. Open field Cxt B, shock n = 4, no shock n = 4.

**Figure 2.7**

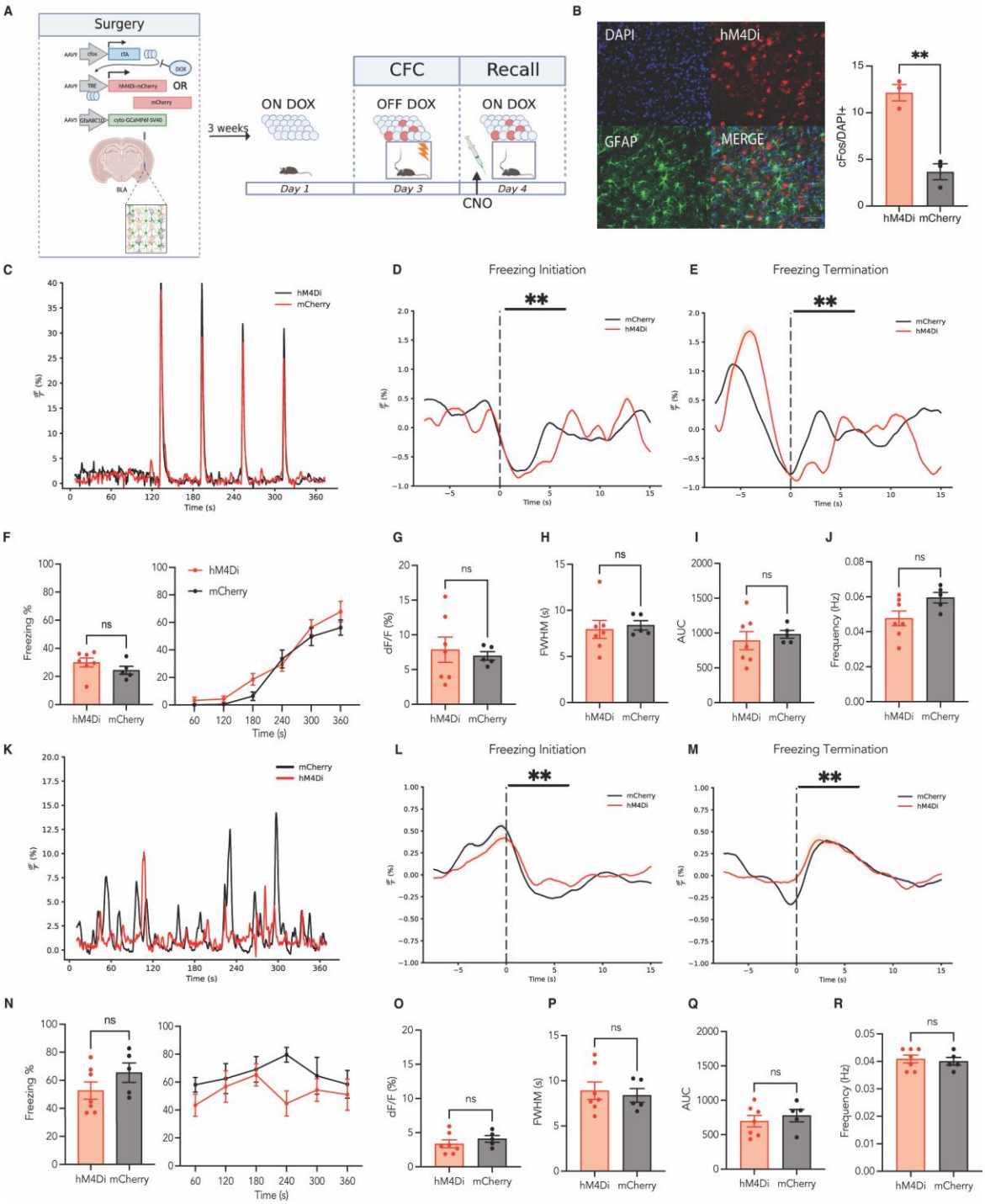
A
Surgery
OR
3 weeks
ON DOX
OFF DOX
ON DOX
CFC
Recall
Day 1
Day 3
Day 4
CNO
B
DAPI
hM4Di
GFAP
MERGE
cFos/DAPI+
hM4Di mCherry
C
hM4Di
mCherry
Time (s)
D
Freezing Initiation
E
Freezing Termination
F
Freezing %
ns
G
dF/F (%)
H
FWHM (s)
I
AUC
J
Frequency (Hz)
K
L
Freezing Initiation
M
Freezing Termination
N
O
P
Q
R

**Figure 2.7: Neuronal fear engram inhibition in the BLA during recall does not modify freezing behavior or astrocytic calcium event characteristics. (A)** Surgical and behavioral schematic. The genetically encoded calcium indicator, AAV5-GfaABC1D-cyto-GCaMP6f-SV40, was unilaterally injected into the BLA in combination with bilateral injection of either AAV9-c-fos-tTA-TRE-hM4DimCherry (hM4Di) or AAV9-c-fos-tTA-TRE-mCherry (mCherry) control virus to allow chemogenetic control of labeled cells while recording astrocytic calcium dynamics. On Day 1, mice were taken off of their Dox diet to allow for the opening of the labeling window 48 h in advance of behavioral testing. On Day 3, mice underwent CFC on day 1 in Cxt A for 360 s where they received four 1.5 mA foot shocks. They were immediately placed back on their Dox diet, thus closing the labeling window. On Day 4, mice were placed back into Cxt A for contextual recall for 360 s in the absence of foot shock. Thirty minutes before this session, CNO was administered at 3 mg/kg to inhibit the labeled engram during recall. Ninety minutes after the start of the behavioral session, mice were perfused to capture peak endogenous cFos protein levels. **(B)** (Left) Representative images of hM4Di-mCherry/GFAP+ co-staining (red and green, respectively) and DAPI+ cells (blue). Scale bar indicates 50 mm. (Right) The percentage of cFos/DAPI counts in the hM4Di and mCherry groups. **(C)** Representative calcium time series (dF/F percentage) for hM4Di (red) and mCherry (black) conditions during the 360 s CFC session. **(D-E)** Peri-event analysis for the initiation (D) and termination (E) of freezing behavior during CFC, with each event occurring at the dashed line (time = 0). **(F)** Behavioral analysis for CFC. (Left) Average percentage freezing. (Right) Freezing across time within the recall session. (**G–J)** Calcium event

metrics for CFC, peak height (G), full-width half-maximum (H), area under the curve (I), and frequency (J). **(K)** Representative calcium time series (dF/F percentage) for hM4Di (red) and mCherry (black) conditions during the 360 s recall session. **(L-M)** Peri-event analysis for the initiation (L) and termination (M) of freezing behavior during recall, with each event occurring at the dashed line (time = 0). **(N)** Behavioral analysis for recall. (Left) Average percentage freezing. (Right) Freezing across time within the recall session. **(O–R)** Calcium event metrics for recall, peak height (O), full-width half-maximum (P), area under the curve (Q), and frequency (R). All error bars and bands indicate SEM. For t-tests and ANOVAs, *p<0.05, **p<0.01, ***p<0.001, ****p<0.0001; ns, not significant. For peri-event metrics, *95% CI, **99% CI; ns; hM4Di = 7, mCherry = 5.

**Figure 2.8**

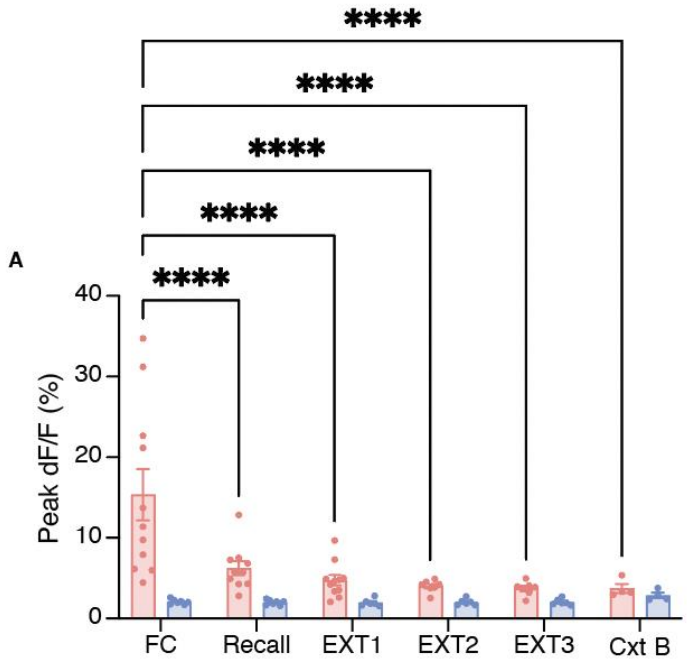


**Figure 2.8: Astrocytic calcium dF/F does not change after contextual fear conditioning. dF/F (percentage) across FC, recall, extinction (EXT1–3), and exposure to the novel open field context (Cxt B).** All error bars and bands indicate SEM. For ANOVA, $p<0.05$, $^{**}p<0.01$, $^{***}p<0.001$, $^{****}p<0.0001$; ns, not significant. Shock n = 4–11, no shock n = 4–7.

# CHAPTER THREE: ENGRAM REACTIVATION MIMICS CELLULAR SIGNATURES OF FEAR

Data and portions of the text in this chapter were originally published as:

Suthard, R. L., Senne, R. A., Buzharsky, M. D., Diep, A. H., Pyo, A. Y., & Ramirez, S. (2024). Engram reactivation mimics cellular signatures of fear. *Cell reports*, *43*(3), 113850. https://doi.org/10.1016/j.celrep.2024.113850

## Abstract

Engrams, or the physical substrate of memory, recruit heterogeneous cell types. Targeted reactivation of neurons processing discrete memories drives the behavioral expression of memory, though the underlying landscape of recruited cells and their real-time responses remain elusive. To understand how artificial stimulation of fear affects intra-hippocampal neuron-astrocyte dynamics as well as their behavioral consequences, we express channelrhodopsin-2 in an activity-dependent manner within dentate gyrus neurons while recording both cell types with fiber photometry in hippocampal ventral CA1 across learning and memory. Both cell types exhibit shock responsiveness, with astrocytic calcium events uniquely modulated by fear conditioning. Optogenetic stimulation of a hippocampus-mediated engram recapitulates coordinated calcium signatures time locked to freezing, mirroring those observed during natural fear memory recall. Our findings reveal cell-type-specific dynamics in the hippocampus during freezing behavior, emphasizing neuronal-astrocytic coupling as a shared mechanism enabling both natural and artificially induced memory retrieval and the behavioral expression of fear.

## 3.1) Introduction

The HPC is a region within the medial temporal lobe that is indispensable for episodic memory (Eichenbaum, 2000). In recent years, there has been an increasing focus on the ventral HPC's vital role in emotional processing and memory. Studies have confirmed differential roles along the dorsal and ventral axis, where the dorsal hippocampus (dHPC) is necessary for spatial and temporal encoding, while lesions to the ventral hippocampus (vHPC) cause emotional dysregulation and impaired stress responses (Fanselow & Dong, 2010; Ciocchi et al, 2015; Strange et al, 2014). More specifically, the vCA1 subregion contains a subset of basolateral amygdala-projecting neurons necessary for contextual fear conditioning (CFC) and are responsive to the aversive conditioning (Ciocchi et al, 2015). This body of work suggests a critical role for vCA1 in aversive conditioning and the subsequent emotional responses.

The HPC's subregions and cell types have a complex and heterogeneous structure-function relationship. The dentate gyrus (DG), CA3, and CA1 subregions of the HPC make up the "trisynaptic loop," which has shown to be a critical circuit for HPC mnemonic processes. Moreover, the dHPC, specifically the DG, contains defined sets of cells that undergo plasticity-related changes during learning which, when activated, are sufficient to drive the behavioral expression of memory (Liu & Ramirez et al, 2012; Ramirez et al, 2013; Ramirez et al, 2015; Denny et al, 2014; Redondo et al, 2014). These studies rely on inducible genetic tools, such as the Tet-tag system (Reijmers et al, 2007), to effectively 'tag' or label neuronal ensembles or *engrams* active during an initial experience which can later be reactivated via chemo- or optogenetics. This field of work has enhanced our

understanding of HPC computations and allows for a time-locked strategy for assessing a causal role between circuitry and behavior. However, most studies to date have focused almost exclusively on neuronal contributions to memory engrams, while the role of non-neuronal cell types within this HPC circuitry have remained relatively understudied. Thus, it is unknown whether these cells modulate intrahippocampal population dynamics in a pattern akin to natural memory recall.

Astrocytes are a predominant glial cell type that have been shown to play a pivotal role in the tripartite synapse, coupling with pre- and postsynaptic neurons to bidirectionally modulate synaptic communication (Araque et al, 1999; Perea, Navarette & Araque, 2009; Araque, Carmignoto & Haydon, 2001; Bezzi & Volterra, 2001; Haydon, 2001). These cells perform vital functions including maintaining the blood-brain barrier, supporting metabolic needs of surrounding neurons, releasing gliotransmitters and expressing neurotransmitter receptors to appropriately respond to and modulate their neuronal neighbors (Araque et al, 2014; Covelo & Araque, 2018; Porter & McCarthy, 1996). Recently, there has been a shift to studying astrocytes at the systems-level through the use of optogenetics, chemogenetics and optical imaging techniques (Corkrum et al, 2020; Lines et al, 2022; Qin et al, 2020; Tsunematsu et al, 2021; Ingiosi et al, 2020). For instance, manipulation of astrocytes in hippocampal and amygdalar sub-regions has been shown to impair or enhance both recent and remote memory formation and retrieval (Adamsky et al, 2018; Kol et al, 2020; Li et al, 2020; Martin-Fernandez et al, 2017). Moreover, recent engram studies have demonstrated the importance of non-neuronal cell types, microglia, and oligodendrocytes, in experience- and activity-dependent processes (Pan et al, 2020; Wang et al, 2020;

Steadman et al, 2020). Broadly, this burgeoning field suggests that glial cells are playing a role in modulating local and long-range projections within the brain to regulate behavior. Still, despite these recent advances little is known about how astrocytes may be playing a role in emotional processing within vCA1 during fear memory expression.

To that end, we combined activity-dependent tagging strategies with dual-color fiber photometry to study neuronal-astrocytic interplay of activity across fear encoding, natural recall, and artificial reactivation of a tagged engram. We injected a glial fibrillary acidic protein (GFAP)-driven GCaMP6f virus paired with a neuronal human synapsin (hSyn)-driven jRGECO1a in vCA1 to measure neuronal and astrocytic dynamics, while concurrently tagging and reactivating cells active during CFC in the dorsal DG (dDG) using Tet-tag viral constructs. We find that optogenetic reactivation of a fear memory is sufficient to induce cellular signatures that are akin to those seen during natural recall. These findings further enhance our understanding of the complex interplay of the cellular machinery of the brain and suggest that neurons and astrocytes are important members of the same processes.

## 3.2) Materials and Methods

### *3.2.1) Animals*

Wild type, male C57BL/6J mice (P29-35; weight 17-19g; Charles River Laboratories strain #027) were housed in groups of 3-5 mice per cage at the time of surgery. The animal facilities (vivarium and behavioral testing rooms) were maintained on a 12:12 hour light cycle (0700-1900). Mice received food and water *ad libitum* before and after

surgery. All mice were placed on a 40mg/kg doxycycline (Dox; Bio-Serv) diet 48 hours prior to surgery to inhibit any ‘tagging’ that could occur with the infusion of the Tet-tag viral cocktail. Following surgery, mice were group-housed with littermates and allowed to recover for 4 weeks before experimentation for expression of genetically-encoded calcium indicators (GECIs). All subjects were treated in accord with protocol 201800579 approved by the Institutional Animal Care and Use Committee (IACUC) at Boston University. As a limitation of this study, only male mice were utilized, and future work will investigate if these findings generalize to females as well. All n-values for each experimental group (Shock-ChR2, Shock-eYFP and Neutral-ChR2) can be found within the legends of each figure.

*3.2.2) Stereotaxic Surgery*

For all surgeries, mice were initially anesthetized with 3.0–3.5% isoflurane inhalation during induction and maintained at 1–2% isoflurane inhalation through stereotaxic (David Kopf Instruments) nose cone delivery (oxygen 1L/min). Ophthalmic ointment was applied to the eyes to provide adequate lubrication and prevent corneal desiccation. The hair on the scalp above the surgical site was removed using Nair hair removal cream and subsequently cleaned with alternating applications of betadine solution and 70% ethanol. 2.0% lidocaine hydrochloride (HCl) was injected subcutaneously as local analgesia prior to midsagittal incision of the scalp skin to expose the skull. 0.1 mg/kg (5 mg/kg) subcutaneous (SQ) dose of meloxicam was administered

at the beginning of surgery. All animals received craniotomies with a 0.5–0.6 mm drill-bit for ventral CA1 (vCA1) and dorsal dentate gyrus (dDG) injections and implants.

A 10μL airtight syringe (Hamilton Company) with an attached 33-gauge beveled needle was slowly lowered to the coordinates of hippocampal ventral CA1 (vCA1): −3.16 anteroposterior (AP), −3.10 mediolateral (ML) and −4.50 dorsoventral (DV) for fiber photometry recordings. All coordinates are given relative to bregma (mm). A volume of undiluted 250nL:500nL AAV5-GfaABC1D-cyto-GCaMP6f-SV40 (AddGene #52925)(Haustein et al, 2014) and AAV9-hSyn-NES-jRGECO1a-WPRE.SV40 (AddGene #100854)(Dana et al, 2016) was injected using a microinfusion pump for the vCA1 coordinate at 50 nL/min (UMP3; World Precision Instruments). After the injection was complete, the needle remained at the target site for 7–10 min post-injection before removal. Following viral injection, a unilateral optic fiber (200μm core diameter; 1.25mm ferrule diameter, NA = 0.37, length = 4.5mm; Neurophotometrics) was implanted at −4.60DV, slightly below the site of viral injection.

To enable engram tagging and manipulation via optogenetics, bilateral dorsal dentate gyrus (dDG) was infused with 1:1 undiluted AAV9-c-fos-tTA-BGHpa and AAV-TRE-ChR2-eYFP/AAV9-TRE-eYFP (UMass Vector Core, custom) to label neuronal ensembles with channelrhodopsin (ChR2), a blue-light sensitive protein. A volume of 250nL of the viral cocktail was infused at 100 nL/min into bilateral dDG at −2.20 AP, ± 1.30 ML and −2.0DV. Mice received bilateral optic fiber implants 0.2mm above the site of infusion (1.80 DV)(Doric Lenses). The implant was secured to the skull with a layer of adhesive cement (C&M Metabond) followed by multiple layers of dental cement

(Stoelting). Following surgery, mice were injected with a 0.1 mg/kg intraperitoneal (IP) dose of buprenorphine. They were placed in a recovery cage with a heating pad until fully recovered from anesthesia. Histological assessment verified viral targeting and data from off-target injections were not included in analyses.

*3.2.3) Tet-Tag System*

The Tet-tag system is an inducible, activity-dependent labeling strategy that relies on the neuronal expression of the immediate-early gene, cfos. This system is composed of a viral cocktail of c-fos-tTA and TRE-ChR2-eYFP or eYFP control fluorophore. This genetic strategy has been used to label (‘tag’) a neuronal ensemble, typically referred to as a memory engram, that contains information that is vital to the encoding and recall of a recent experience. This system couples the cfos promoter to the tetracycline transactivator (tTA). In its protein form, tTA directly binds to the tetracycline response element (TRE) in a doxycycline (Dox)-dependent manner and drives expression of a protein of interest (i.e., channelrhodopsin (ChR2) and/or fluorophore). This allows for the temporal regulation of a ‘tagging’ window when removed from an animal’s diet 48 h prior to a salient experience (i.e., contextual fear conditioning or home cage exposure). Returning the mice to Dox diet immediately after the experience of interest ‘closes’ the tagging window, and they remain untouched for 24 h to prevent off-target labeling. Most importantly, the expression of ChR2 allows for optogenetic reactivation of the experience tagged during encoding. Specifically, optogenetic stimulation of ChR2+ negative engram cells with blue light in a ‘neutral’ context manifests as a freezing response, typically referred to as light-induced freezing.

*3.2.4) Fiber Photometry Data Collection*

A 470-nm LED (Neurophotometrics; FP3002) delivered an excitation wavelength of light to astrocytes expressing GCaMP6f via a single fiber optic implant. The emitted 530-nm signal from the indicator was collected via this same fiber and patch cord (Doric Lenses), spectrally-separated using a dichroic mirror, passed through a series of filters, and was focused on a scientific camera. Isosbestic signals were simultaneously captured by alternating excitation with 415-nm LED to dissociate motion, tissue autofluorescence, and photobleaching from true changes in fluorescence. For these dual-color experiments, we acquired data simultaneously from two channels by adding a 560-nm LED to excite jRGECO1a. All wavelengths were interleaved and collected simultaneously using Bonsai interfacing with the Neurophotometrics system (Lopes et al, 2015). The sampling rate for the calcium signals was 10 Hz per channel.

*3.2.5) Behavioral Testing*

On Day 1, mice were habituated for 600s to a neutral context (Cxt B) while undergoing optogenetic stimulation to control for encoding of a novel environment and light-stimulation alone (Coulbourn Instruments). Because they are still consuming a Dox diet, there should be no experience or engram ‘tagged ’during this time. After this session, the Dox-containing diet was replaced with standard mouse chow (ad libitum) 48 h prior to behavioral tagging to open a time window of activity-dependent labeling. On Day 3, mice were placed into the shock context (Cxt A) where they underwent CFC for 360s. Foot shocks (0.75mA, 2s duration) were administered at the 120s, 180s, 240s and 300s time

points and animals were immediately placed back on Dox diet for 24 h, closing the tagging window. This labeled sufficiently active cells with ChR2-eYFP or eYFP alone. On Day 4, mice were placed back in Cxt A where they received foot shocks on the previous day for 360s of 'natural recall'. On the following Day 5, ChR2-eYFP+ or eYFP+ cells were optogenetically stimulated (450nm laser diode, 20Hz, 10ms pulse, 15mW output) in Cxt B with alternating 2-min light-ON and light-OFF epochs [off/on/off/on/off] for a total of 600s (Doric Lenses). 90 min after the start of the last behavioral session, we performed perfusions to measure endogenous c-Fos at its peak, providing a proxy of recent neural activity resulting from optogenetic reactivation of dDG. Brains were sliced on a vibratome at 50μm thickness, immunohistochemistry, and confocal microscopy (Zeiss LSM800, Germany) were performed to quantitatively analyze the total number of 'tagged' cells in dDG, number of overlaps between endogenous c-Fos+ and 'tagged' ChR2/eYFP+ cells and expression profile of GCaMP6f and jRGECO1a. Time series data were analyzed in vCA1 from neurons and astrocytes across all experimental days.

All of these sessions took place in mouse conditioning chambers (Coulbourn Instruments) with metal-panel side walls, plexiglass front and rear walls and a stainless-steel grid floor composed of 16 grid bars (18.5 × 18 × 21.5cm). The grid floor was connected to a precision animal shocker to deliver 2 s duration, 0.75mA foot shocks. Context A was composed of this standard fear conditioning chamber with white light and no odorants. Context B was in a separate room, with a textured black floor to cover the shock grid, striped laminated walls, an orange odor, and red light in the front of the room. No auditory changes were made across contexts. A web camera was mounted in front of

the chamber to record animal behavior that was triggered by the onset of calcium recording in Bonsai/Neurophotometrics. The behavioral session was triggered by a computer running FreezeFrame4 software (Actimetrics). The chambers were cleaned with 70% ethanol solution prior to each animal placement.

*3.2.6) Immunohistochemistry*

On the final day of behavior, mice were overdosed with 3% isoflurane and perfused transcardially with cold (4°C) 1 X Phosphate-buffered saline (PBS; Gibco) followed by 4% Paraformaldehyde (PFA; pH = 7.4; Sigma-Aldrich) in PBS. Brains were extracted and kept in PFA at 4°C for 24–48 h. Brains were sectioned into 50μm thick coronal sections with a vibratome and collected in cold PBS or 0.01% sodium azide in PBS for long-term storage. Sections were washed three times for 10–15 min with PBS or PBST to remove 0.01% sodium azide used for storage. Vibratome sections were incubated for 2 h in PBS combined with 0.2% Triton (PBST; Teknova) and 5% bovine serum albumin (BSA; Sigma-Aldrich) on a shaker at room temperature for blocking. Sections were incubated in the primary antibodies (1:1000 rabbit polyclonal anti-cFos [SySy; #226 008]; 1:1000 chicken polyclonal anti-GFP [Invitrogen; #A10262]; 1:1000 guinea pig anti-RFP [SySy; #390 004] diluted in PBS/1% BSA/Triton X-100 solution at 4°C for 24–48 h depending on the stain of interest. The slices were washed three times for 10–15 min each in 1xPBS or 0.2% PBST. The secondary antibodies were diluted in secondary antibody solution (PBS/1% BSA/Triton X-100) and incubated for 2 h at room temperature. The following secondary antibodies were used: 1:200 Alexa goat anti-rabbit 555 [Invitrogen; #A-21428];

1:200 Alexa goat anti-chicken 488 [Invitrogen; #A-11039]; 1:500 Alexa goat anti-guinea pig 555 [Invitrogen; #A-11073]. The sections were then washed three times with 1xPBS or PBST for 10–15 min each and mounted using Vectashield HardSet Mounting Medium with DAPI (Vector Laboratories Inc.). Once dry, slides were sealed with clear nail polish on each edge and stored in a slide box in the fridge (4°C). Mounted slices were imaged using a confocal microscope (Zeiss LSM800, Germany). Brains from all mice used in fiber photometry experiments were analyzed to check adequate fiber location and proper and selective viral expression. Animals that did not meet the criteria for proper fiber location and virus expression were discarded.

*3.2.7) Image Acquisition*

All coronal brain slices were imaged through a Zeiss LSM 800 epifluorescence microscope with a 20x/0.8 numerical aperture objective using Zen2.3 software. Brains from all mice used in fiber photometry experiments were analyzed to check adequate fiber location and proper and selective viral expression. Animals that did not meet the criteria for proper fiber location and virus expression were discarded.

Images of the dDG were captured in a 2 x 4 tile (1280 x 640 μm) z-stack. DAPI, cFos and green fluorescent protein (GFP) were imaged as separate channels for target verification, ensemble size quantification and overlaps of ‘reactivation.’ 3-4 slices (6–8 dDG ROIs) were imaged for each animal for averaging.

*3.2.8) Quantification and statistical analysis*

All details of statistical analysis (statistical test used, n value, comparisons, test statistics, p-values, post-hoc multiple comparisons, outliers removed, and results of normality and variance measures) can be found in the Supplemental Statistical Table. Brief notes of statistical tests are included in the main and supplemental figure legends (statistical test, n value, outliers or mice removed). Statistical analyses were performed using Python and GraphPad Prism v10.

*Behavioral measures and event metrics:* For behavioral measures and event metrics, violin plots show the data distribution with dashed lines indicating the upper and lower quartiles and the solid line indicating the median. All data were checked for normality using Shapiro-Wilks and Kolmogorov-Smirnov tests, equality of variance (standard deviation) using Brown-Forsythe test and outliers using the ROUT method. This method was recommended by GraphPad Prism, which uses identification from nonlinear regression. We chose a ROUT coefficient Q value of 10% (False Discovery Rate), making the threshold for outliers less-strict and allowing for an increase in power for outlier detection. Mice that were excluded for other reasons, such as a lack of freezing epochs, were noted in the figure legends where applicable in peri-event analysis.

To analyze differences between groups for behavioral measures, event metrics and cross-correlation measures, we used: One-way ANOVAs (normal) or Kruskal-Wallis test (nonparametric) with Holm-Sidak's (normal) or Dunn's (nonparametric) post-hoc multiple comparisons tests, if applicable. If variances were not equal, a Brown-Forsythe ANOVA (normal) was performed instead with Dunnett's T3 multiple comparisons test, if applicable.

To analyze differences between groups and across time within a single session we used: Two-way repeated measures (RM) ANOVAs (between-subject factor: Group; within-subject factor: Time). Tukey's multiple comparisons was performed as a post-hoc multiple comparisons test, if applicable. For all tests, alpha was set to $p < 0.05$.

*Cell counts:* For cell counts, one-sample t-tests were used to statistically compare each group's mean overlap to chance/theoretical mean (1.0). For all tests, alpha was set to $p<0.05$.

*Simple linear regression:* For simple linear regression, X was denoted as the maximum cross-correlation value and Y as the average percent freezing for a single session. The solid line indicated the line of best fit that predicts Y from X with the associated 95% CI. $R^2$ goodness-of-fit measure, p-value and equation are reported in each plot, as well as in the supplemental Statistical Table. For all tests, alpha was set to $p<0.05$.

*Binomial generalized linear modeling:* To determine the probability of freezing behavior from neuron and astrocyte calcium signals, a binomial generalized linear model with logit link was used. Beta coefficients for astrocyte and neuron calcium signals in the regression models were compared across group using One-way ANOVAs (normal) or Kruskal-Wallis test (nonparametric) with Games-Howell pairwise post-hoc multiple comparisons tests. For area under the curve (AUC) comparison across groups, Welch's ANOVA or Kruskal-Wallis tests were performed on normal and nonparametric data. For all tests, alpha was set to $p<0.05$.

*3.2.9) Cell Counting Analysis*

dDG images were processed prior to quantification in FIJI (ImageJ). Images were processed using a custom macro to split channels, adjust brightness/contrast and z-project (maximum intensity). Regions of interest were selected using the Polygon tool so that only cells within the dDG granule cell layer were quantified. cFos, GFP and DAPI channels were separately quantified in Ilastik,41 a supervised machine-learning analysis tool. This method uses a pixel and object classification pipeline facilitated by a human annotator and allows for automated batch processing once the algorithm has been properly trained. Overlaps between cFos and GFP were quantified manually in FIJI (ImageJ) using the Cell Counter plug-in due to the small number of cells.

Once cells were counted, the amount of cFos+, GFP+ and cFos+GFP+ (overlap) cells in each slice were normalized to the total number of DAPI+ cells (cFos+/DAPI+, GFP+/DAPI+ and overlap/DAPI+). The chance of an overlap was defined as (cFos+/DAPI+) x (GFP+/DAPI+), which was calculated for each slice. Overlap/chance was then calculated by dividing overlap/DAPI by chance for each individual slice. Overlap/chance was averaged across all slices for each mouse to generate a single average value that was used in statistical analysis.

*3.2.10) Fiber Photometry Analysis*

*Pre-processing:* All fiber photometry analysis was performed using an in-house pipeline available at https://github.com/rsenne/RamiPho. Extracted photometry signals first underwent baseline correction using the adaptive iteratively reweighted Penalized

Least Squares (airPLS) algorithm. For this algorithm we set $\lambda = 10.7$ and $p = 0.05$ with a maximum of 100 iterations. Following baseline correction, we used a Kalman Filter to smooth each trace (Kalman, 1960). The Kalman Filter (or Gaussian Linear Dynamical System) is a model of the form:

$$x_t = Ax_{t-1} + q_t$$

$$y_t = Hx_t + r_t$$

Where $A$ is the state transition matrix, $H$ is the observation model matrix, $q_t$ is the process noise which is zero-mean Gaussian distributed with $Q_t$ covariance, $Q_t$ : $q_t \sim N(0, Q_t)$, and $r_t$ is the observation noise which is zero-mean Gaussian noise with covariance $R_t$: $r_t \sim N(0, R_t)$. To use the Kalman Filter we decided to use a p-order Autoregressive ($AR(p)$) process as a process model. We found that almost all photometry traces were well described by an $AR(3)$ model by plotting the partial autocorrelation functions and determining how many lags were outside of the theoretical 95% rejection region. To this end, we modeled every photometry trace as an $AR(3)$ process of the form:

$$x_t = \alpha_0 + \alpha_1 x_{t-1} + \alpha_2 x_{t-2} + \alpha_3 x_{t-3} + \epsilon$$

Where $x_t$ is the current time step, $x_{t-k}$ is the k-th previous timestep, $\alpha_0 - \alpha_3$ are constant coefficients and $\epsilon$ is a Gaussian distributed error term. Thus, for our state transition matrix and observation model matrix we used:

$$A = \begin{bmatrix} \alpha_1 & \alpha_2 & \alpha_3 \\ 1 & 0 & 0 \\ 0 & 1 & 0 \end{bmatrix}$$

$$H = [1 \quad 0 \quad 0]$$

For the model we set the initial covariance as the identity matrix *I* (3) and the initial state as the zero vector (0, 0, 0). We used the expectation-maximization algorithm to find the initial process noise and observation noise covariance matrices. We then used the Kalman (Rauch–Tung–Striebel) Smoother and then used the smoothed estimate of the hidden continuous state as our photometry trace. After smoothing, we then calculated $\frac{\Delta F}{F}$ as $\frac{x_t - median(x)}{median(x)}$ and also a z-scored version as $\frac{x_t - median(x)}{stdev(x)}$. Following this calculator, we then fit an ordinary least squares regression model to correct for motion and artifact noise in the recording according to the following model:

$$y_t = \beta_0 + \beta_1 x_t + \epsilon$$

Where y_t is the calcium indicator x_t is the isosbestic channel the \beta are constant coefficients and epsilon is Gaussian distributed noise. After fitting this model, we used the residuals as our motion corrected trace.

For event detection we used the find_peaks() function in Scipy. Two researchers manually choose parameters across all traces until they were both in agreement. Importantly, all parameters were chosen before any statistical or exploratory analysis was performed and were not altered at a later time point.

*Peri-event analysis:* For event-triggered average significance, we used a tCI confidence interval method previously proposed (Jean-Richard-Dit-Bressel, Clifford & McNally, 2020). For our event triggered averages we aggregated all within-animal signals so that we could assume that our samples were independent and identically distributed. Thus, for this method we assumed each time point was distributed according to a student-t's distribution. We then marked any period of time greater than 0.8 s (this decision was arbitrary and could be chosen to be longer for more conservative estimation, but this is longer than the proposed time threshold in the original paper) that did not include the baseline of 0 (traces were median-shifted to zero) was marked at a significant peri-event.

*Binomial Generalized Linear Modeling:* To assess how neural and astrocytic traces could be used to predict freezing we used a Binomial GLM with the canonical logit link function. For model selection, all data was pooled together on the Shock-ChR2 animals, and we performed 10-fold cross validation and used the Maximum Likelihood Ratio test to assess the following models 1) just a constant, 2) a constant and the astrocyte signal, 3) a constant and the neuronal signal, 4) and a constant, the astrocyte signal, and the neural signal. The MLRT results suggested that the full model was superior to all of the nested models. Our cross-validation approach also found that the full model was the most generalizable. After this model selection routine, we fit the chosen model to each animal's data separately.

*Cross-Correlation Analysis:* In the context of assessing the relationship between neuronal and astrocytic signals over time, max-cross correlation is calculated to determine the lag at which the similarity between the two signals is highest. The formula $R_{xy}(\tau)$ is

the expected value of the product of deviations from the mean of both signals, where one signal is shifted by the lag time $\tau$. The max-cross correlation is computed as follows:

$$R_{xy}(\tau) = E[(X(t) - \mu_x) \cdot (Y(t + \tau_{argmax}) - \mu_y)]$$

Here, X(t) represents the neuronal signal at time t, and $Y(t + \tau_{argmax})$ represents the astrocytic signal shifted by the lag time $\tau$ that maximizes the cross-correlation. $\mu_X$ and $\mu_Y$ are the means of the neuronal and astrocytic signals, respectively. The argmax function identifies the lag $\tau$ that maximizes the cross-correlation function. This approach identifies the time offset at which the two signals are most linearly related to each other, which could be indicative of the delay between neuronal activity and astrocytic response, or vice versa. The calculation of $R_{xy}(\tau)$ over different values of $\tau$ allows the identification of the time lag that corresponds to the peak of the cross-correlation function, hence the term "max-cross correlation". This peak value represents the strongest linear relationship between the two signals at the optimal lag time.

*3.2.11) Behavioral Analysis*

To perform unbiased behavioral evaluation, the pose estimation algorithm, DeepLabCut, was used for animal kinematics (position, acceleration, velocity)(Mathis et al, 2018). This open-source toolbox allows for training of a deep neural network using a small number of behavioral videos. This method was confirmed for accuracy by a blinded

researcher that manually scored a subset of videos. Additionally, Any-Maze (Stoelting Co.) was used for supervised automated analysis of freezing bout initiation and termination. This behavioral data was time locked to our fiber photometry time series data for analysis.

To extract acceleration and velocity information from DeepLabCut, we again used the Kalman Filter as described above. We first calculated the center of mass of the pose estimates for the mice to estimate the x and y coordinates. After this we then formulated a Kalman Filtering model using the following matrices:

$$A = \begin{bmatrix} 1 & 0 & \Delta t & 0 & 0.5\Delta t^2 & 0 \\ 0 & 1 & 0 & \Delta t & 0 & 0.5\Delta t^2 \\ 0 & 0 & 1 & 0 & \Delta t & 0 \\ 0 & 0 & 0 & 1 & 0 & \Delta t \\ 0 & 0 & 0 & 0 & 1 & 0 \\ 0 & 0 & 0 & 0 & 0 & 1 \end{bmatrix}$$

$$H = \begin{bmatrix} 1 & 0 & 0 & 0 & 0 & 0 \\ 0 & 1 & 0 & 0 & 0 & 0 \end{bmatrix}$$

$$Q = \begin{bmatrix} 0 & 0 & 0 & 0 & 0 & 0 \\ 0 & 0 & 0 & 0 & 0 & 0 \\ 0 & 0 & 0 & 0 & 0 & 0 \\ 0 & 0 & 0 & 0 & 0 & 0 \\ 0 & 0 & 0 & \Delta t^2 & 0 & 0 \\ 0 & 0 & 0 & 0 & \Delta t^2 & 0 \end{bmatrix}$$

$$R = \begin{bmatrix} Var(x) & 0 \\ 0 & Var(y) \end{bmatrix}$$

For the initial state mean we used: ( $x_1$, $y_1$, 0, 0, 0, 0) and for the initial covariance we used the identity matrix: $I(6)$. Using this method, we were able to extract smooth estimates of the (x, y) position, velocity, and acceleration.

### 3.3) Results

*3.3.1) In vivo calcium recordings of neurons and astrocytes in the ventral hippocampus during natural and artificial memory reactivation.*

We first monitored neuron and astrocyte calcium dynamics in hippocampal vHPC using dual-color fiber photometry in freely moving mice across habituation, CFC, natural recall and optogenetic ('artificial') reactivation of a tagged fear memory. Wild type mice were injected in vCA1 unilaterally with AAV5-GfaABC1D-GCaMP6f and AAV9-hSyn-jRGECO1a to express genetically-encoded calcium indicators (GECIs) in astrocytes and neurons, respectively. Additionally, these mice were bilaterally injected with the Tet-tag viral cocktail of AAV9-c-fos-tTA and AAV9-TRE-ChR2-eYFP or eYFP control in the dorsal DG to allow for temporal control over 'tagging' and reactivating a neuronal ensemble with this simultaneous recording of calcium dynamics (Figure 1A). jRGECO1a and GCaMP6f successfully and effectively expressed in vHPC neurons and astrocytes, respectively (Figure 1B). Across all days of behavior, we used fiber photometry to record freely moving neuronal and astrocytic calcium activity in the vHPC (Figure 1A, C). Mice were placed into three groups: Shock-ChR2 (mice that received foot shock and expressed active channelrhodopsin [ChR2] in tagged fear engram cells), Shock-eYFP (mice that received foot shock and expressed control eYFP in tagged fear engram cells) and Neutral-

ChR2 (mice that did not receive foot shock and express active ChR2 in tagged neutral engram cells). On Day 1, all mice remained on doxycycline (Dox) diet while they freely explored neutral Context B (Cxt B) and received blue-light stimulation for habituation. After this session, mice had Dox diet replaced with standard chow for 48 hours prior to the engram labeling. On Day 3, mice in the Shock-ChR2 and Shock-eYFP groups underwent CFC in Context A (Cxt A). Here, they received 4, 0.75mA foot shocks while off Dox. Mice in the Neutral-ChR2 group were placed in Cxt A for the same duration of time in the absence of aversive stimuli. After this session, all mice were returned to the Dox diet to close the 'tagging window'. On Day 4, all mice were placed back in Cxt A for contextual ('natural') recall. On Day 5, all mice were placed in the previously habituated Cxt B where they received blue-light stimulation during the 120-240 seconds and 360-480 second time periods. 90 minutes after the first light-ON epoch of optogenetic stimulation, mice were transcardially perfused to capture peak cFos protein levels and allow us to examine the 'reactivation rate' of tagged vs. reactivated neurons in dDG (Figure 1C).

Next, we performed histology to visualize the tagged dDG engram cells (green), reactivated cFos cells (red), DAPI (blue), and overlaps (yellow) for Shock-ChR2 (Figure 1D, top), Shock-eYFP (Figure 1D, center), and Neutral-ChR2 (Figure 1D, bottom). There were no statistically significant differences in the active cFos+ cells (%cFos+/DAPI+) across any group (Figure 1E). The percentage of tagged cells (%eYFP+/DAPI+) was significantly different across groups. Post hoc multiple comparisons demonstrated significantly greater eYFP+ "tagged" engram cells in the Shock-eYFP group compared with both the Shock-ChR2 and Neutral-ChR2 groups (Figure 1F). Additionally, there was

a significant increase in eYFP+ tagged cells in the Shock-ChR2 compared with the Neutral-ChR2 group (Figure 1F). These increased eYFP+ cells in the Shock-eYFP group compared with those expressing ChR2 is perhaps not unexpected because of the differences in molecular weight and ultimate localization of the effector protein in the cell. ChR2 requires trafficking to the cellular membrane for activation by optogenetics in addition to the cytosolic expression of eYFP. Finally, to assess the similarity of the initially "tagged" engram cells and those reactivated during optogenetic stimulation, we quantified the number of overlaps for each group cFos+eYFP+/DAPI+ compared with chance (eYFP+/DAPI+) × (cFos+/DAPI+). We observed that the overlaps/chance in the Shock-ChR2 and Neutral-ChR2 groups were significantly greater than the chance theoretical mean of 1.0 (Figure 1G). This result indicates that optogenetic stimulation of "active" ChR2 protein in our tagged cells, both fearful and neutral in nature, increased the number of reactivated cells from the initially labeled experience, whereas our eYFP group was not activated.

*3.3.2) Neurons and astrocytes respond robustly to foot shock and freezing epochs during contextual fear conditioning.*

To test the hypothesis that astrocytes and neurons play an active role in the acquisition of contextual fear, we used in vivo fiber photometry to record the activity of both cell types across all experimental days of our behavioral task (Figure 1A, bottom). During CFC, mice in the Shock-ChR2 and Shock-eYFP groups had significantly increased freezing levels compared with Neutral-ChR2 mice, which did not receive foot shocks

(Figure 2A-B). These mice acquired fear across the session, with an increase in the Shock-ChR2 and Shock-eYFP groups but not in the Neutral-ChR2 group (Figure 2A-B). Calcium time series for astrocytes (Figure 2C) and neurons (Figure 2D) in the Shock-ChR2 and Shock-eYFP groups indicated increased activity at the times of a 0.75-mA foot shock (120, 180, 240, and 300 s) but not in the Neutral-ChR2 group, which did not receive foot shocks. To better understand this assessment, whole-session peri-event analyses for astrocytes (Figure 2E) and neurons (Figure 2J) demonstrated a significant increase in activity at the onset of each foot shock. During the foot shocks, we observed a significant increase in the Z-scored %dF/F (change in fluorescence/baseline) for both astrocytes (Figure 2F) and neurons (Figure 2K) in the Shock-ChR2 and -eYFP groups but not in the Neutral-ChR2 group, as expected. Further, calcium event characteristics were calculated for neurons and astrocytes in all groups, as averaged for events within the entire session. Astrocytes that underwent shock displayed an increase in peak height (%dF/F) and area under the curve (AUC) as well as a decrease in full width half-maximum (FWHM) compared with those that did not receive shocks (Figure 2G–2I). On the other hand, neuronal calcium characteristics were not significantly different across any groups within CFC as a whole (Figure 2L–2N).

Next, we hypothesized that astrocytes and neurons would be time locked to the onset and offset of behavioral freezing bouts, in line with previous work from BLA astrocytes during fear learning (Suthard & Senne et al, 2023). Peri-event analysis of foot shocks showed that neurons and astrocytes are both time locked to 0.75-mA foot shocks, with neurons displaying a smaller amplitude event that begins shortly before astrocytic

calcium (Figure 2O, top and center), compared with those that did not receive an aversive stimulus (Figure 2O, bottom). For freezing onset, both neurons and astrocytes displayed a significant decrease in activity immediately before the start of the freezing bout, rebounding around 1–2 s post event (Figure 2P, top and center), which we did not observe in Neutral-ChR2 mice (Figure 2P, bottom). Interestingly, both astrocytes and neurons displayed a significant decrease in activity at the offset of freezing bouts in the Shock-ChR2 and -eYFP groups with little delay between the two cell types (Figure 2Q, top and center). As neurons and astrocytes showed coordinated activity at freezing bouts, we hypothesized that, as the freezing percentage increased, there would be an increase in correlation between cell types (max cross-correlation). To understand this, we performed cross-correlation between the neuron and astrocyte calcium time series for the entire CFC session (Figure 2R). We observed that the maximum cross-correlation value was not significantly different across the three groups (Figure 2S). Further, we performed a simple linear regression to see whether an increase in maximum neuron-astrocyte cross-correlation can predict an increase in an animal's freezing level. For CFC, we did not observe a significant relationship between cross-correlation and average percent freezing (Figure 2T).

*3.3.3) Neuronal and astrocytic calcium are responsive to freezing epochs during contextual recall.*

To understand vHPC neuron-astrocyte calcium dynamics during natural recall, mice were placed back in Cxt A in the absence of any aversive stimuli the next day. During

recall, mice in the Shock-ChR2 and Shock-eYFP groups expressed high levels of fear, as shown by increased freezing across the session (Figures 3A-B) compared with Neutral-ChR2 mice that did not experience foot shock the day before. Whole-session individual calcium time series (Figures 3C-D) and average traces (Figures 3E-F) for astrocytes and neurons showed qualitatively similar activity in shock groups during recall. Similar to CFC, there was a significant dip and rapid increase in the Z-scored %dF/F for both astrocytes and neurons at the onset of freezing bouts for the Shock-ChR2 and Shock-eYFP groups (Figure 3G, top and middle) that was not observed in the Neutral-ChR2 calcium (Figure 3G, bottom). Further, we observed a similar rapid decrease in calcium activity across cell types at the offsets of freezing bouts (Figure 3H, top and middle), which again was not observed in the Neutral-ChR2 mice (Figure 3H, bottom). Calcium event characteristics were calculated for both neurons and astrocytes across all groups during the entire recall session. Similar to CFC, astrocytes in the Shock-eYFP group displayed significantly increased peak height and AUC compared with the Neutral-ChR2 group (Figure 3I, K). The Shock-ChR2 group had a trend toward the same significant increase in peak height and AUC compared with Neutral-ChR2, with no difference between Shock-ChR2 and Shock-eYFP (Figure 3I, K). Again, neuronal calcium events did not differ significantly in any metric across groups during this entire session (Figures 3L–3N). We further investigated the relationship between neuron-astrocyte cross-correlation and freezing during recall, as consolidation of the memory may contribute to a stronger relationship between these factors. We observed that the maximum cross-correlation value was significantly higher in the groups that received foot shocks previously compared with

Neutral-ChR2 (Figure 3O). Finally, a simple linear regression revealed a significant positive relationship between the maximum cross-correlation and freezing with an increase in neuron-astrocyte correlation predictive of an increase in the animal's freezing behavior. With this information, we can conclude that increased maximum cross-correlation is positively associated with freezing levels (Figure 3P).

*3.3.4) Neuron-astrocyte calcium responds to freezing epochs during optogenetic reactivation of fear.*

To optogenetically reactivate a fear memory, mice were placed in previously neutral Cxt B for 600 seconds while receiving blue light stimulation during the 120-240 and 360-480 second time intervals. In our experiment, optogenetic reactivation drove the highest level of freezing in the Shock-ChR2 group, as expected (Figure 4A-B), though in an atypical manner from previously reported light-induced studies but nonetheless consistent with an overall increase in freezing behavior during stimulation (Kitamura et al, 2017; Power et al, 2023; Rahsepar et al, 2023). Interestingly, while we observe increases in freezing with the onset of blue light at the 120 and 360 second timepoints, the already extant freezing levels we believe reflect contextual generalization, which provides us with an opportunity to study global increases in freezing and its effects on intra-hippocampal dynamics. The Shock-eYFP group displays a moderate level of fear that is likely due to fear generalization (Figure 4A-B). As anticipated, Neutral-ChR2 mice display the lowest level of freezing, hovering around 20% on average across the session (Figure 4A-B). Qualitatively, there were no significant differences in individual nor in whole session

calcium timeseries across groups for both astrocytes (Figure 4C, E) and neurons (Figure 4D-I). There were no changes in calcium event metrics across all the groups in both cell types for the entire optogenetic session (Figure 4F-H, 4J-L). To further understand how these calcium event metrics may change within the optogenetic stimulation epochs, we compared the peak height, AUC and FWHM for each group (Shock-ChR2, Shock-eYFP, and Neutral-ChR2) across light ON (120-240s, 360-420s) and OFF (0-120s, 240-360s, 420-600s)(Figure S2). We found no significant differences between light ON and OFF epochs in any group for astrocytic calcium (Figure S2A-C). For neurons, there was a significant increase in AUC during the light ON epochs only for Shock-ChR2, but no differences in peak height or FWHM (Figure S2D-F). This is interesting, as this increase in AUC is unique to the group that is receiving optogenetic reactivation of a fear memory.

Additionally, there was no significant difference in maximum cross-correlation across all the groups during the optogenetic reactivation session (Figure 4M). However, a simple linear regression revealed a significant relationship between maximum cross-correlation and average freezing during this session (Figure 4N). However, the $R^2$ value for cross-correlation ($R^2 = 0.2114$) was lower during this session compared to recall ($R^2 = 0.3071$)(Figure 3P).

Interestingly, we observed coordinated calcium signatures in the Shock-ChR2 group time-locked to freezing onset and offset resembling those during natural recall in both Shock-ChR2 and Shock-eYFP mice (Figure 3G-H). Most notably, this time-locking to freezing epochs was not present in the Shock-eYFP and Neutral-ChR2 group during optogenetic reactivation (Figure 4O-P). Both the Shock-eYFP and Neutral-ChR2 exhibited

some level of freezing behavior, likely due to generalization of fear, but artificial reactivation of a fear memory re-engaged astrocytes and neurons calcium activity in a stereotyped manner characteristic of natural recall. Optogenetic stimulation onset and offset did not appear to significantly change calcium activity in either cell type, although blue light onset may have led to a decrease in calcium in both cell types specific to fear memory activation (Figure 3Q-R).

*3.3.5) Predictive reliability of freezing is present only in the Shock-ChR2 group.*

As astrocytes and neurons changed their dynamics in response to freezing onset and offset during optogenetic and natural memory recall, we next asked if freezing could be reliably predicted from the fiber photometry traces (Figure 3G-H, Figure 4O-P). To this end, we fit a binomial generalized linear model (GLM) with a logit link to the freezing as a function of the astrocytic and neuronal photometry signals. During model selection, (*see Methods*), we found that a model that used both neuronal and astrocytic signals was best able to predict freezing. Both coefficients were found to be statistically significant. We then fit this model to each animal during recall (Figure 5A-B). We found that the coefficients for the Shock-ChR2 group corresponding to the astrocytic photometry signal were not significantly different from the Shock-eYFP group but were significantly different from the Neutral-ChR2 group during natural recall (Figure 5B). Interestingly, we found no significant differences between the Shock-eYFP group's coefficients and the other groups, and we saw no significant differences in the coefficient values that correspond to the neuronal signal (Figure 5B). To assess the predictive validity of our model, we used

receiver operating characteristic (ROC) curves and the AUC metric (Figure 5C-D, 5G-H). We found during natural recall that the Shock-ChR2 group was not significantly better at predicting freezing than the Shock-eYFP group but was significantly better at predicting freezing than the Neutral-ChR2 group (Figure 5D). Again, we found that the Shock-eYFP group was not significantly different from either group. We next wanted to see how these results would change during artificial reactivation, especially as we saw a decoupling of the peri-event responses to freezing onset and offset between the Shock-eYFP groups during artificial reactivation (Figure 4O-P). Furthermore, we found that the astrocyte signal corresponding beta coefficients were significantly different in the Shock-ChR2 group compared with both other groups (Figure 5F). We again observed no statistical differences in the neuronal signal coefficients (Figure 5F) and then found that, in the AUC metrics, the Shock-ChR2 group had significantly better predictive power than both the Shock-eYFP and Neutral-ChR2 groups (Figure 5H). Overall, this analysis suggests that our optogenetic stimulation paradigm preserves freezing-specific information within the photometry signals of vCA1 neurons and astrocytes.

*3.3.6) Mice display low freezing and no differences in calcium dynamics across all groups during habituation*

On Day 1, mice were placed in a neutral Cxt B for a habituation session while receiving blue light stimulation during the 120-240 and 360-480 second time intervals. As expected, mice exhibited low levels of freezing because no cells were tagged with ChR2 (Figure S1A-B). Calcium timeseries and whole session peri-event analysis for astrocytes

(Figure S1C-E) and neurons (Figure 3D, 3I) showed qualitatively similar activity in all groups during habituation. Calcium event characteristics were calculated for all groups for both neurons and astrocytes by averaging across all events during the entire session. In both cell types, there were no significant differences in any event metrics: peak height, area under the curve, and full-width half-maximum (Figure S1F-M, S1J-L). Further, we calculated neuron-astrocyte cross-correlation, observing, as expected, non-significant differences across the three groups (Figure S1M). We fit a simple linear regression to test if differences in cross-correlation can predict the animal's average freezing level. During the habituation session, we did not observe a significant relationship between cross-correlation and freezing (Figure S1N). Next, we performed peri-event analysis to examine astrocytic and neuronal calcium dynamics at the timepoints of freezing initiation and termination, and the onset and offset of blue-light stimulation. During habituation, we did not observe the same stereotyped decreases and increases in calcium time-locked to freezing bouts observed during natural or artificial fear memory recall (Figure S1O-P). This confirms that the calcium signatures we observe during recall for both shock groups and artificial fear memory recall in the Shock-ChR2 group are unique to fear memory engagement. Blue-light stimulation onset and offset during habituation did not reliably time-lock to calcium in any group, with significant events likely related to spurious, noisy activity that we commonly observe during 'neutral' contexts (Figure S1Q-R)(Suthard & Senne et al, 2023).

## 3.4) Discussion

### *3.4.1) The role of neuron-astrocyte dynamics during natural and artificial fear memory*

In this study, we asked how artificial reactivation of fear ensembles affects intrahippocampal neuronal and astrocytic calcium activity and how this interfaces with fear behavioral states. Our data demonstrate the emergence of coordinated calcium signatures time locked to onset and offset of freezing during CFC that become more distinctive during natural recall in the Shock-ChR2 and -eYFP groups. This is consistent with previous findings from our lab showing that astrocytes in the BLA are time locked to freezing epochs during CFC and recall. Optogenetic reactivation of a dDG fear engram recapitulates these dynamics during freezing bouts, whereas stimulation of neutral-tagged neurons (Neutral-ChR2) and control Shock-eYFP mice do not, suggesting that this manipulation mimics the natural expression of fear.

### *3.4.2) Optogenetic stimulation of a fear engram elicits atypical behavioral response*

Based on previous work and the work of others, when mice with tagged Shock-ChR2+ cells undergo optogenetic stimulation of these fear-related neuronal ensembles, they display light-induced freezing behavior. For this reason, we expected that our mice in the Shock-ChR2 group would display high levels of freezing during the light-ON epochs and a decrease during light-OFF epochs. This “seesaw” effect is not typically observed in Shock-eYFP and Neutral-ChR2 groups, where they display lower levels of freezing overall. This is because the eYFP+ cells are not blue light sensitive and, thus, should not be “reactivated” or brought back online to drive fear, and the Neutral-ChR2 group has a

non-shock-related experience labeled. Our behavioral findings during optogenetic reactivation showed an increase in freezing with the onset of blue-light stimulation that was modest in the Shock-ChR2 group. In line with our observations, previous engram research has shown a range of variability in light-induced freezing behaviors driven by differences in stimulation frequency and brain region (Roy et al, 2022). For instance, recent work has shown a very modest increase between light-ON and -OFF epochs (e.g., ~5% changes in freezing) with optogenetic stimulation of the prefrontal cortex (PFC), which is consistent with our findings (Kitamura et al, 2017). This is further supported by other work showing large variability in freezing, with the distributions between shock and no shock largely overlapping and few mice driving this significant difference during the light-ON periods (Power et al, 2023). Further, when collapsed across the entire optogenetic session (light-ON and light-OFF epochs together for each group), this study observed no significant differences across shock and no-shock mice. Both of these studies nonetheless successfully dissociated light-induced changes in behavior from light-induced changes in cellular dynamics. Importantly, our optogenetic stimulation, although similarly modest in behavioral effects, indeed recapitulates coordinated calcium signatures resembling natural recall that are time locked to freezing behavior, only in the Shock-ChR2 group. This may suggest that, during fear states, and specifically during bouts of freezing, fear engram reactivation alters downstream neuronal and astrocytic calcium dynamics and that this alteration mimics natural fear states.

*3.4.3) Correlation between neuronal and astrocytic calcium can predict fear states.*

Due to the robust coordinated responses between neurons and astrocytes at the onset and offset of freezing epochs, we next tested whether the two cell types become more correlated with an increase in average fear. Our analysis showed no significant differences in maximum cross-correlations between groups during CFC. This is likely due to the emergence of the fear state across the session and may require consolidation of the memory (Kitamura et al, 2017). In line with this hypothesis, in natural recall there was increased correlation between neurons and astrocytes in the shocked groups compared with the no-shock group. A simple linear regression analysis revealed that cross-correlations had a linear relationship to average freezing in the session. During the artificial recall session, although the Shock-ChR2 group exhibited increased freezing levels and stereotyped calcium signatures time locked to freezing characteristic of natural fear, there were no significant differences in maximum cross-correlations. Moreover, we observed more variability in cross-correlations between animals in both shock groups compared with natural recall. We speculate that optogenetic stimulation of an engram multiple synapses upstream (Fanselow & Dong, 2010) alters natural dynamics and leads to decreased coordination between cell types across the session compared with recall. Despite the induction of elevated fear levels and stereotyped calcium time locking to freezing epochs during optogenetic reactivation, this artificial perturbation is likely to produce more variability, both behaviorally and cellularly.

*3.4.4) Statistical Modelling Enhances Interpretability of Engram Research*

The ability to manipulate engrams via inhibition or activation has been technologically feasible for the past two decades (Han et al, 2009; Liu & Ramirez, 2012), but the majority of research relies on using behavioral metrics (e.g., freezing) and or measurements of immediate-early gene (IEG) expression as the primary readouts. However, as real-time recording and concurrent optogenetic perturbations are becoming more prevalent, a higher level of cellular and behavior resolution is warranted to measure phenotypes in an unbiased manner. One caveat with using a single behavioral dimension to assay memory is that it makes a prima facie assumption that subjects are independent and identically distributed. However, several studies have shown that metrics including freezing are not always universally expressed and show considerable variability. For instance, the often-observed "bi-directional freezing" often observed during optogenetic stimulation is not always present (Kitamura et al, 2017; Power et al, 2023; Rahsepar et al, 2023). In this study, we propose that, as real-time recording approaches become more prevalent in engram research, statistical modeling will become indispensable. We used a classic statistical model, the GLM, which has been seminal in many other fields of neuroscience (McCullagh & Nelder, 1989). We found that using our two photometry signals from astrocytes and neurons reliably predicted freezing behavior in mice even though we observed non-traditional freezing curves. Accordingly, we speculate that engram stimulation preserves encoded "fear" states within the activity of vCA1 neurons and astrocytes. This suggests that, while engram stimulation is undoubtedly an artificial approach, we nonetheless observe physiological responses expected under natural fear

memory recall. We believe that this result, paired with our observation of significant peri-events in the Shock-ChR2 group only during optogenetic stimulation, advances the idea that our stimulation is recapitulating fear-related neuronal responses. It is worth underscoring that our model selection procedure suggests that neuronal signals are playing an important predictive role in our model, despite the absence of significant group-level differences in the corresponding beta coefficients. We believe that there are a few reasonable explanations that could resolve this conflict. For example, like other red calcium indicators, jRGECO1a has lower signal-to-noise ratio than its GCaMP6f counterpart, and so it is feasible that some animals will have much more reliable predictive capabilities in this channel than others. An additional caveat is that we fit a separate model to each of the animals and assume that each mouse is independent. Thus, future research could augment our approach in at least two manners: one could use a generalized linear-mixed effects model that would supply a maximum a posteriori estimate of the posterior distribution of the beta coefficients, or one could use a fully Bayesian approach and partial-pool all of the data to consider the inherent variability of different mice. Regardless, we believe that even simple statistical models, such as the ones used here, will enhance the interpretation of future engram studies.

*3.4.5) Advancing the study of natural and artificially-driven memories*

Our study demonstrates that optogenetic reactivation of a fear engram induces neuronal-astrocytic dynamics that resemble the cellular responses observed during natural fear memory recall. Interestingly, recent work has characterized the relationship between

phase-specific optogenetic stimulation of the DG and theta oscillations in dCA1 of the HPC using local field potentials. Here, they find that stimulation during the trough of theta is more effective at driving freezing behavior compared with the peak of theta. The variability in freezing behavior in our data could be potentially explained by imprecise stimulation patterns that do not yet consider phase-specific relationships between engram activation and ongoing rhythms in the brain (Rahsepar et al, 2023). This study also did not observe significant light-induced freezing during light-ON epochs at 20 Hz in the dDG but did observe this during trough stimulation, further supporting the notion that the brain contains optimal rhythmic windows during which optogenetic stimulation of an engram may be most effective at driving behavior. This work builds on others that have recorded from within or downstream of DG engram stimulation. For example, calcium recordings of *Fos*-dependent (F-RAM) and *Npas4*-dependent (N-RAM) ensembles expressing GCaMP after CFC revealed that they were differentially reactivated during recall in the DG, with the N-RAM ensemble uniquely engaging for memory discrimination (Sun et al, 2020). Further, single-unit electrophysiological activity in the BLA of mice while simultaneously activating DG positive engram cells had both excitatory and inhibitory effects on individual cells (Ramirez et al, 2015). Finally, 20-Hz stimulation of a sparse population of DG granule cells has been shown to excite and inhibit an equal number of neurons downstream in the CA3, which provides a putative mechanism for how both excitation and inhibition work together to effectively_express a memory (Lee et al, 2019). Together with this previous work, our study supports the idea that optogenetic reactivation is sufficient to induce behavioral and cellular fear states similar to those observed during natural recall.

*3.4.6) Limitations of the study*

In this study, we primarily use fiber photometry, which, despite its many applications in systems neuroscience research, has inherent spatial-temporal limitations for recording cellular activity in vivo. One such issue is the lack of standardization and agreement in the field for optimal photometry recording preprocessing. Furthermore, photometry's spatial resolution is such that activity of GECI+ cells is recorded as a 1-dimensional time series, which captures bulk fluorescence in a brain region of interest but is incapable of resolving individual cell responses. Importantly, calcium responses at the single-cell level have been shown to encode complex behavioral variables through a variety of physiological processes, including sequence development, polysynaptic input-output architectures, and within the cells themselves. Additionally, our optogenetic protocol specifically stimulates a fraction of dDG granule cells, and while this approach has been successful in prior engram work, increasing numbers of studies have shown that these memory ensembles are distributed units whose activity evolves with experience and time (Roy et al, 2022). Thus, it remains an open question whether stimulating engrams across the brain would also recapitulate endogenous physiological activity across multiple cell types, as we observed in our study.

**3.5) Author Contributions**

Conceptualization, R.L.S, R.A.S, S.R.; Methodology, R.L.S, R.A.S, S.R.; Formal Analysis, R.L.S, R.A.S, M.D.B; Investigation, R.L.S, R.A.S, M.D.B, A.D., A.Y.P.; Visualization, R.L.S, R.A.S; Writing – Original Draft, R.L.S, R.A.S, M.D.B, S.R.; Writing

– Review & Editing, R.L.S, R.A.S, M.D.B, S.R.; Funding Acquisition, S.R.; Resources, S.R. Supervision, S.R.

### 3.6) Acknowledgements

We thank members of the Ramirez laboratory for their helpful comments and suggestions on the manuscript. This material is based upon work supported by the Air Force Office of Scientific Research (AFOSR) under award number FA9550-21-1-0310, the Ludwig Family Foundation, an NIH Early Independence Award DP5 OD023106-01, NIH Transformative Award, Brain and Behavior Research Foundation Young Investigator Grant, McKnight Foundation Memory and Cognitive Disorders Award, Pew Scholars Program in the Biomedical Sciences, the Chan-Zuckerberg Initiative, and the Center for Systems Neuroscience and Neurophotonics Center at Boston University. Behavioral schematics were created using BioRender.com

### 3.7) Declaration of Interests

The authors declare no competing interests.

### 3.8) Data and Code Availability

All data reported in this paper will be shared by the lead contact upon request. All original code has been deposited at https://github.com/rsenne/RamiPho and is publicly available as of the date of publication. DOIs are listed in the key resources table. Any additional information required to reanalyze the data reported in this paper is available from the lead contact upon request.

## 3.9) Figures

### Figure 3.1

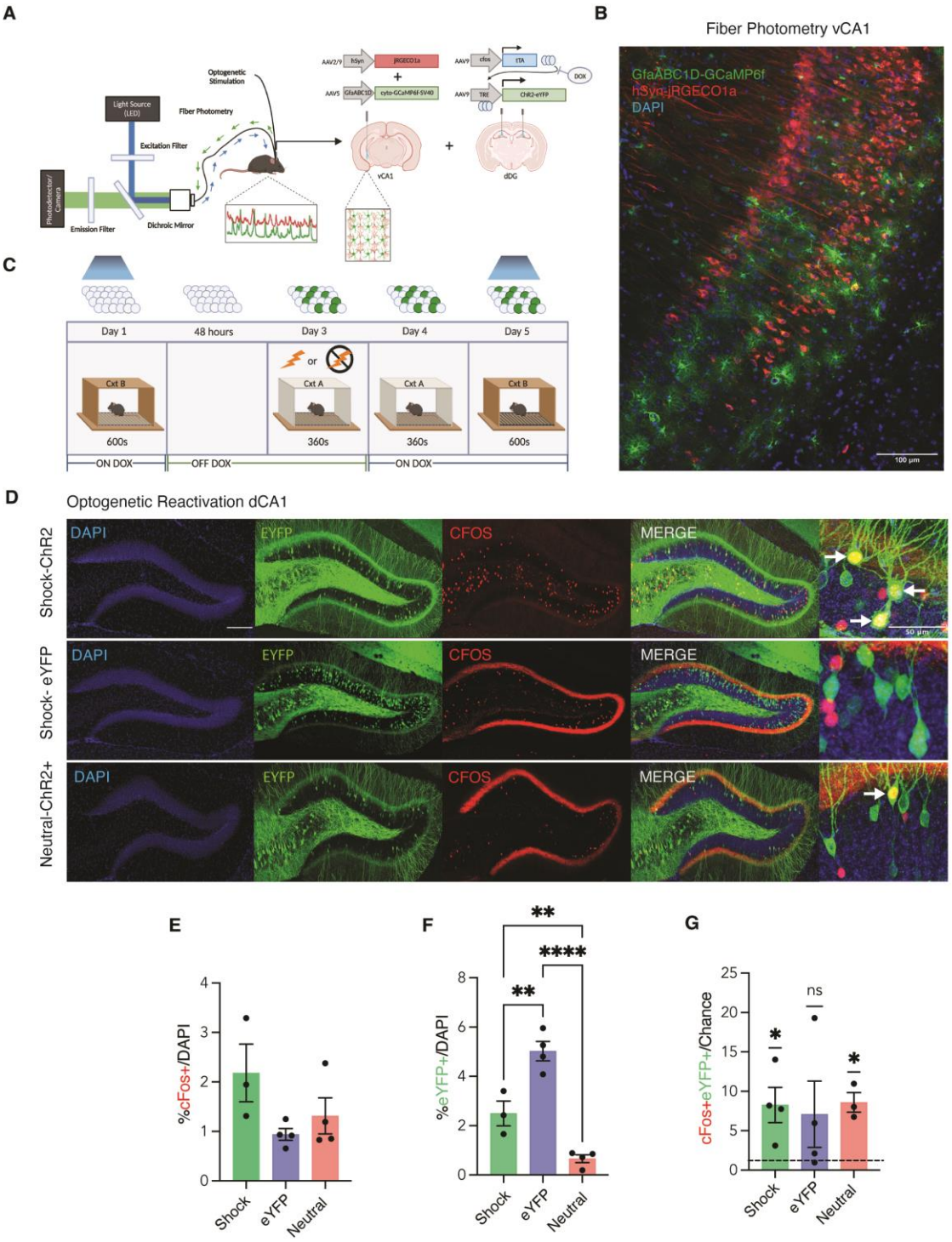

**Figure 3.1: In vivo calcium recordings of neurons and astrocytes in the ventral hippocampus during natural and artificial memory reactivation**. (A) Neuron-astrocyte fiber photometry recordings hippocampal ventral CA1 (vCA1) coupled with optogenetic stimulation of a dorsal dentate gyrus (dDG)-mediated neuronal ensemble. Mice were injected in vCA1 with AAV5-GfaABC1D-cyto-GCaMP6f-SV40 and AAV9-hSyn-jRGECO1a-WPRE.SV40, and received a unilateral optical fiber implant to enable Ca2+ recordings. dDG was infused with AAV9-c-fos-tTa and AAV9-TRE-ChR2-eYFP or control vector, and implanted with bilateral optical fibers. **(B)** Representative confocal microscopy image of the vCA1 pyramidal cell layer expression of hSyn-jRGECO1a (red; neurons), GfaABC1D-GCaMP6f (green; astrocytes) and DAPI (blue; nuclei) that was the site of fiber photometry recordings. **(C)** Schematic representation of the viral tagging strategy used during behavioral testing: On Day 1, mice were placed in Context B (Cxt B) for 600 seconds of habituation in the presence of blue light optogenetic stimulation while on DOX diet. DOX diet was removed for 48 hours immediately after this session to open the 'tagging' window. On Day 3, mice were split into three groups: Shock-ChR2, Shock-eYFP and Neutral-ChR2, where they underwent a neutral (no-shock) or contextual fear conditioning (4-shock; 0.75mA, 2 second duration foot shocks) experience for 360 seconds in Context A (Cxt A). Mice were placed immediately back on DOX diet to close the 'tagging' window. On Day 4, all mice were placed back in Cxt A for a 360 second natural recall session. Day 5 mice underwent a 600 second session in Cxt B where they received optogenetic blue light stimulation (450nm laser diode, 20Hz, 10ms pulse, 15mW) to 'reactivate' the tagged ensemble. 90 minutes after the start of optogenetic stimulation, mice

were transcardially perfused to capture peak endogenous cFos protein resulting from stimulation. **(D)** Representative 20x confocal images of dDG histology visualizing DAPI+ cells (blue), eYFP+ cells (green; active during FC), cFos+ cells (red; active during optogenetic stimulation) and overlaps (yellow; active during both sessions) between these three channels for each group: shock-ChR2 (top), shock-eYFP (middle) and neutral-ChR2 (bottom) to show the effects of optogenetic reactivation of ChR2+ or eYFP+ cells in the hippocampus. Zoomed representative 20x images of these overlaps (yellow) are shown in the far-right of each row with arrows highlighting these. **(E)** %cFos+/DAPI+ cells were not different across groups; One-way ANOVA. **(F)** %eYFP+/DAPI+ cells was significantly increased in Shock-ChR2 and Shock-eYFP groups; One-way ANOVA and Holm-Sidak's multiple comparisons. **(G)** %cFos+eYFP+/chance (overlap) cells were significantly greater than chance in Shock-ChR2 and Neutral-ChR2 groups; One-sample t-tests of each group against chance (1.0). *$p \leq 0.05$, **$p \leq 0.01$, ***$p \leq 0.001$, ****$p \leq 0.0001$, ns = not significant. Per group: n=3-4 mice x 8 dDG regions of interest (ROI) each were quantified for statistical analysis of cell counts. Error bars indicate SEM. Scale bars for 1B represent 100μm and 1D represent 200μm (20x; DAPI, eYFP, cFos, Merge) and 50μm (40x; Merge).

**Figure 3.2**

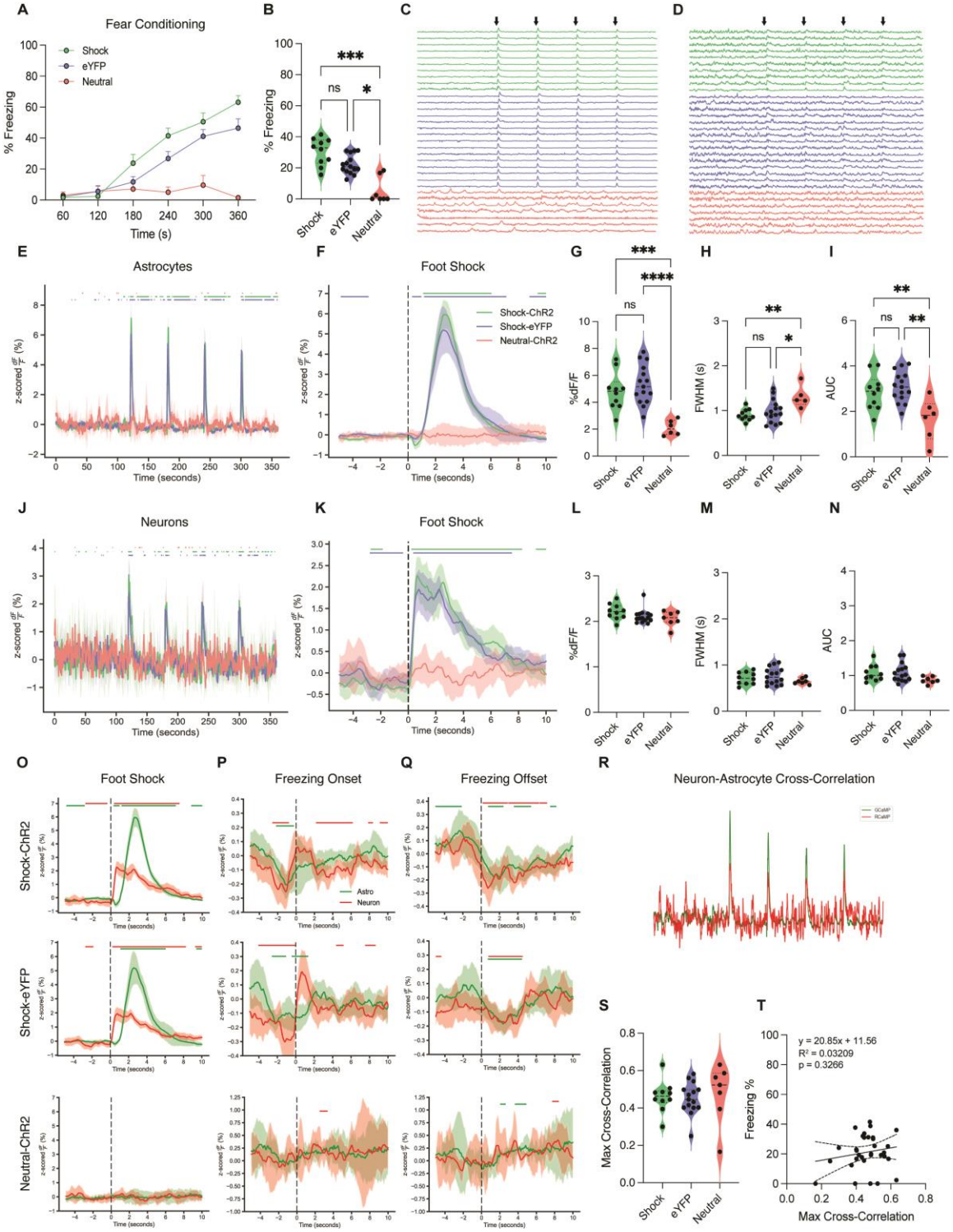
A
Fear Conditioning
Shock
eYFP
Neutral
% Freezing
Time (s)
B
% Freezing
***
ns
*
Shock
eYFP
Neutral
C
D
E
Astrocytes
z-scored dF/F (%)
Time (seconds)
F
Foot Shock
Shock-ChR2
Shock-eYFP
Neutral-ChR2
Time (seconds)
G
***
****
ns
%dF/F
Shock
eYFP
Neutral
H
**
ns
*
FWHM (s)
I
**
ns
**
AUC
J
Neurons
K
Foot Shock
L
%dF/F
M
FWHM (s)
N
AUC
O
Foot Shock
Shock-ChR2
Shock-eYFP
Neutral-ChR2
P
Freezing Onset
Astro
Neuron
Q
Freezing Offset
R
Neuron-Astrocyte Cross-Correlation
S
Max Cross-Correlation
T
y = 20.85x + 11.56
R² = 0.03209
p = 0.3266
Freezing %
Max Cross-Correlation

**Figure 3.2: Neurons and astrocytes respond robustly to foot shock and freezing epochs during contextual fear conditioning. (A-B)** Mice in Shock-ChR2 (green) and Shock-eYFP (blue) groups acquired fear during contextual fear conditioning (CFC) as shown by increased freezing percentage across the session (A) and on average (B) compared to Neutral-ChR2 (coral) mice that did not receive foot shock. **(C-D)** Calcium timeseries for astrocytes (C) and neurons (D) in the Shock-ChR2 and Shock-eYFP groups indicated increased activity at the times of 0.75mA foot shock (black arrows; 120, 180, 240, 300 seconds), but not the Neutral-ChR2 group. Each row represents a single subject across time (seconds). **(E, J)** Whole session peri-event analysis for astrocytic (E) and neuronal (J) calcium activity during CFC show an increase in activity (z-scored %dF/F) at the onset of each foot shock (dashed lines) in the Shock-ChR2 and Shock-eYFP groups. **(F, K)** Foot shock peri-event analysis for astrocytes (F) and neurons (K), with the onset of shock occurring at the dashed line (time = 0). Shock-ChR2 (green) and shock-eYFP (blue) show a significant increase in calcium activity (z-scored %dF/F), but neutral-ChR2 (coral) mice do not. **(G-I, L-N)** Calcium event metrics (z-scored) for astrocytes (G-I) and neurons (L-N) averaged across the entire CFC session; (G,L) peak height (%dF/F), (H,M) full-width half maximum (s), and (I,N) area under the curve (AUC). Astrocytes in Shock-ChR2 and Shock-eYFP groups show increased peak height and AUC, and decreased FWHM compared to Neutral-ChR2. Neurons show no significant differences in any metric during CFC across groups. **(O-Q)** Peri-event analysis for neurons (red) and astrocytes (green) during foot shock (O), freezing onset (P) and freezing offset (Q) for Shock-ChR2 (top), Shock-eYFP (middle) and Neutral-ChR2 (bottom). Shock-ChR2 and Shock-eYFP mice

show a significant response across cell types to foot shock, freezing onset and offset, compared to Neutral-ChR2 mice. **(R)** Representative neuron-astrocyte cross-correlation, with neurons (red) and astrocytes (green) shifted to maximally align with one another. **(S)** Maximum cross-correlation value (0.0-1.0) was not significantly different across groups during CFC. **(T)** Simple linear regression for average freezing percentage (%) and maximum cross-correlation value for all mice collapsed across groups during CFC did not show a significant relationship. For all violin plots, One-way ANOVA or Kruskal-Wallis tests were performed on normal and nonparametric data, respectively. For post-hoc multiple comparisons tests, Holm-Sidak's (normal) or Dunn's (nonparametric) multiple comparisons were performed with *$p \leq 0.05$, **$p \leq 0.01$, ***$p \leq 0.001$, ****$p \leq 0.0001$, ns = not significant. For peri-event analysis, we used a 95% tCI (shaded region) confidence interval method where a 'significant' event indicated by the colored bars above the timeseries indicates any time period greater than 0.8 seconds that did not include the median-shifted baseline of 0. Error bars in line plots are represented as mean ± SEM. Violin plots display the data distribution with dashed lines indicating upper and lower quartiles and the solid line indicating the median. For simple linear regressions, the solid line indicates the line of best fit that predicts Y from X with the associated 95% CI. $R^2$ goodness-of-fit measure, p-value and equation are reported. For event metrics and freezing behavior, shock n=10, eYFP n=15, neutral n=6-7; only one mouse in the neutral group was excluded as an outlier for astrocytic FWHM. For foot shock peri-event analysis, shock n=10, eYFP n=15, neutral n=7. For freezing onset and offset peri-events, shock n=10,

eYFP n=15, neutral n=3; four neutral mice were excluded due to their entire lack of freezing during CFC.

**Figure 3.3**

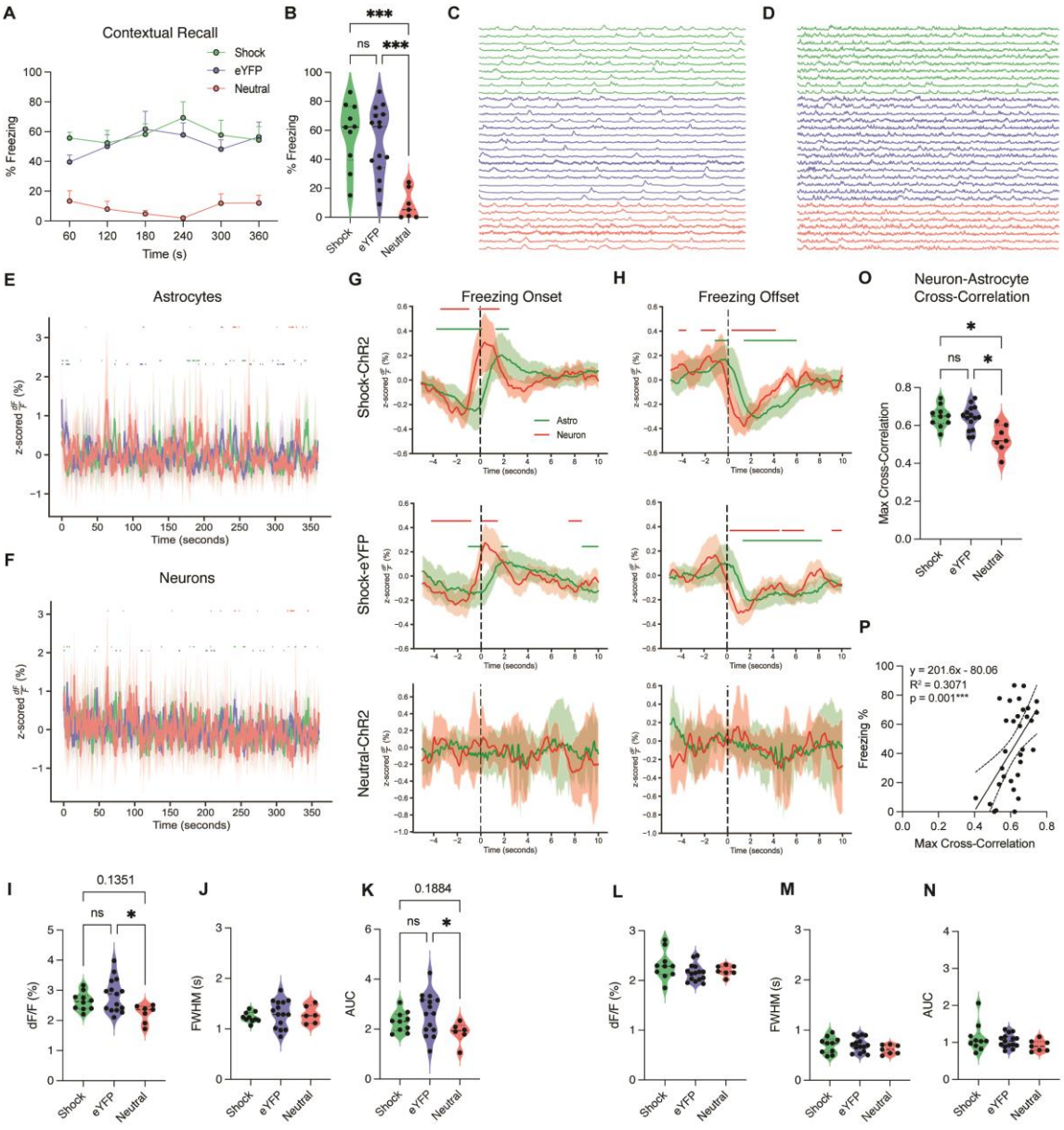

**Figure 3.3: Neuronal and astrocytic calcium are responsive to freezing epochs during contextual recall in shock, but not neutral groups. (A-B)** Mice in Shock-ChR2 (green) and Shock-eYFP (blue) groups expressed high levels of contextual fear recall, as shown by increased freezing percentage across the session (A) and on average (B) compared to Neutral-ChR2 (coral) mice that did not receive foot shock the day before. **(C-D)** Calcium timeseries for astrocytes (C) and neurons (D) in the Shock-ChR2 and Shock-eYFP groups indicated similar qualitative activity in both cell types compared to Neutral-ChR2. Each row represents a single subject across time (seconds). **(E-F)** Whole session peri-event analysis for astrocytic (E) and neuronal (F) calcium activity during recall showed similar activity (z-scored %dF/F) across all groups. **(G-H)** Peri-event analysis for neurons (red) and astrocytes (green) during freezing onset (G) and freezing offset (H) for Shock-ChR2 (top), Shock-eYFP (middle) and Neutral-ChR2 (bottom). Shock-ChR2 and Shock-eYFP mice showed a significant response across cell types to freezing onset and offset, compared to Neutral-ChR2 mice. **(I-N)** Calcium event metrics (z-scored) for astrocytes (I-K) and neurons (L-N) averaged across the entire recall session; (I, L) peak height (%dF/F), (J, M) full-width half maximum (s), and (K, N) area under the curve (AUC). Astrocytes in Shock-ChR2 and Shock-eYFP groups showed significant or a trend towards an increase in peak height and AUC compared to Neutral-ChR2. Neurons showed no significant differences in any metric during recall across groups. **(O)** Neuron-astrocyte cross-correlation; maximum cross-correlation value (0.0-1.0) was significantly increased in both shock groups compared to neutral-ChR2 during recall**. (P)** Simple linear regression for average freezing percentage (%) and maximum cross-correlation value for all mice collapsed across groups

during recall showed a significant relationship. For all violin plots, One-way ANOVA or Kruskal-Wallis tests were performed on normal and nonparametric data, respectively. For post-hoc multiple comparisons tests, Holm-Sidak's (normal) or Dunn's (nonparametric) multiple comparisons were performed with *$p \leq 0.05$, **$p \leq 0.01$, ***$p \leq 0.001$, ****$p \leq 0.0001$, ns = not significant. For peri-event analysis, we used a 95% t-confidence interval (tCI) (shaded regions) method where a 'significant' event indicated by the colored bars above the timeseries indicates any time period greater than 0.8 seconds that did not include the median-shifted baseline of 0. Error bars in line plots are represented as mean ± SEM. Violin plots display the data distribution with dashed lines indicating upper and lower quartiles and the solid line indicating the median. For simple linear regressions, the solid line indicates the line of best fit that predicts Y from X with the associated 95% CI. $R^2$ goodness-of-fit measure, p-value and equation are reported. For event metrics and freezing behavior, shock n=10, eYFP n=15, neutral n=6-7; only one mouse in the neutral group was excluded as an outlier for astrocytic FWHM. For freezing onset and offset peri-events, shock n=10, eYFP n=15, neutral n=5; two neutral mice were excluded due to their entire lack of freezing during recall.

**Figure 3.4**

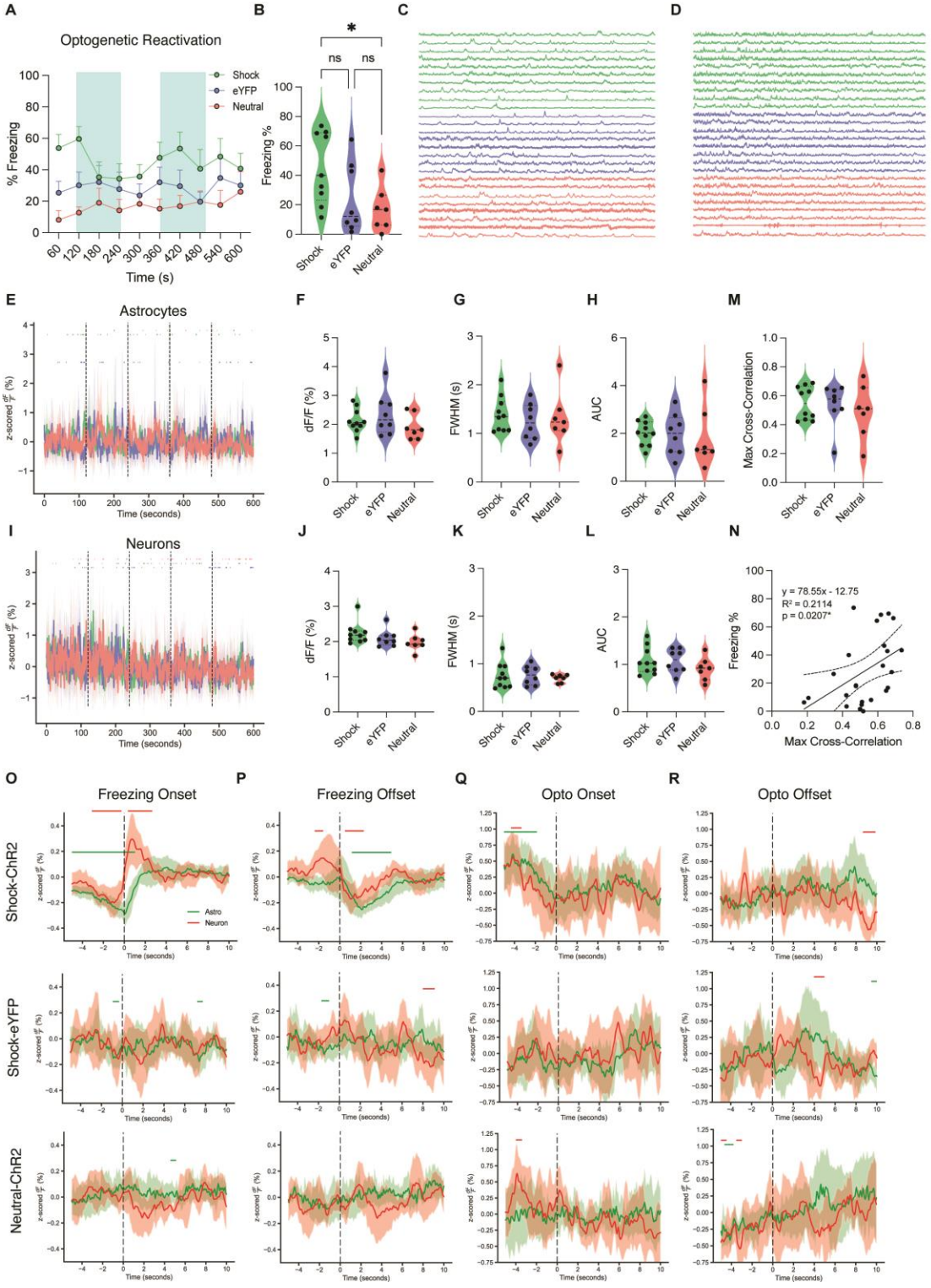
A
Optogenetic Reactivation
% Freezing
Time (s)
Shock
eYFP
Neutral
B
Freezing %
ns
ns
*
C
D
E
Astrocytes
z-scored dF/F (%)
Time (seconds)
F
dF/F (%)
G
FWHM (s)
H
AUC
M
Max Cross-Correlation
I
Neurons
J
K
L
N
Freezing %
y = 78.55x - 12.75
R² = 0.2114
p = 0.0207*
Max Cross-Correlation
O
Freezing Onset
P
Freezing Offset
Q
Opto Onset
R
Opto Offset
Shock-ChR2
Shock-eYFP
Neutral-ChR2
Astro
Neuron

**Figure 3.4: Neuron-astrocyte calcium responds to freezing epochs during optogenetic reactivation of fear. (A-B)** Mice in Shock-ChR2 (green) expressed higher levels of freezing across the session (A) and on average (B) during optogenetic reactivation of a fear memory compared to Shock-eYFP (blue) and Neutral-ChR2 (coral) groups expressing moderate and low levels of fear, respectively. Blue shading indicates the light ON epochs (120-240s; 360-480s) during the 600 second session. **(C-D)** Calcium timeseries for astrocytes (C) and neurons (D) indicated similar qualitative activity in both cell types across all groups during optogenetic reactivation. Each row represents a single subject across time (seconds). **(E, I)** Whole session peri-event analysis for astrocytic (E) and neuronal (I) calcium activity during recall showed similar activity (z-scored %dF/F) across all groups. **(F-H, J-L)** Calcium event metrics (z-scored) for astrocytes (F-H) and neurons (J-L) averaged across the entire optogenetic reactivation session; (F, J) peak height (%dF/F), (G, K) full-width half maximum (seconds), and (H, L) area under the curve (AUC). Neurons and astrocytes showed no significant differences in any metric across groups**. (M)** Neuron-astrocyte cross-correlation; maximum cross-correlation value (0.0-1.0) was not significantly different across any groups during the session. **(N)** Simple linear regression for average freezing percentage (%) and maximum cross-correlation value for all mice collapsed across groups during optogenetic reactivation showed a significant relationship. (**O-R)** Peri-event analysis for neurons (red) and astrocytes (green) during freezing onset (O), freezing offset (P), optogenetic stimulation onset (Q) and offset (R) for Shock-ChR2 (top), Shock-eYFP (middle) and Neutral-ChR2 (bottom). Shock-ChR2 mice showed a significant response across cell types to freezing onset and offset that is not

present in other groups. For all violin plots, One-way ANOVA or Kruskal-Wallis tests were performed on normal and nonparametric data, respectively. For post-hoc multiple comparisons tests, Holm-Sidak's (normal) or Dunn's (nonparametric) multiple comparisons were performed with *$p \leq 0.05$, **$p \leq 0.01$, ***$p \leq 0.001$, ****$p \leq 0.0001$, ns = not significant. For peri-event analysis, we used a 95% t-confidence interval (tCI) (shaded regions) method where a 'significant' event indicated by the colored bars above the timeseries indicates any time period greater than 0.8 seconds that did not include the median-shifted baseline of 0. Error bars in line plots are represented as mean ± SEM. Violin plots display the data distribution with dashed lines indicating upper and lower quartiles and the solid line indicating the median. For simple linear regressions, the solid line indicates the line of best fit that predicts Y from X with the associated 95% CI. $R^2$ goodness-of-fit measure, p-value and equation are reported. For event metrics and freezing behavior, shock-ChR2 n=10, shock-eYFP n=9, neutral-ChR2 n=7; one shock-ChR2 mouse was excluded as an outlier. For peri-events, shock-ChR2 n=10, shock-eYFP n=8, neutral-ChR2 n=7.

**Figure 3.5**

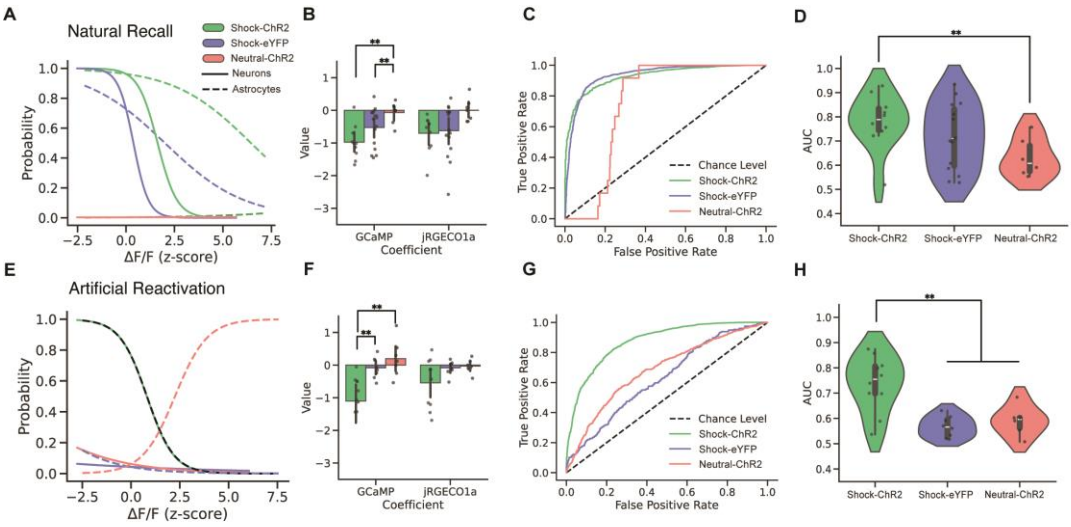


**Figure 3.5: Optogenetic reactivation of a hippocampal engram preserves cellular signals of fear**. **(A)** Best-fitting model for each group during natural recall. Lines reflect partial effects where the other signal is held at the mean value to show how the probability of freezing changes as a function of signal value. **(B)** Values of beta coefficients for astrocyte and neuronal photometry signals in the regression models during natural recall. **(C)** Receiver operating characteristic (ROC) plot for the best fitting model for each group. **(D)** Area under the curve (AUC) values for each model across groups. **(E)** Best-fitting model for each group during artificial reactivation. Lines reflect the partial effects where the other signal is fixed to the mean. **(F)** Beta coefficients for each signal across groups during artificial reactivation. **(G)** ROC plot for the best fitting model for each group. **(H)** AUC values for each model across groups. For the logistic regression model, a binomial generalized linear model with logit link was used with neurons (solid lines) and astrocytes (dashed lines) for each group: Shock-ChR2 (green), Shock-eYFP (blue) and Neutral-ChR2

(coral). For the bar plots showing beta coefficients for each group, One-way ANOVA or Kruskal-Wallis tests were performed on normal and nonparametric data, respectively. For post-hoc multiple comparisons, Games-Howell pairwise comparisons were used. For AUC violin plots, Welch's ANOVA or Kruskal-Wallis tests were performed on normal and nonparametric data. For all of the above tests mentioned, statistical significance is indicated with *$p \leq 0.05$, **$p \leq 0.01$, ***$p \leq 0.001$, ****$p \leq 0.0001$, ns = not significant. Error bars in bar plots are represented as mean ± SEM. Violin plots display the data distribution with dark regions indicating the upper and lower quartiles and the solid white line indicating the median.

**Figure S1**

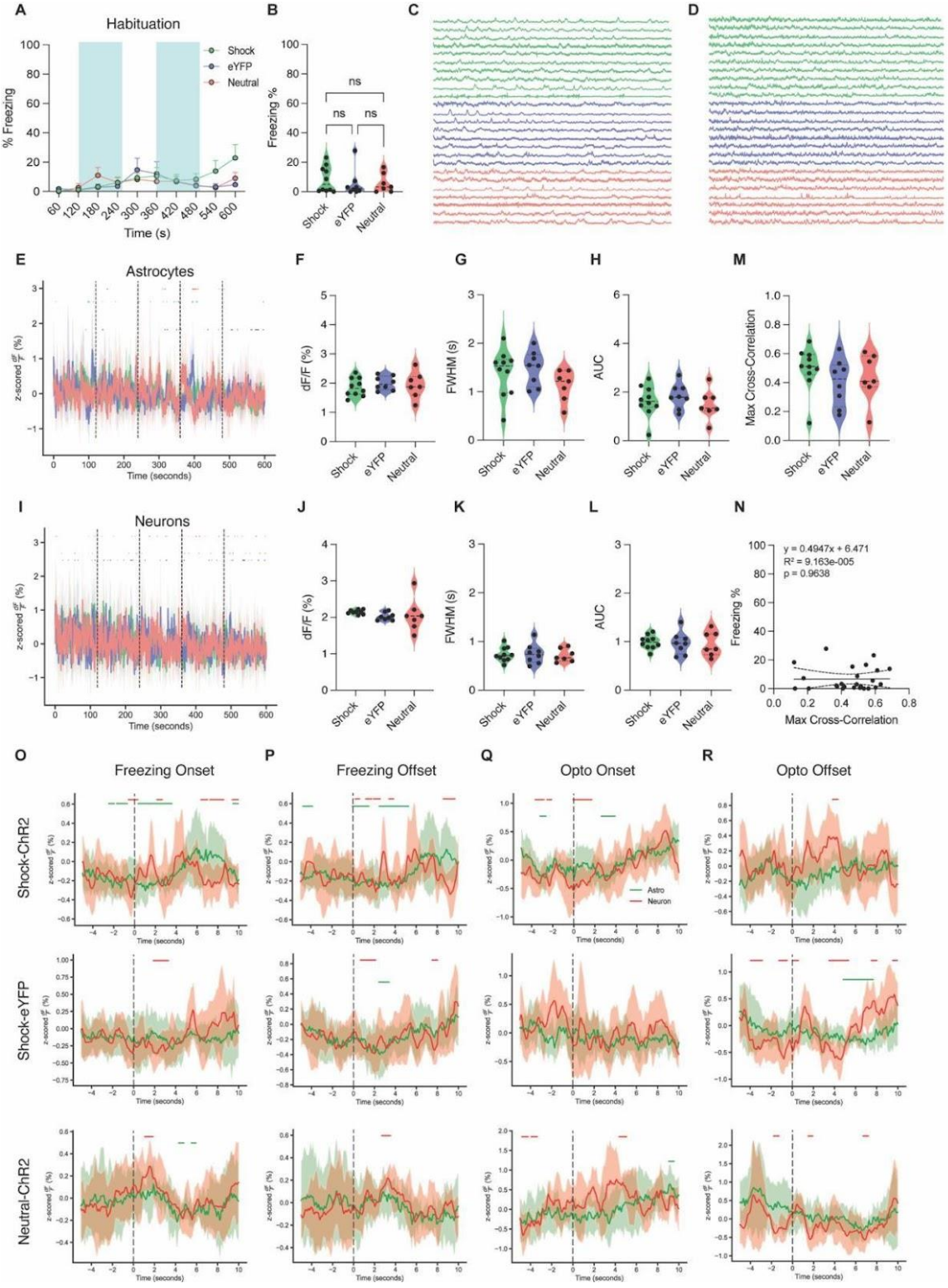
A
Habituation
% Freezing
Time (s)
Shock
eYFP
Neutral
B
Freezing %
ns
ns
ns
C
D
E
Astrocytes
z-scored dF/F (%)
Time (seconds)
F
dF/F (%)
G
FWHM (s)
H
AUC
M
Max Cross-Correlation
I
Neurons
J
K
L
N
y = 0.4947x + 6.471
R² = 9.163e-005
p = 0.9638
Max Cross-Correlation
O
Freezing Onset
P
Freezing Offset
Q
Opto Onset
R
Opto Offset
Shock-ChR2
Shock-eYFP
Neutral-ChR2
Astro
Neuron

**Figure S1 (*related to Figure 4*): Mice display low freezing and no differences in calcium dynamics across all groups during habituation.**

**(A-B)** Mice in all groups, Shock-ChR2 (green), Shock-eYFP (blue) and Neutral-ChR2 (coral) expressed low levels of fear, as evidenced by freezing percentage across the session (A) and on average (B). Blue shading indicates the light ON epochs (120-240s; 360-480s) during the 600 second session. **(C-D)** Calcium timeseries for astrocytes (C) and neurons (D) indicated similar qualitative activity in both cell types across all groups during habituation. Each row represents a single subject across time (seconds). **(E, I)** Whole session peri-event analysis for astrocytic (E) and neuronal (I) calcium activity during habituation showed similar activity (z-scored %dF/F) across all groups. **(F-H, J-L)** Calcium event metrics (z-scored) for astrocytes (F-H) and neurons (J-L) averaged across the entire habituation session; (F, J) peak height (%dF/F), (G, K) full-width half maximum (s), and (H, L) area under the curve (AUC). Neurons and astrocytes showed no significant differences in any metric during the session across groups. **(M)** Neuron-astrocyte cross correlation; maximum cross-correlation value (0.0-1.0) was not significantly different across any groups during the session. **(N)** Simple linear regression for average freezing percentage (%) and maximum cross-correlation value for all mice collapsed across groups during habituation showed no significant relationship. **(O-R)** Peri-event analysis for neurons (red) and astrocytes (green) during freezing onset (O), freezing offset (P), optogenetic stimulation onset (Q) and offset (R) for Shock-ChR2 (top), Shock-eYFP (middle) and Neutral-ChR2 (bottom). All groups showed significant periods of time for either cell type, but no evident pattern of activation occurred during each event. For all

violin plots, One-way ANOVA or Kruskal-Wallis tests were performed on normal and nonparametric data, respectively. For post-hoc multiple comparisons tests, Holm-Sidak's (normal) or Dunn's (nonparametric) multiple comparisons were performed with $p \leq 0.05$, $^{**}p \leq 0.01$, $^{***}p \leq 0.001$, $^{****}p \leq 0.0001$, ns = not significant. For peri-event analysis, we used a 95% tCI confidence interval method where a 'significant' event indicated by the colored bars above the timeseries indicates any time period greater than 0.8 seconds that did not include the median-shifted baseline of 0. Error bars in line plots are represented as mean ± SEM. Violin plots display the data distribution with dashed lines indicating upper and lower quartiles and the solid line indicating the median. For simple linear regressions, the solid line indicates the line of best fit that predicts Y from X with the associated 95% CI. $R^2$ goodness-of-fit measure, p-value and equation are reported. For event metrics and freezing behavior, shock-ChR2 n=10, shock-eYFP n=8, neutral-ChR2 n=7; one shock-ChR2 mouse was excluded as an outlier for neuron peak height. For peri-events, shock-ChR2 n=10, shock-eYFP n=8, neutral-ChR2 n=5; two neutral-ChR2 mice were removed due to a lack of freezing epochs.

**Figure S2**

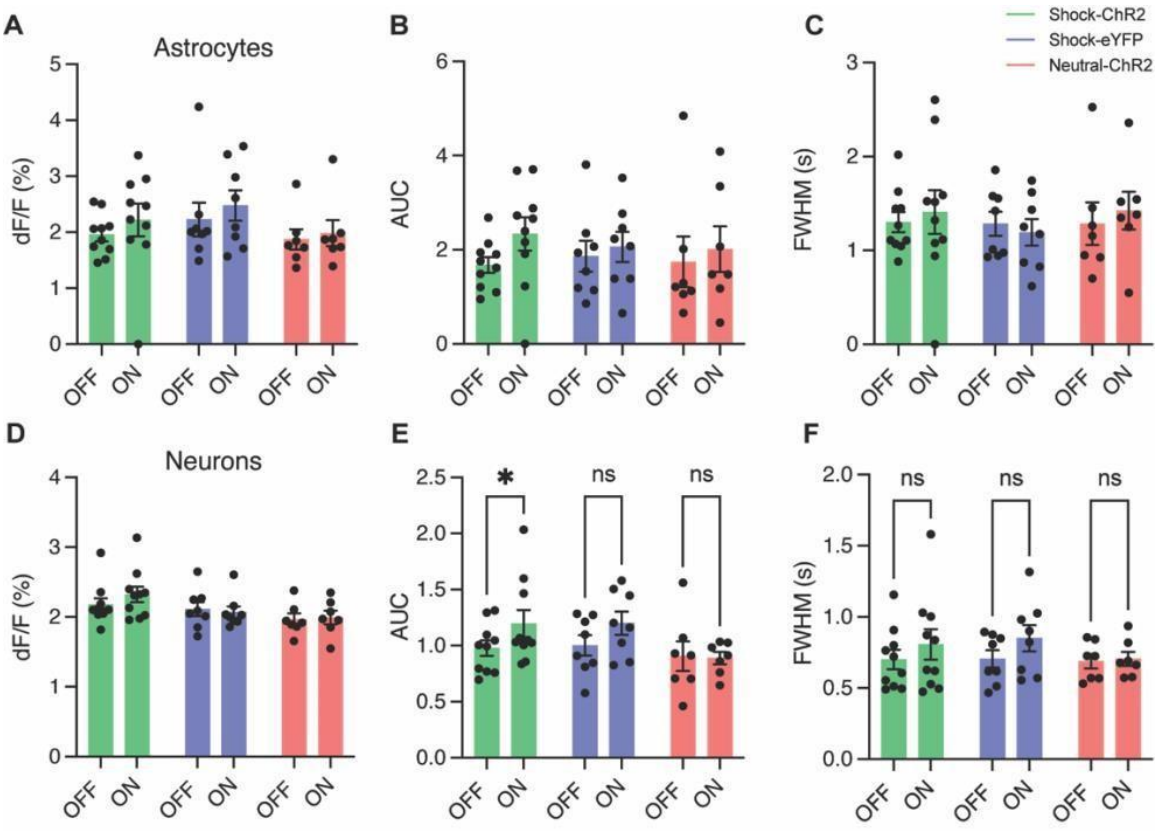


**Figure S2 (*related to Figure 4*): Neurons display increased area under the curve during light ON epochs in the Shock-ChR2 group. (A-F)** Calcium event metrics (z-scored) for astrocytes (A-C) and neurons (D-F). (A, D) peak height (%dF/F), (B, E) area under the curve (AUC) and (C, F) full-width half maximum (s). Astrocytes showed no significant differences in any metric between light ON and OFF epochs during optogenetic reactivation. Neurons had an increased AUC during the light ON epochs only in the Shock-ChR2 group. OFF epochs include 0-120s, 240-360s, 420-600s and ON epochs include 120-240s and 360-420s. For all bar plots, Two-Way ANOVA with repeated measures (ON/OFF) were performed to analyze effects of group (Shock-ChR2 (green), Shock-eYFP (blue) and Neutral-ChR2 (coral)) and Light (ON/OFF). For post-hoc multiple comparisons

tests, Holm-Sidak's (normal) multiple comparisons were performed with $p \leq 0.05$, $^{**}p \leq 0.01$, $^{***}p \leq 0.001$, $^{****}p \leq 0.0001$, ns = not significant to compare light ON vs. OFF epochs for each group. Error bars in line plots are represented as mean ± SEM. For event metrics: Shock-ChR2 n=10, Shock-eYFP n=8, Neutral-ChR2 n=7; no outliers were removed.

# CHAPTER FOUR: SEQUENCES OF ASTROCYTE ACTIVATION MIRROR MEMORY FOR FEARFUL EVENTS IN THE DORSAL HIPPOCAMPUS


## Abstract

The dorsal hippocampus primarily relies on pyramidal neurons to encode the spatiotemporal components of episodic memory. Recent work has shown that astrocytes are also key members of higher-level cognitive processes like learning and memory, working together with neurons to generate complex representations of the world. Our study explores this role further using one-photon imaging in dorsal CA1, a subregion where place and time cells are canonically studied within the rodent brain. We discovered that astrocytes are shock-responsive, displaying sequences that are akin to hippocampal time cells at the onset of these aversive stimuli. Notably, these sequences reappear during contextual recall and seem to be driven by reactivated astrocytes across days. These preliminary findings hint at astrocytic involvement in temporal coding and provide evidence that this reappearance during recall may serve as a memory-specific retrieval mechanism. Further analysis aims to delineate the characteristics of these sequences across fear conditioning and recall, and how they may be coupled with fear-related behaviors like freezing.


## 4.1) Introduction

The dorsal hippocampus is a heterogenous structure with numerous cell types involved in generating and maintaining detailed representations of space and time that

contribute to the formation of episodic memories. Within the hippocampus, pyramidal cells are the primary neuronal subtype that function as place and time cells, each developing spatially-tuned receptive fields within an environment (O'Keefe, 1976; O'Keefe & Dostrovsky, 1971; O'Keefe & Speakman, 1987; McNaughton, 2006) or tiling the temporal plane thorough sequential activity (Eichenbaum, 2014; Mau et al, 2018). Glial cells, on the other hand, have been largely ignored in this realm of spatiotemporal processing until recently. Recent findings have shown that astrocytes work together with neurons in a synergistic and complementary manner to represent spatial information in dorsal CA1 of the hippocampus (dCA1) (Curreli et al, 2022), and may encode reward location via similar spatial mechanisms (Doron et al, 2021). Additionally, computational modeling has proposed that astrocytic neuromodulation is sufficient to generate neuronal place fields via enhanced theta oscillations and plasticity changes (Polykretis & Michmizos, 2022). Together, these findings open the door to studying astrocytic involvement in spatiotemporal processing during memory formation and retrieval and how it relates to neuronal activity within these circuits.

To investigate the role of astrocytes in spatiotemporal processing within the hippocampus during memory encoding and recall, our study employed astrocytic one-photon imaging in the dCA1 region. First, we tracked astrocytes across days to understand how reactivated cells play a role in learning and memory processes. Secondly, we found that astrocytes are shock-responsive in dCA1 at the single-cell level, replicating previous findings from our lab and others. However, we find novel evidence that astrocyte sequences were triggered by the onset of these aversive foot shocks during contextual fear

conditioning. These sequences exhibited similar properties preliminarily to those displayed by canonical hippocampal time cells in response to other types of stimuli. Interestingly, these sequences reappeared during contextual recall and were driven by reactivated astrocytes that were active across days. These findings suggest a potential role of astrocytes in temporal coding within memory circuits and may serve as a behaviorally-relevant retrieval mechanism. Ongoing analysis aims to further characterize these sequences, examining their persistence across days, how they relate to contextual memory recall and behaviors like freezing.

## 4.2) Methods

### *4.2.1) Subjects*

The animals used in this study were male, wild-type C57BL6 (P29-35; 17-19g) mice obtained from Charles River Laboratories at the time of surgery. Animals were housed in the Boston University animal facilities in standard ventilation cages on a 12:12 dark/light cycle (0700-1900) and given ad libitum access to standard food and water. Mice were housed with littermates in cages with 4-5 mice and after GRIN lens implantation, they were individually-housed to prevent any damage to their implants. Due to individual-housing, mice were given additional enrichment in the form of supplemental bedding materials and a cardboard hut. Following GRIN lens surgery, mice were given 10 days to recover before the start of behavior. All subjects were treated in accord with protocol 201800579 approved by the Institutional Animal Care and Use Committee (IACUC) at Boston University. No statistical methods were used to determine sample size, but were

instead based on sample sizes of previous one-photon imaging studies. All n-values for each experimental group (Cxt A, Cxt B) can be found within the Results section as mentioned.

*4.2.2) Stereotaxic Surgery*

**Viral transduction:** Mice were anesthetized with 3-3.5% isoflurane during induction and maintained at 2-3% inhalation using stereotaxic nose cone delivery (oxygen 1.2 L/min). Paralube ophthalmic ointment was applied regularly to the eyes to maintain adequate lubrication. Scalp hair was removed using Veet or Nair hair removal cream; this was subsequently removed using applications of betadine solution and ethanol (70%). Lidocaine hydrochloride (2.0%) was injected subcutaneously (SQ) as a local analgesic agent under the scalp prior to incision. Meloxicam (0.1mg/kg) was administered SQ at the start of surgery. After scalp incision, mice received a unilateral (right) craniotomy with a 0.5-0.6mm drill bit for the dorsal hippocampal CA1 (dCA1) viral injection. A 10uL airtight Hamilton syringe with an attached 33-gauge beveled needle was used to inject AAV-GfaABC1D-cyto-GCaMP6f-SV40 (Penn Vector Core) at the coordinates of dCA1: -2.00 anteroposterior (AP), +1.40 mediolateral (ML) and -1.50 dorsoventral (DV). All coordinates are given relative to bregma (mm). 1000nL of undiluted virus was injected at 50nL/min using a microinfusion pump (UMP3; World Precision Instruments). After injection, the needle remained at the site of injection for 5-7 minutes to prevent viral spread. After injection, the incision was sutured closed using 4/0 Non-absorbable Nylon Monofilament Suture (Brosan). At the end of surgery, mice were injected with a 0.1mg/kg

intraperitoneal (IP) dose of buprenorphine. Following surgery, mice were placed in a clean recovery cage with a heating pad until regaining reflexes. To allow time for viral expression and recovery, mice were monitored for 2 weeks prior to implantation of GRIN lens surgery.

**GRIN lens implantation:** After 2 weeks, we inserted a GRIN lens (Inscopix, Inc.). 30 minutes prior to surgery, mice were injected with 0.1mL of dexamethasone diluted in 0.1mL sterile saline IP to reduce brain swelling. Mice were prepared as described above and the previous incision site was reopened. A 0.5-0.6mm drill bit was used to drill a 1mm craniotomy around the previous site of injection at the coordinates listed above. Using vacuum suction, 30 to 34-gauge needle attachments and constant administration of cold, sterile saline, brain tissue was aspirated down just beyond the thick fibers of the corpus callosum. Blood control was performed using absorbable gelatin sponge (Surgifoam). A GRIN lens and integrated base plate were lowered slowly to -1.30DV and a biocompatible silicone adhesive (Kwik-Sil) was used to seal off the exposed perimeter of the lens and skull. Multiple layers of adhesive cement (C&M Metabond) were applied up to the cuff of the integrated base plate and the headcap was completed with darkened dental cement (Stoelting). Mice were administered the same doses of postoperative analgesics described above. They were able to recover for 10 days before imaging experiments were performed during our behavioral paradigm.

*4.2.3) Behavioral testing*

Prior to behavioral testing, all mice were handled and habituated to being plugged into the miniature microscope. On Day 1, mice were subjected to contextual fear conditioning (CFC) for 330 seconds in Context A (Cxt A), where they received foot shocks (0.75mA, 2s duration) at the 120, 180, 240 and 300 second time points. On Day 2, mice underwent a 330s contextual recall session in the same mouse conditioning chamber (Cxt A) or were instead exposed to a novel Context B (Cxt B) for the same duration of time (330s).

**Context parameters:** Cxt A was a standard mouse conditioning chamber (18.5 x 18.5 x 21.5 cm; Coulbourn Instruments) with metal-panel side walls, plexiglass front and rear walls and a stainless-steel grid-floor (16 bars) that were connected to a precision animal shocker (Actimetrics). Cxt B was a standard mouse conditioning chamber of the same size in a different behavioral room that was modified to have striped plastic walls, almond scent, and a clear plastic floor. No lighting differences or the presence of auditory stimuli existed in either context. Ethanol (70%) was used to clean Cxt A, while Rescue disinfectant spray was used to clean in Cxt B to maintain these odor profiles.

*4.2.4) One-photon imaging*

**Acquisition:** All imaging experiments were conducted on awake, behaving mice in a freely-moving manner in standard mouse conditioning chambers. GCaMP6f fluorescence signals were imaged using a miniature integrated fluorescence microscope system (Inscopix Inc.) with GRIN lenses implanted in the dorsal CA1 of the hippocampus

(dCA1). Before the start of imaging, the miniature microscope was attached to the baseplate and adjusted to determine the best focal plane and gain for each mouse to achieve the best fluorescence signals. These values were maintained across all recording sessions. Frequency (Hz) and LED output power were consistent across all mice. Video was captured using the nVista Imaging System (Inscopix Inc.) that was triggered by an external TTL to time lock our behavioral session to calcium recordings (FreezeFrame4).

**Pre-Processing:** Calcium imaging data were pre-processed using the Data Processing Software (Inscopix, Inc.; IDPS). Videos were cropped from 1280 x 800 pixels to 1200 x 800 pixels and spatially down sampled by a factor of 4, from 1200 x 800 pixels to 300 x 200 pixels and temporally down sampled by a factor of 2 from 20 to 10 Hz. A spatial bandpass filter was applied using the default settings in IDPS (low cut off: 0.005 and high cut-off = 0.500). Motion correction was performed with the first frame as the global reference frame origin. PCA-ICA and CNMFe analysis failed to identify individual astrocytes in a reliable manner. Thus, to identify individual cells, pre-processed images were converted to dF/F using the mean frame as a reference. Regions of interest (ROI)s were selected by manually identifying astrocytic cell bodies with high contrast over the course of the session, and contours were drawn to contain the pixels of the somatic ROI. To validate this method, ROIs were further confirmed by visual inspection of the individual cell time series, and only those with clearly identifiable signals across two individual researchers were included in further analysis.

**Longitudinal registration of cells:** Longitudinal cell ROI registration was performed using the open-source Matlab program, CellReg, that utilizes a probabilistic

method for tracking cells across multiple sessions (Sheintuch et. al., 2017). In brief, it first aligns each session field-of-view (FOV) to one another by projecting the centroid locations of all the cells' spatial footprints onto one image. It maximizes the cross-correlation between the projections of each session to the reference session (Day 1; fear conditioning). We utilized non-rigid transformations, as they best aligned our dataset. Next, the Pearson correlations between the spatial footprints of the pairs of neighboring cells were calculated, estimating the probability of them being the same cell across sessions (Psame) with a maximum distance of 13-14 um. Further, the data is modeled as a weighted sum of the two distributions (same and different cells), allowing for an estimate of the false-negatives and false-positives. Finally, Psame = 0.50 (default) was utilized as an input for a clustering algorithm. CellReg registered cell outputs were confirmed visually using custom Python scripts that allowed confirmation of proper cell pairs and generation of a csv file that contained the indices of each cell on Day 1 and 2, if applicable, with a value of -1 indicating the cell not being present on that day.

**Behavioral analysis:** Freezing behavior was scored using Any-Maze (Stoelting Inc.).

*4.2.5) Immunohistochemistry*

After the completion of experiments, mice were overdosed with 3% isoflurane and transcardially perfused with cold phosphate buffered saline (PBS), followed by 4% paraformaldehyde (PFA) in PBS. Brains were extracted and placed in PFA at 4℃ for 24-48 hours. All brains were sliced coronally at 50um on a vibratome into cold PBS or 0.01%

sodium azide in PBS for long term storage. Native green fluorescent (GFP) protein signal from the GCaMP6f expression was assessed and sections were counterstained for both astrocytes and neurons using immunohistochemistry (IHC).

For IHC, dorsal CA1 (dCA1) sections underwent three washes in PBS for 5-10 minutes each to remove the 0.01% sodium azide storage solution. Sections were washed in 0.2% Triton X-100 in PBS (PBST) for 3 x 5 minutes each at room temperature. Next, slices were blocked for 2 hours in 1% bovine serum albumin (BSA) and 0.2% Triton X-100 in PBS solution on a shaker at room temperature. Sections were incubated in primary antibodies (1:1000 mouse anti-GFAP [NeuroMab] or 1:500 polyclonal guinea anti-NeuN/Fox3 [SySy]; 1:1000 chicken anti-GFP) made in the same 1% BSA/PBS/Triton X-100 solution at 4C for 24-48 hours.

Sections underwent 3 x 5-minute washes in PBST to remove the primary antibody solution. Sections were incubated in secondary antibodies (1:1000 Alexa Fluor 555 goat anti-mouse IgG [Invitrogen] or 1:1000 Alexa Fluor 555 goat anti-guinea pig [Invitrogen]; 1:1000 Alex Fluor 488 goat anti-chicken [Invitrogen]) for 2 hours at room temperature on a shaker. Sections were washed 3 x 10 minutes in PBST, and subsequently mounted onto microscope slides (VMR International, LLC) with Vectashield HardSet Mounting Medium with DAPI (Vector Laboratories, Inc.). These were allowed to dry for 24 hours at room temperature and edges of the coverslips were clear nail polished to maintain moisture. Slides were stored in a slide box in 4C after imaging.

*4.2.6) Statistical Methods*

All details of statistical analysis (statistical test used, n values, test statistics, p-values, post-hoc multiple comparisons, outliers removed) can be found in-text and in figure legends, where applicable. Statistical tests were performed using Python and GraphPad Prism v10.

For analysis of average percent freezing, total number of active cells, and reactivation percentage, plots show the distribution of data with utilizing bar, line, and box plots. All data were checked for normality using Shapiro-Wilks and Kolmogorov-Smirnov tests, equality of variance (standard deviation) using Brown-Forsythe test and outliers using the ROUT method. This method was recommended by GraphPad Prism, which uses identification from nonlinear regression. We chose a ROUT coefficient Q value of 10% (False Discovery Rate), making the threshold for outliers less-strict and allowing for an increase in power for outlier detection. Using this method, no outliers were detected across any of the analyses performed. To analyze differences in freezing or number of active cells, we used a Two-way repeated measures (RM) ANOVA (between-subject factor: Group; within-subject factor: Day) followed by Sidak's post-hoc multiple comparisons, where applicable. To analyze differences in reactivated cell percentage, we used an Independent t-test. For all tests, alpha was set to $p < 0.05$.

For event-triggered average significance (foot shock), we used a tCI confidence interval method previously proposed (Jean-Richard-Dit-Bressel, Clifford & McNally, 2020). For our event triggered averages we aggregated all within-animal signals so that we could assume that our samples were independent and identically distributed. Thus, for this

method we assumed each time point was distributed according to a Student-t's distribution. We then marked any period of time greater than 0.8 s (this decision was arbitrary and could be chosen to be longer for more conservative estimation, but this is longer than the proposed time threshold in the original paper) that did not include the baseline of 0 (traces were median-shifted to zero) was marked at a significant peri-event.

## 4.3) Results

### *4.3.1 One-photon imaging of dorsal hippocampal astrocytes across contextual fear learning and recall.*

To study how astrocytes are involved in temporal coding within a contextual fear conditioning paradigm, we performed one-photon (1p) imaging of dCA1 astrocytes in freely-moving mice (Figure 1A). Wild type C57BL/6J mice were injected with 1000nL of an astrocyte-specific genetically-encoded calcium indicator (GECI), AAV5-GfaABC1D-cyto-GCaMP6f, into unilateral dCA1. After recovery and viral expression, mice had a gradient index (GRIN) lens implanted above the pyramidal cell layer of dCA1 to allow visualization of the GCaMP-expressing astrocytes (Figure 1A-B). Selective expression of this GCaMP in astrocytes was assessed with co-staining of neurons (NeuN) or astrocytes (GFAP), where we observed successful labeling of astrocytes in and around the pyramidal cell layer (Figure 1C).

On Day 1 of behavior, all mice (n=7) underwent contextual fear conditioning (CFC) in Context A (Cxt A) to acquire the association between the conditioned stimulus (context; CS) and unconditioned stimulus (foot shock; US) which were paired at the 120, 180, 240

and 300 second time points during a 330 second session (foot shocks; 2s duration; 0.75mA intensity) (Figure 1A). On Day 2 of behavior, mice were split into two groups where they were placed back into Cxt A for recall (n=4; Context A Group) or into a novel Context B (Cxt B) (n=3; Context B Group) for the same duration of time each of those days to control for the memory-specific nature of our findings and the effects of time (Figure 1A). Behaviorally, there was a significant interaction of Day and Group, as well as a main effect of Group for average freezing levels (Figure 1D)(Two-way RM ANOVA; [Interaction] $F(1,5) = 21.68$, $p=0.0056$; [Day] $F(1,5) = 2.232$, $p=0.1954$; [Group] $F(1.5) = 10.17$, $p=0.0243$; [Subject] $F(5,5) = 2.269$, $p=0.1948$). Post-hoc multiple comparisons showed that mice in Cxt A and B froze at the same level on Day 1 during CFC as expected (Figure 1D)(Sidak's multiple comparisons [Day 1]: $p = 0.9960$). While on Day 2, mice in the Cxt A group froze significantly more than the Cxt B group because they were re-exposed to the fearful context (Figure 1D)(Sidak's multiple comparisons [Day 2]: $p = 0.0008$).

*4.3.2) Longitudinal registration of astrocytes*

In order to assess astrocytes across Day 1 and 2, we longitudinally tracked regions-of-interest (ROIs) from each imaging session. We successfully tracked these astrocytes across days using a combination of manual ROI selection within each session and CellReg, a Matlab-based tool that aligns cell footprints across sessions using field-of-view (FOV) alignment and probabilistic modeling of spatial footprints (Sheintuch et al, 2017). CellReg identified astrocytes active on Day 1 or Day 2 only, as well as those that overlapped or were 'reactivated' on Day 2. A representative footprint map shows all cells active during

CFC from a FOV that were detected using manual ROI selection (Figure 1E). Identification of tracked cells across Day 1 and 2 of behavior is shown in a representative output image from CellReg, where green ROIs were detected across both sessions (Figure 1F). While the footprints may appear distorted in size across days, we believe this is a result of the nonlinear transformation and scaling that was utilized to overlap the two spatial maps during registration.

We next tracked astrocytes across days and qualitatively observed two mild, albeit non-significant, trends: there were a similar number of total cells active on Day 1 during CFC across both groups and a drop-off in the number of cells active in the Cxt B group on Day 2 compared to Day 1. However, statistical analysis revealed no significant differences in the total number of active cells on Day 1 vs. Day 2 (Day) or across Cxt A or Cxt B (Group) (Figure 1G) (Two-way ANOVA RM; [Day x Group] $F(1,5) = 0.6655$, $p=0.4517$; [Day] $F(1,5) = 2.954$, $p=0.1463$; [Group] $F(1,5) = 0.6988$, $p=0.4413$; [Subject] $F(5,5) = 5.454$, $p=0.0431$). This may be due to a limitation in our group sizes (n=3-4) that may not allow us to truly parse this difference out statistically, as is frequently an issue in small-sampled 1p imaging experiments. Further, tracking of astrocytes across days allowed us to look at the percentage of cells that were ‘reactivated’ or were present on Day 1 and Day 2. We hypothesized that there would be more reactivated cells in the Cxt A group because they were placed back into the original fearful context, compared to the Cxt B group. Qualitatively, there appeared to be a greater percentage of reactivated cells (% reactivated cells/ total cells Day 1) in Cxt A, but there was no statistically significant difference

between the two groups, only a trend (Figure 1H)(Independent t-test; t = 2.441, df = 5, p=0.0586).

Together, we show for the first time that tracking of astrocytes across days during 1p imaging is technically possible using our pipeline. Additionally, we conclude that there is a similar number of cells active across CFC and Day 2 in our groups, where a larger sample size may reveal a drop in active cells in the Cxt B group. Finally, we show a trend towards a larger percentage of reactivated cells in Cxt A vs. B, potentially suggesting astrocytic involvement in a memory-specific process at the single-cell level.

*4.3.3) Astrocytes are shock-responsive during contextual fear conditioning*

During the CFC session, all mice across both groups received foot shocks (n=7). Here, astrocytes were significantly activated after the onset of each foot shock, peaking around 5 seconds post-stimulus (Figure 2A). This event-triggered average shows the average calcium transient for each group (Cxt A = blue; Cxt B = orange) representing all astrocytes and all animals within the session (Figure 2A). This finding is in line with previous work from our lab and others showing astrocyte shock response in the hippocampus, cortex, and amygdala (Suthard & Senne et al, 2023; 2024; Qin et al, 2020). This is recapitulated within the representative traces shown for Cxt A and B groups, with almost all astrocytes displaying a robust response to one or more shocks during the CFC session (Figure 2B). It is notable that qualitatively there are unique kinetics (rise and decay time), and number of shocks responded to at the single-cell level, with some astrocytes responding rapidly and decaying more quickly, while others displayed much slower decay

times (Figure 2B). This idea that there may be cells that respond to shock in a temporally-unique manner led us to further investigate the temporal structure of calcium responses to foot shock during CFC.

*4.3.4) Evidence of astrocytic temporal sequences after foot shock onset*

First, we plotted heatmaps containing the average calcium response for all astrocytes, for each animal, at the timing of foot shock (120, 180, 240, 300 seconds). We sorted these heatmaps by the maximal z-scored calcium response and plotted a range of time -14 to 28 seconds around foot shock. Qualitatively, we observed a hook-like structure that spans from approximately 18 to 28 seconds after foot shock, resembling some activity that is typical of hippocampal time cells in all of our animals (**Figure 3A**). On a larger scale, we also plotted heatmaps for all astrocytes across the entire CFC session sorted the same way to get a gross picture of their behavior during the 330 seconds (**Figure 3B**). Again, we observe remarkable coordinated activity at each of the foot shocks that maintain this hooked structure and tile some duration of time between the 60 seconds until the next shock in all animals. Before the onset of the first shock at 120 seconds, there is very little astrocytic calcium activity, in line with previous work noting that these cells come online during salience rather than just in a home cage (Adamsky et al, 2018) or a neutral, novel environment (Suthard & Senne et al, 2024).

To examine the structure of this astrocytic activity more rigorously, we performed cross-validation by computing the sorted activity for all cells during the 1$^{st}$ and 3$^{rd}$ foot shocks and compared this to the 2$^{nd}$ and 4$^{th}$ foot shocks during CFC for each animal. We

can then plot the 2nd and 4th foot shock heatmap sorted by the 1st and 3rd peak times to understand how this sequence is maintained across stimulus presentation. This method is essentially a non-parametric test of correlation of the peak times for the two halves of the data during the session. The advantage of comparing these pairs of foot shocks is that it accounts for systematic drift over time for time cells within session and should average out with this method (Mau et al, 2018). We observed maintained structure in this cross-validated heatmap for all animals, suggesting that what we are seeing is a reliable sequence (Figure 3C). To further validate this, we calculated the Spearman's correlation on the sorted peak times for the 1st and 3rd shocks vs. the 2nd and 4th shocks for each animal. We chose a Spearman's over a Pearson's correlation because we are assuming that the distribution of peak times across cells does not follow a normal distribution. In the Spearman's Correlation Test, rho is the correlation coefficient, which indicates the strength of the relationship between the two variables being tested (higher rho = stronger relationship) and the p-value being less than 0.05 indicates that we reject the null hypothesis that there is no relationship between the two variables. For our mice, the Spearman's tests indicated rho values between 0.3840 and 0.5585, as well as all p-values were near 0.000, suggesting that the sequences observed for the 1st and 3rd shocks vs. the 2nd and 4th have a strong relationship with one another. This observation of this time cell-like structure warranted further investigation into how these astrocytes may compare to their neuronal counterparts as it relates to temporal encoding.

*4.3.5) How does astrocytic sequential activity map onto spatial footprints?*

Astrocytes are unique in that they are connected with one another via gap junctions, enabling buffering of potassium and other ions throughout the syncytium, as well as propagation of calcium signaling throughout the network (Scemes & Spray, 2003). One major question is how this sequential activity may spatially map to the astrocytic network within dCA1. Does the sequence start in a small cluster of highly-active astrocytes and propagate outward in a biologically-relevant manner? Or is this activity more spread out and not as dependent on a spreading activity mechanism to derive the sequence? To investigate this, we plotted the first to last cell in the sequence for each animal as a progressing colormap for each shock (#1-4) and on average to understand visually how this might be happening. We qualitatively observe that the order of astrocytic firing is stable across foot shocks, with the dark red astrocytes displaying a peak location earlier than lighter pink astrocytes (**Figure 4**). However, also present are some cells that change their ordering within the sequence over shocks, potentially indicating a shared representation of time within the network of astrocytes rather than a concrete ordering that is due to the connectivity of the syncytium.

*4.3.6) Evidence of astrocytic sequences during memory recall*

We next set out to understand if these astrocytic sequences were also present during the Day 2 session of behavior, and if so, how they may be memory-specific in nature. To accomplish this, we first plotted sorted heatmaps for all astrocytes for the entire Day 2 session for both Cxt A and B groups to see if we could visually detect these sequences

(Figure 5A). Here, we observed very distinct differences across the two groups, with Cxt A mice displaying sequence-like bursts of activity at seemingly regular intervals across the session (Figure 5A). However, mice that were instead experiencing a novel, safe environment (Cxt B), there were no sequence-like bursts of activity and instead seemed to tile the entire session (Figure 5C). Since these sequences started around the timing of previous foot shocks (120, 180, 240, 300 seconds) on Day 1, we next plotted sorted heatmaps for all astrocytes at these intervals for Cxt A and B groups (Figure 5B, D). This was in line with our hypothesis that these sequences may appear at similar intervals during recall in Cxt A at stimulus-relevant intervals, such as the onset of shocks. Here, we observe that Cxt A mice display a similar hook-like sequence at the timing of previous foot shocks on Day 2 that we observed during the actual foot shocks on Day 1 (Figure 5B). On the other hand, Cxt B mice instead display a linear tiling of astrocytic activity when sorted, indicating a noisier process that appears unique from Cxt A (Figure 5D). We plan to further investigate how we can detect these sequences during Day 2 in an unbiased manner to compare their structure to those present on Day 1. Further, we will determine if these sequences are triggered by behaviorally-relevant states like freezing during Day 2 that may account for differences across the Cxt A and B groups, as they display different freezing levels.

*4.3.7) Reactivated astrocytes maintain temporal information during recall*

We next wondered if the astrocytic sequences present on Days 1 and 2 were composed of the same cells coming online in the same order. If the astrocyte sequences

that were present on Day 1 during CFC are not maintained across days in the same order, this is still interesting as the sequential information is maintained within the cell population in a different way. To address this question, we took the population of 'reactivated' astrocytes that were present on both days and plotted the Day 2 session based on their previous ordering on Day 1. When plotting the whole Day 2 session sorted on Day 1, we observed above-chance sequential information that was maintained within the Cxt A, but not Cxt B mice (Figure 6B, D). Further, when we analyzed the temporal epochs surrounding the previous timings of foot shock (120, 180, 240, 300 seconds) within these sorted heatmaps, we observed the same phenomenon (Figure 6A, C). These preliminary findings suggest that the astrocytes present in the Day 1 foot shock sequences are the same cells that are present in the Day 2 reactivated sequences in Cxt A, but not Cxt B, potentially pointing to some memory-specific process.

**4.4) Discussion**

Together, our preliminary findings pose that astrocytes may contribute to temporal processing during contextual fear memory acquisition and retrieval, opening the door to further exploration into the biological mechanisms behind this phenomenon. Here, we first show the feasibility of one-photon imaging of astrocytes in freely-moving mice and an ability to track these cells across days for analysis of reactivated astrocytes. This technique will allow for future experiments investigating freely-moving, single-cell recordings of astrocytes within natural environments, bolstering current work using head-fixed two-photon methods. Ideally, future work will utilize higher-resolution imaging modalities like

the Mini-2p (Zong et al, 2022) that will blend the benefits of our one-photon method with the spatial resolution of two-photon imaging to understand astrocytic functioning in more detail. Further, we replicate findings that astrocytes in the hippocampus are shock-responsive at the single-cell level, with almost all cells in the ROI active during one or more foot shocks. Next, we provide preliminary evidence that astrocyte sequences are triggered by foot shocks in dCA1 during contextual fear conditioning. Further, we observe that these sequences re-appear during recall in a memory-specific manner that we will continue to characterize. Finally, these recall sequences are maintained by a stable population of reactivated astrocytes in Cxt A, but not Cxt B mice. Overall, these preliminary findings lay the groundwork to understand how astrocytes may be involved in the spatiotemporal processing required for the formation and maintenance of contextual fear memory.

### *4.4.1) How might astrocytes and neurons differ in their temporal encoding?*

One major question is how these sequences in astrocytes may relate to what we already know about temporal encoding in neurons within the hippocampus during learning and memory tasks. Canonically, neuronal time cells span the entire trial or epoch during a behavioral task, but these astrocytes appear to terminate earlier than the subsequent foot shock (60 seconds later), suggesting some potential differences in their characteristics. Because these sequences terminate earlier, we wanted to understand why this may be happening and generated a few plausible hypotheses. First, hippocampal time cells are typically represented by a subpopulation of the total neurons (~30-50%), but we are not

filtering out any astrocytes by specific criteria which may contribute to ‘noisier’ sequences. Second, it is possible that astrocytes are inherently different than neurons in their responses and may encode temporal information in a novel manner than previously explained. This would make sense as neurons and astrocytes are likely not mirroring exact functional properties of one another, but instead are working together to form complex representations of the world. Finally, as our ROIs were determined manually, we were extremely conservative in labeling astrocytic somas and may have missed cell activity containing important temporal information. 1p data is also much poorer in SNR than 2p imaging methods, making it harder to detect lower levels of activity within astrocytes that may be smaller in amplitude or longer in duration. These cells would have activity ‘further out’ in time than their robustly-responding counterparts, and thus is a major limitation of this work. We hope that this work will allow us to understand how astrocytes may differ in their temporal coding from neurons, and inspire future work that examines these properties in higher resolution to overcome these limitations.

*4.4.2) Ongoing work*

Our ongoing work is systematically quantifying how these sequences in astrocytes may be similar to canonical neuronal time cells. Plotting the peak locations will allow us to assess the characteristics of these cell dynamics more quantitatively across all animals and at the individual animal level. If they are time cell-like, astrocyte peak locations would cover several seconds after foot shock, indicating true sequential activation. Further, the distribution of peak locations would not be uniformly distributed and instead skewed

towards smaller values closer to the stimulus onset. Further, to assess how these estimated peak locations fit within different distribution types, we will perform model-fitting. Classic time cells in the hippocampus fit within a Power-Law distribution (Cao et al, 2022), as they display logarithmic compression. We hypothesize that astrocyte peak times may fit best within an Exponential-Gaussian distribution, displaying some sequential pattern that is unique from neurons. Further, to understand how astrocytic sequences may drift across the session (Mau et al, 2018), we will calculate the cosine similarity between the first shock and subsequent shocks for each animal. We expect that we will observe a very high similarity between the astrocytic sequences at each shock, with a slight decrease across the session.

As we expect that astrocytic sequences will be unique from traditional neuronal time cells, we will next evaluate if these astrocytic sequences are more similar to neuronal time cells or temporal context cells. Time cells fire in sequence at a specific time after an event (i.e. trial onset) and maintain a record of the past. However, it is unknown if time cell-like dynamics are displayed even in neurons at the onset of a foot shock, nor if these sequences occur at the first instance of an event. On the other hand, temporal context cells (Bright et al, 2020) respond immediately when an animal enters a new environment and relax at different rates. These two cell types appear to encode temporal information differently, but time can be decoded better than chance for both systems. Using the characteristics of these two cell types, we will assess if these astrocytic sequences may be more similar to temporal context cells, time cells or if they fall somewhere in between. Time cells have a large range of mu (peak times) that are correlated with sigma (field

width), where cells that fire later in the sequence tend to have wider time fields or longer event duration. On the other hand, temporal context cells are independent of the mu distribution (peak times) and have a large range of tau (relaxation rate), as these cells peak around the same time but relax at different rates. We hypothesize that astrocyte sequences will display characteristics of both classic neuronal subpopulations, falling somewhere in between time and temporal context cells when evaluating their mu and sigma parameters.

For the recall session, we will continue to characterize these sequences using the same methods described above for the CFC activity. This information will allow us to understand how the Day 1 and 2 sequences are similar or unique across the Cxt A and B groups, lending evidence to the memory-specific nature of this process. We will further develop a method to automatically detect these 'replay-like' sequences during recall to understand the total number of sequences across the Day 2 session in Cxt A and B groups. Further, as mentioned previously, we will correlate these recall sequences with freezing and other meaningful behavioral epochs to understand the relevance to memory recall.

**4.5) Author Contributions**

List of authors (in no particular order, as analysis is ongoing): Rebecca L. Suthard (R.L.S), Ryan A. Senne (R.A.S), Rui Cao (R.C.), Amy H. Monasterio (A.H.M.), Evan A. Ruesch (E.A.R.), Michelle D. Buzharsky (M.D.B.), Marc W. Howard (M.W.H.), Steve Ramirez (S.R.).

## 4.6) Figures

### Figure 4.1

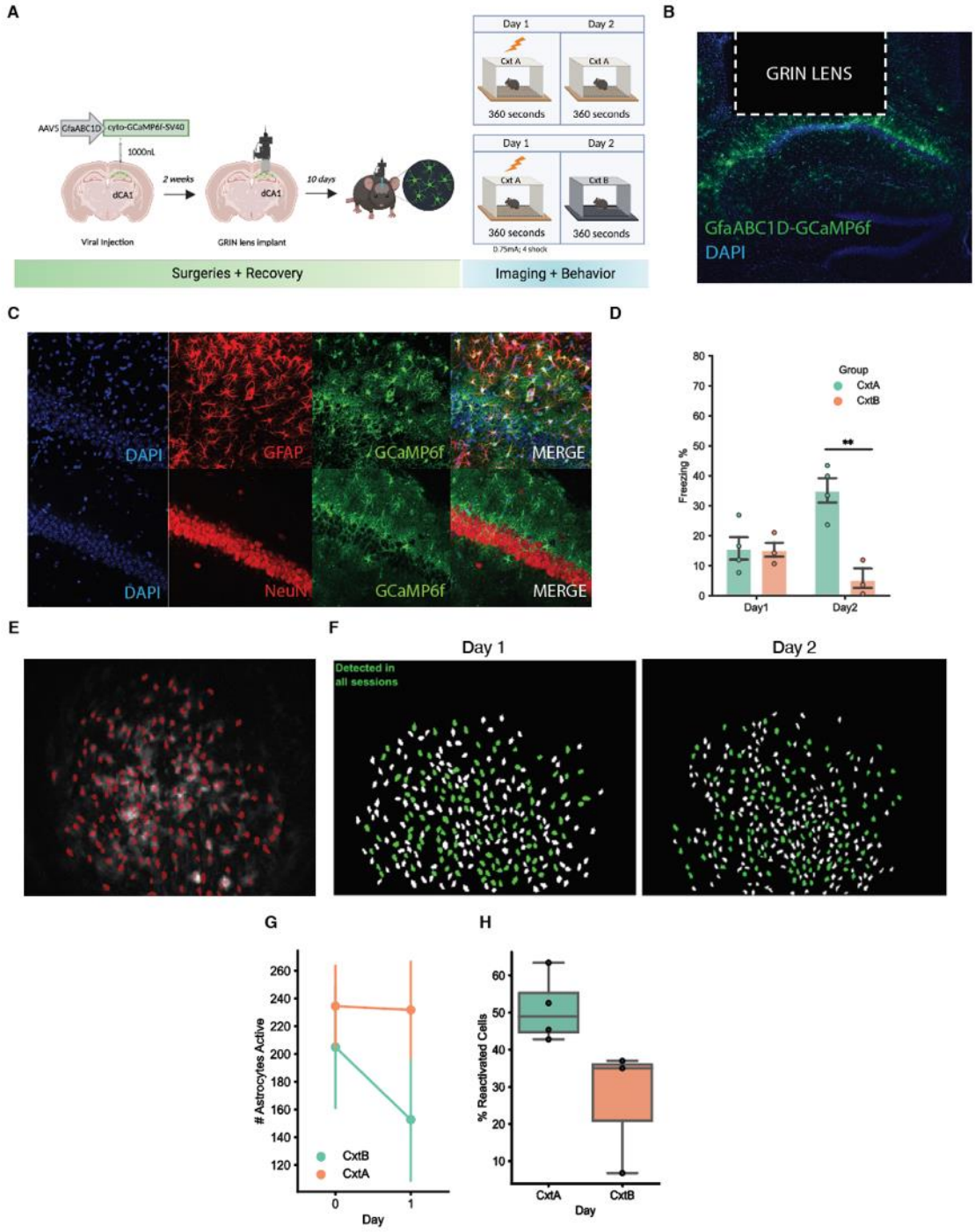

**Figure 4.1: One-photon imaging of astrocytes in dorsal hippocampus across contextual fear learning and recall. (A)** Astrocyte one-photon (1p) recordings in dorsal CA1 (dCA1) of the hippocampus. Wild type C57BL/6J mice were injected with 1000nl of the astrocyte-specific genetically-encoded calcium indicator, AAV5-GfaABC1D-cyto-GCaMP6f-SV40, into dCA1 and allowed two weeks for recovery before implantation of a gradient-index (GRIN) lens above the pyramidal cell layer. After 10 days of post-surgical recovery, mice were imaged using the nVista System (Inscopix, Inc.). On Day 1, all mice (n=7) underwent contextual fear conditioning (CFC) for 330 seconds in Context A (Cxt A), where they received four foot shocks (0.75mA, 2s duration) at the 120, 180, 240 and 300 second time points. On Day 2, mice underwent a 330 second contextual recall session in the same mouse conditioning chamber (Cxt A) or were instead exposed to a novel Context B (Cxt B) for the same duration of time as a memory-specific control. **(B)** Representative 20x confocal microscopy image of the dCA1 pyramidal cell layer expression of GfaABC1D-GCaMP6f (green; astrocytes) and DAPI (blue; nuclei) with an approximate location of the GRIN lens implantation. **(C)** Representative 20x confocal microscopy images of the dCA1 pyramidal cell layer visualizing DAPI+ cells (blue; nuclei), GfaABC1D-GCaMP6f (green; viral expression), glial fibrillary acidic protein (GFAP)(red; astrocytes) or NeuN (red; neurons) to ensure selective expression of our virus in astrocytes. **(D)** Average % freezing for Day 1 (CFC) and Day 2 (recall/novel exposure) across Cxt A and B groups. **(E)** Representative regions-of-interest (ROIs) map shows all astrocytes active during CFC from a mouse that were detected using manual ROI selection and curation. **(F)** CellReg output that shows a representative set of tracked astrocytes across

Days 1-2, where green ROIs are detected across both sessions. **(G)** Number of astrocytes active on Days 1-2 across Cxt A and B groups. **(H)** Percentage of 'reactivated' astrocytes (# reactivated astrocytes during Day 2/total # astrocytes during Day 1) across Cxt A and B groups. For 1D and 1G, Two-way RM ANOVA was performed with Sidak's multiple comparisons test (post-hoc) where applicable. For 1H, an Independent t-test was performed. Significance was indicated by: *$p \leq 0.05$, **$p \leq 0.01$, ***$p \leq 0.001$, ****$p \leq 0.0001$. Error bars in all plots indicate mean ± SEM. All data was tested for normality and no outliers were removed. Cxt A (n = 4) and Cxt B (n = 3).

**Figure 4.2**

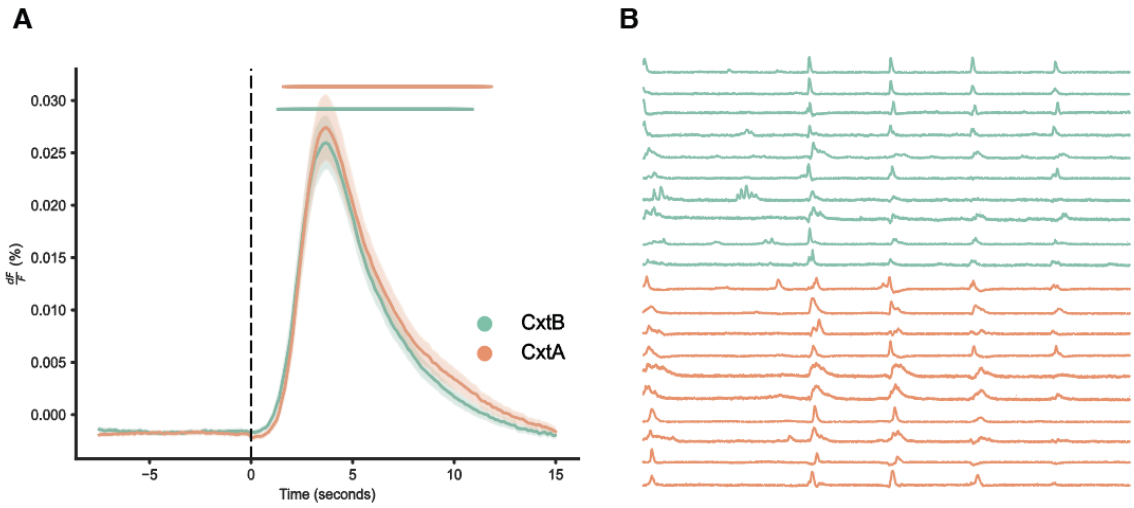


**Figure 4.2: Astrocytes are shock-responsive during contextual fear conditioning. (A)** Peri-event analysis for astrocytes in Cxt A (orange) and Cxt B (green) indicate increased activity (% dF/F) at the times of 0.75mA foot shocks (dashed line; 120, 180, 240, 300 seconds averaged). For peri-event analysis, we used a 95% t-confidence interval (tCI) (shaded region) approach where a "significant" event, indicated by the colored bars above the average time series (solid lines), represents any time period greater than 1 second where the tCI did not include the median-shifted baseline of 0. **(B)** Representative calcium time series for Cxt A and B groups showing almost all astrocytes display a robust response to one or more shocks during the CFC session. In Figure 2A, shock-response is averaged for each group with Cxt A (n = 4) and Cxt B (n = 3).

**Figure 4.3**

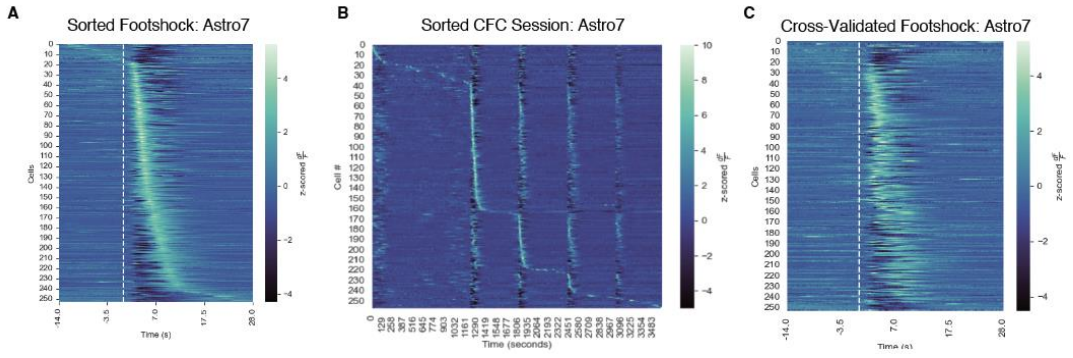


**Figure 4.3: Evidence of astrocytic temporal sequences after foot shock onset. (A)** Representative heatmap showing the average calcium response for all astrocytes (n = 250), for a single animal (Astro7) at the timing of foot shock (dashed white line; 120, 180, 240, 300 seconds) sorted by their maximal z-scored response. We observed a hook-like structure that spans from the timing of foot shock (time = 0) to approximately 28 seconds after. **(B)** Representative heatmap showing the same information above for all astrocytes across the entire Day 1 contextual fear conditioning (CFC) session, with sequential activity appearing at each foot shock. (C) Representative cross-validated heatmap for the same mouse (Astro7) across all cells (n = 250 astrocytes). We computed the average 2$^{nd}$ and 4$^{th}$ foot shock activity and sorted this information by the 1$^{st}$ and 3$^{rd}$ peak times for each animal to understand how this sequence is maintained across stimulus presentation. We observed maintained structure in these cross-validated heatmaps for all animals, suggesting a reliable sequence during CFC.

**Figure 4.4**

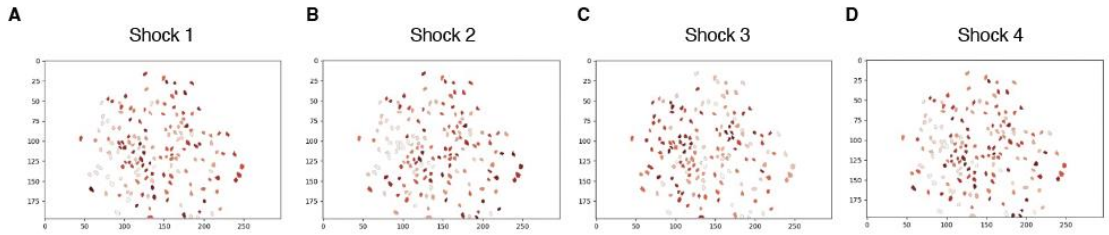


**Figure 4.4: How does astrocytic sequential activity map onto spatial footprints?** Representative spatial region-of-interest (ROI) maps for a single mouse as they underwent each foot shock (A-D). Each ROI was plotted with the first to last astrocyte in the foot shock-induced sequence as a progressing colormap for each shock, with the dark red cells displaying peak locations earlier than the lighter pink astrocytes. We observe relatively stable spatial representation of the astrocytic sequences across all animals, with some cells changing their ordering within the sequence over shocks.

**Figure 4.5**

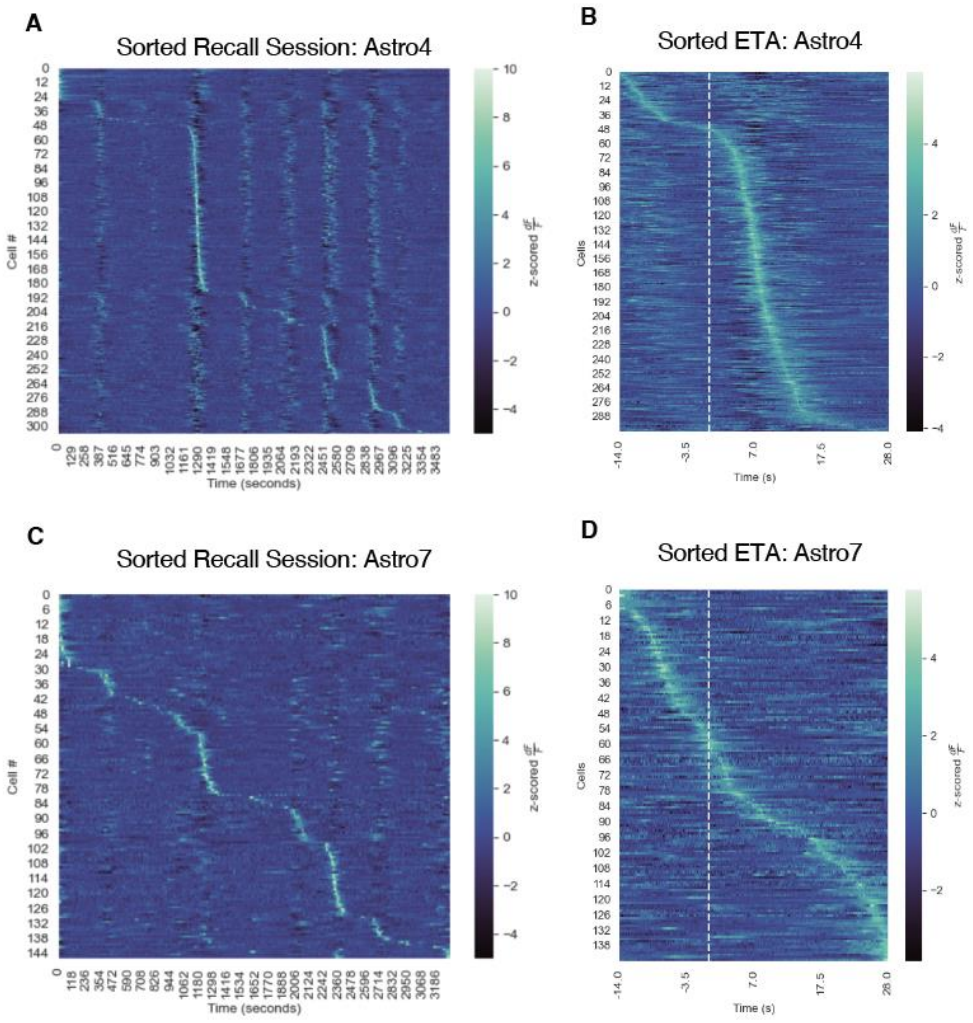


**Figure 4.5: Evidence of astrocytic sequences during memory recall. (A)** Representative heatmap showing the average calcium response for all astrocytes (n = 288), for a single animal (Astro4; Cxt A) sorted by their maximal z-scored response across the entire Day 2 recall session. **(B)** Representative heatmap showing the same information above for all Astro4 astrocytes at the timing of previous foot shocks (dashed line; 120, 180, 240, 300 seconds) during recall. **(C)** Representative heatmap showing the average calcium response

for all astrocytes (n = 144), for a single animal (Astro7; Cxt B) sorted by their maximal z-scored response across the entire Day 2 novel exposure session. **(D)** Representative heatmap showing the same information above for all Astro7 astrocytes at the timing of previous foot shocks (dashed line; 120, 180, 240, 300 seconds) during Cxt B exposure. Together, we observed sequence-like bursts of activity at regular intervals throughout the session in Cxt A, but not Cxt B mice **(A, C)**. Cxt A, but not Cxt B mice displayed similar hook-like sequences at the timing of previous foot shock on Day 2 that we observed during the actual foot shocks on Day 1.

**Figure 4.6**

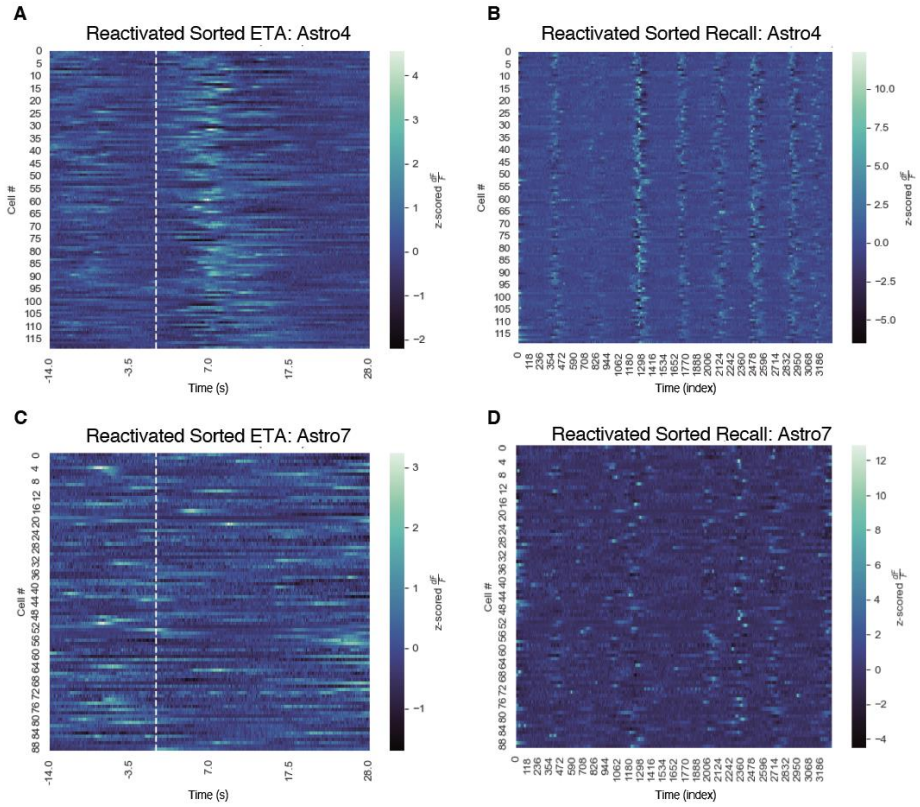


**Figure 4.6: Reactivated astrocytes maintain temporal information during recall. (A-B)** Representative heatmap showing the average calcium response for all reactivated astrocytes (n = 115), for a single animal (Astro4; Cxt A) sorted by their maximal z-scored response at the timing of previous foot shocks (dashed line; 120, 180, 240, 300 seconds) during recall (A) and for the entire recall session (B). **(C-D)** Representative heatmap showing the average calcium response for all reactivated astrocytes (n = 88), for a single animal (Astro7; Cxt B) sorted by their maximal z-scored response at the timing of previous foot shocks (dashed line; 120, 180, 240, 300 seconds) during novel context exposure (C)

and for the entire session (D). Together, we observed above-chance sequential information that was maintained within Cxt A but not Cxt B mice.

## BIBLIOGRAPHY

Adamsky, A., Kol, A., Kreisel, T., Doron, A., Ozeri-Engelhard, N., Melcer, T., Refaeli, R., Horn, H., Regev, L., Groysman, M., London, M., & Goshen, I. (2018a). Astrocytic Activation Generates De Novo Neuronal Potentiation and Memory Enhancement. Cell, 174(1), 59-71.e14.

Adamsky, A., & Goshen, I. (2018b). Astrocytes in Memory Function: Pioneering Findings and Future Directions. Neuroscience, 370, 14–26.

Adolphs, R., Tranel, D., Damasio, H., & Damasio, A. R. (1995). Fear and the human amygdala. The Journal of neuroscience: the official journal of the Society for Neuroscience, 15(9), 5879–5891.

Agulhon C, Petravicz J, McMullen AB, Sweger EJ, Minton SK, Taves SR, Casper KB, Fiacco TA, McCarthy KD (2008) What is the role of astrocyte calcium in neurophysiology? Neuron, 59:932–946.

Agulhon, C., Fiacco, T. A., & McCarthy, K. D. (2010). Hippocampal short- and long-term plasticity are not modulated by astrocyte Ca2+ signaling. Science, 327(5970), 1250–1254.

Airan, R. D., Thompson, K. R., Fenno, L. E., Bernstein, H., & Deisseroth, K. (2009). Temporally precise in vivo control of intracellular signalling. Nature, 458(7241), 1025–1029.

Akther, S., & Hirase, H. (2022). Assessment of astrocytes as a mediator of memory and learning in rodents. Glia, 70(8), 1484–1505.

Alberini, C. M., Cruz, E., Descalzi, G., Bessières, B., & Gao, V. (2018). Astrocyte glycogen and lactate: new insights into learning and memory mechanisms. Glia, 66(6), 1244.

Amaral, D. G., & Witter, M. P. (1989). The three-dimensional organization of the hippocampal formation: a review of anatomical data. Neuroscience, 31(3), 571–591.

Anagnostaras, S. G., Maren, S., & Fanselow, M. S. (1999). Temporally graded retrograde amnesia of contextual fear after hippocampal damage in rats: within-subjects examination. The Journal of neuroscience: the official journal of the Society for Neuroscience, 19(3), 1106–1114.

Araque, A., Parpura, V., Sanzgiri, R. P., & Haydon, P. G. (1999). Tripartite synapses: Glia, the unacknowledged partner. Trends in Neurosciences, 22(5), 208–215.

Araque, A., Carmignoto, G., & Haydon, P. G. (2001). Dynamic signaling between astrocytes and neurons. Annual Review of Physiology, 63, 795–813.

Araque, A., Carmignoto, G., Haydon, P. G., Oliet, S. H. R., Robitaille, R., & Volterra, A. (2014). Gliotransmitters travel in time and space. Neuron, 81(4), 728–739.

Armbruster, B. N., Li, X., Pausch, M. H., Herlitze, S., & Roth, B. L. (2007). Evolving the lock to fit the key to create a family of G protein-coupled receptors potently activated by an inert ligand. Proceedings of the National Academy of Sciences of the United States of America, 104(12), 5163–5168.

Armbruster, M., Naskar, S., Garcia, J. P., Sommer, M., Kim, E., Adam, Y., Haydon, P. G., Boyden, E. S., Cohen, A. E., & Dulla, C. G. (2022). Neuronal activity drives pathway-specific depolarization of peripheral astrocyte processes. Nature neuroscience, 25(5), 607–616.

Bannerman, D. M., Yee, B. K., Good, M. A., Heupel, M. J., Iversen, S. D., & Rawlins, J. N. (1999). Double dissociation of function within the hippocampus: a comparison of dorsal, ventral, and complete hippocampal cytotoxic lesions. Behavioral neuroscience, 113(6), 1170–1188.

Bannerman, D. M., Deacon, R. M., Offen, S., Friswell, J., Grubb, M., & Rawlins, J. N. (2002). Double dissociation of function within the hippocampus: spatial memory and hyponeophagia. Behavioral neuroscience, 116(5), 884–901.

Batiuk, M. Y., Martirosyan, A., Wahis, J., de Vin, F., Marneffe, C., Kusserow, C., Koeppen, J., Viana, J. F., Oliveira, J. F., Voet, T., Ponting, C. P., Belgard, T. G., & Holt, M. G. (2020). Identification of region-specific astrocyte subtypes at single cell resolution. Nature communications, 11(1), 1220.

Bayley, P. J., Gold, J. J., Hopkins, R. O., & Squire, L. R. (2005). The neuroanatomy of remote memory. Neuron, 46(5), 799–810.

Bazargani, N., & Attwell, D. (2016). Astrocyte calcium signaling: the third wave. Nature neuroscience, 19(2), 182–189.

Bechara, A., Tranel, D., Damasio, H., Adolphs, R., Rockland, C., & Damasio, A. R. (1995). Double dissociation of conditioning and declarative knowledge relative to the amygdala and hippocampus in humans. Science, 269(5227), 1115–1118.

Berg, S., Kutra, D., Kroeger, T., Straehle, C. N., Kausler, B. X., Haubold, C., Schiegg, M., Ales, J., Beier, T., Rudy, M., Eren, K., Cervantes, J. I., Xu, B., Beuttenmueller, F., Wolny, A., Zhang, C., Koethe, U., Hamprecht, F. A., & Kreshuk, A. (2019). Ilastik: interactive machine learning for (bio)image analysis. Nature methods, 16(12), 1226–1232.

Bezzi, P., & Volterra, A. (2001). A neuron-glia signaling network in the active brain. Current Opinion in Neurobiology, 11(3), 387–394.

Blanchard, D. C., & Blanchard, R. J. (1972). Innate and conditioned reactions to threat in rats with amygdaloid lesions. Journal of Comparative and Physiological Psychology, 81(2), 281–290.

Bliss, T. V., & Lomo, T. (1973). Long-lasting potentiation of synaptic transmission in the dentate area of the anaesthetized rabbit following stimulation of the perforant path. The Journal of physiology, 232(2), 331–356.

Boyden, E. S., Zhang, F., Bamberg, E., Nagel, G., & Deisseroth, K. (2005). Millisecond-timescale, genetically targeted optical control of neural activity. Nature neuroscience, 8(9), 1263–1268.

Bright, I. M., Meister, M. L. R., Cruzado, N. A., Tiganj, Z., Buffalo, E. A., & Howard, M. W. (2020). A temporal record of the past with a spectrum of time constants in the monkey entorhinal cortex. Proceedings of the National Academy of Sciences of the United States of America, 117(33), 20274–20283.

Burwell, R. D., & Amaral, D. G. (1998). Cortical afferents of the perirhinal, postrhinal, and entorhinal cortices of the rat. The Journal of comparative neurology, 398(2), 179–205.

Calder, A. J., Young, A. W., Rowland, D., Perrett, D. I., Hodges, J. R., & Etcoff, N. L. (1996). Facial emotion recognition after bilateral amygdala damage: Differentially severe impairment of fear. Cognitive Neuropsychology, 13(5), 699–745.

Campeau, S., & Davis, M. (1995). Involvement of the central nucleus and basolateral complex of the amygdala in fear conditioning measured with fear-potentiated startle in rats trained concurrently with auditory and visual conditioned stimuli. The Journal of neuroscience: the official journal of the Society for Neuroscience, 15(3 Pt 2), 2301–2311.

Cao, R., Bladon, J. H., Charczynski, S. J., Hasselmo, M. E., & Howard, M. W. (2022). Internally generated time in the rodent hippocampus is logarithmically compressed. eLife, 11, e75353.

Cembrowski, M. S., Wang, L., Sugino, K., Shields, B. C., & Spruston, N. (2016). Hipposeq: a comprehensive RNA-seq database of gene expression in hippocampal principal neurons. eLife, 5, e14997.

Chen, B. K., Murawski, N. J., Cincotta, C., McKissick, O., Finkelstein, A., Hamidi, A. B., Merfeld, E., Doucette, E., Grella, S. L., Shpokayte, M., Zaki, Y., Fortin, A., & Ramirez, S. (2019). Artificially Enhancing and Suppressing Hippocampus-Mediated Memories. Current biology: CB, 29(11), 1885–1894.e4.

Cho, W.H., Noh, K., Lee, B.H., Barcelon, E., Jun, S.B., Park, H.Y., Lee, S.J. (2022). Hippocampal astrocytes modulate anxiety-like behavior. Nature Communications, 13:1 13, 1–14.

Ciocchi, S., Passecker, J., Malagon-Vina, H., Mikus, N., and Klausberger, T. (2015). Brain computation. Selective information routing by ventral hippocampal CA1 projection neurons. Science, 348, 560–563. 10.1126/science.aaa3245.

Collingridge, G. L., Kehl, S. J., & McLennan, H. (1983). Excitatory amino acids in synaptic transmission in the Schaffer collateral-commissural pathway of the rat hippocampus. The Journal of physiology, 334, 33–46.

Corcoran, K. A., & Quirk, G. J. (2007). Activity in prelimbic cortex is necessary for the expression of learned, but not innate, fears. The Journal of neuroscience : the official journal of the Society for Neuroscience, 27(4), 840–844.

Corkrum, M., Covelo, A., Lines, J., Bellocchio, L., Pisansky, M., Loke, K., Quintana, R., Rothwell, P. E., Lujan, R., Marsicano, G., Martin, E. D., Thomas, M. J., Kofuji, P., & Araque, A. (2020). Dopamine-Evoked Synaptic Regulation in the Nucleus Accumbens Requires Astrocyte Activity. Neuron, 105(6), 1036.

Covelo, A., and Araque, A. (2018). Neuronal activity determines distinct gliotransmitter release from a single astrocyte. ELife, 7. 10.7554/eLife.32237.

Croft, W., Reusch, K., Tilunaite, A., Russell, N. A., Thul, R., & Bellamy, T. C. (2016). Probabilistic encoding of stimulus strength in astrocyte global calcium signals. Glia, 64(4), 537–552.

Cui, G., Jun, S. B., Jin, X., Luo, G., Pham, M. D., Lovinger, D. M., Vogel, S. S., & Costa, R. M. (2014). Deep brain optical measurements of cell type–specific neural activity in behaving mice. Nature Protocols, 9(6), 1213.

Curreli, S., Bonato, J., Romanzi, S., Panzeri, S., & Fellin, T. (2022). Complementary encoding of spatial information in hippocampal astrocytes. PLoS biology, 20(3), e3001530.

Dana, H., Mohar, B., Sun, Y., Narayan, S., Gordus, A., Hasseman, J.P., Tsegaye, G., Holt, G.T., Hu, A., Walpita, D., et al. (2016). Sensitive red protein calcium indicators for imaging neural activity. ELife, 5. 10.7554/eLife.12727.

Davis, M. (1992). The role of the amygdala in conditioned fear. In J. P. Aggleton (Ed.), The amygdala: Neurobiological aspects of emotion, memory, and mental dysfunction (pp. 255–306). Wiley-Liss.

Davis, M., & Whalen, P. J. (2001). The amygdala: vigilance and emotion. Molecular psychiatry, 6(1), 13–34.

DeNardo, L. A., Liu, C. D., Allen, W. E., Adams, E. L., Friedmann, D., Fu, L., Guenthner, C. J., Tessier-Lavigne, M., & Luo, L. (2019). Temporal evolution of cortical ensembles promoting remote memory retrieval. Nature neuroscience, 22(3), 460–469.

Denny, C.A., Kheirbek, M.A., Alba, E.L., Tanaka, K.F., Brachman, R.A., Laughman, K.B., Tomm, N.K., Turi, G.F., Losonczy, A., and Hen, R. (2014). Hippocampal memory traces are differentially modulated by experience, time, and adult neurogenesis. Neuron, 83, 189–201. 10.1016/j.neuron.2014.05.018.

di Castro, M. A., Chuquet, J., Liaudet, N., Bhaukaurally, K., Santello, M., Bouvier, D., Tiret, P., & Volterra, A. (2011). Local Ca2+ detection and modulation of synaptic release by astrocytes. Nature Neuroscience, 14(10), 1276–1284.

Dong, H. W., Swanson, L. W., Chen, L., Fanselow, M. S., & Toga, A. W. (2009). Genomic-anatomic evidence for distinct functional domains in hippocampal field CA1. Proceedings of the National Academy of Sciences of the United States of America, 106(28), 11794–11799.

Doron, A., Rubin, A., Benmelech-Chovav, A., Benaim, N., Carmi, T., Refaeli, R., Novick, N., Kreisel, T., Ziv, Y., & Goshen, I. (2022). Hippocampal astrocytes encode reward location. Nature, 609(7928), 772–778.

Durkee, C. A., Covelo, A., Lines, J., Kofuji, P., Aguilar, J., & Araque, A. (2019). Gi/o protein-coupled receptors inhibit neurons but activate astrocytes and stimulate gliotransmission. Glia, 67(6), 1076–1093.

Eichenbaum H. (2014). Time cells in the hippocampus: a new dimension for mapping memories. Nature reviews. Neuroscience, 15(11), 732–744.

Eichenbaum H. (2004). Hippocampus: cognitive processes and neural representations that underlie declarative memory. Neuron, 44(1), 109–120.

Eichenbaum, H., & Cohen, N. J. (2001). From conditioning to conscious recollection: Memory systems of the brain. Oxford University Press.

Eichenbaum, H. (2000). A cortical-hippocampal system for declarative memory. Nature reviews neuroscience, 1, 41–50. 10.1038/35036213.

Eichenbaum, H., Schoenbaum, G., Young, B., & Bunsey, M. (1996). Functional organization of the hippocampal memory system. Proceedings of the National Academy of Sciences of the United States of America, 93(24), 13500–13507.

Eichenbaum, H., & Buckingham, J. (1990). Studies on hippocampal processing: Experiment, theory, and model. In M. Gabriel & J. Moore (Eds.), Learning and computational neuroscience: Foundations of adaptive networks (pp. 171–231). The MIT Press.

Fan, X. C., Ma, C. N., Song, J. C., Liao, Z. H., Huang, N., Liu, X., & Ma, L. (2021). Rac1 Signaling in Amygdala Astrocytes Regulates Fear Memory Acquisition and Retrieval. Neuroscience Bulletin, 37(7), 947.

Fanselow, M.S., and Dong, H.-W. (2010). Are the dorsal and ventral hippocampus functionally distinct structures? Neuron, 65, 7–19. 10.1016/j.neuron.2009.11.031.

Fedotova, A., Brazhe, A., Doronin, M., Toptunov, D., Pryazhnikov, E., Khiroug, L., Verkhratsky, A., & Semyanov, A. (2023). Dissociation Between Neuronal and Astrocytic Calcium Activity in Response to Locomotion in Mice. Function, 4(4), zqad019.

Felix-Ortiz, A. C., & Tye, K. M. (2014). Amygdala inputs to the ventral hippocampus bidirectionally modulate social behavior. The Journal of neuroscience: the official journal of the Society for Neuroscience, 34(2), 586–595.

Fellin, T., Pascual, O., Gobbo, S., Pozzan, T., Haydon, P. G., & Carmignoto, G. (2004). Neuronal synchrony mediated by astrocytic glutamate through activation of extrasynaptic NMDA receptors. Neuron, 43(5), 729–743.

Ferbinteanu, J., & McDonald, R. J. (2001). Dorsal/ventral hippocampus, fornix, and conditioned place preference. Hippocampus, 11(2), 187–200.

Figueiredo, M., Lane, S., Stout, R. F., Jr, Liu, B., Parpura, V., Teschemacher, A. G., & Kasparov, S. (2014). Comparative analysis of optogenetic actuators in cultured astrocytes. Cell calcium, 56(3), 208–214

Flavell, S. W., & Greenberg, M. E. (2008). Signaling mechanisms linking neuronal activity to gene expression and plasticity of the nervous system. Annual review of neuroscience, 31, 563–590.

Gao, V., Suzuki, A., Magistretti, P. J., Lengacher, S., Pollonini, G., Steinman, M. Q., & Alberini, C. M. (2016). Astrocytic β2- Adrenergic receptors mediate hippocampal long- Term memory consolidation. Proceedings of the National Academy of Sciences of the United States of America, 113(30), 8526–8531.

Gergues, M. M., Han, K. J., Choi, H. S., Brown, B., Clausing, K. J., Turner, V. S., Vainchtein, I. D., Molofsky, A. V., & Kheirbek, M. A. (2020). Circuit and molecular architecture of a ventral hippocampal network. Nature neuroscience, 23(11), 1444–1452.

Giaume, C., Koulakoff, A., Roux, L., Holcman, D., & Rouach, N. (2010). Astroglial networks: a step further in neuroglial and gliovascular interactions. Nature reviews neuroscience, 11(2), 87–99.

Goenaga, J., Araque, A., Kofuji, P., & Herrera Moro Chao, D. (2023). Calcium signaling in astrocytes and gliotransmitter release. Frontiers in synaptic neuroscience, 15, 1138577.

González-Arias, C., Sánchez-Ruiz, A., Esparza, J., Sánchez-Puelles, C., Arancibia, L., Ramírez-Franco, J., Gobbo, D., Kirchhoff, F., & Perea, G. (2023). Dysfunctional serotonergic neuron-astrocyte signaling in depressive-like states. Molecular psychiatry, 28(9), 3856–3873.

Goosens, K. A., Hobin, J. A., & Maren, S. (2003). Auditory-evoked spike firing in the lateral amygdala and Pavlovian fear conditioning: mnemonic code or fear bias?. Neuron, 40(5), 1013–1022.

Goosens, K. A., & Maren, S. (2004). NMDA receptors are essential for the acquisition, but not expression, of conditional fear and associative spike firing in the lateral amygdala. The European journal of neuroscience, 20(2), 537–548.

Gore, F., Schwartz, E. C., Brangers, B. C., Aladi, S., Stujenske, J. M., Likhtik, E., Russo, M. J., Gordon, J. A., Salzman, C. D., & Axel, R. (2015). Neural Representations of Unconditioned Stimuli in Basolateral Amygdala Mediate Innate and Learned Responses. Cell, 162(1), 134–145.

Greenberg, M. E., & Ziff, E. B. (1984). Stimulation of 3T3 cells induces transcription of the c-fos proto-oncogene. Nature, 311(5985), 433–438.

Grella SL, Fortin AH, McKissick O, Leblanc H, Ramirez S (2020) Odor modulates the temporal dynamics of fear memory consolidation. Learning and memory, 27:150–163.

Guenthner, C. J., Miyamichi, K., Yang, H. H., Heller, H. C., & Luo, L. (2013). Permanent genetic access to transiently active neurons via TRAP: targeted recombination in active populations. Neuron, 78(5), 773–784.

Gunaydin, L. A., Grosenick, L., Finkelstein, J. C., Kauvar, I. v., Fenno, L. E., Adhikari, A., Lammel, S., Mirzabekov, J. J., Airan, R. D., Zalocusky, K. A., Tye, K. M., Anikeeva, P., Malenka, R. C., & Deisseroth, K. (2014). Natural neural projection dynamics underlying social behavior. Cell, 157(7), 1535.

Guzowski, J. F., McNaughton, B. L., Barnes, C. A., & Worley, P. F. (1999). Environment-specific expression of the immediate-early gene Arc in hippocampal neuronal ensembles. Nature neuroscience, 2(12), 1120–1124.

Guzowski, J. F., Setlow, B., Wagner, E. K., & McGaugh, J. L. (2001). Experience-dependent gene expression in the rat hippocampus after spatial learning: a comparison of the immediate-early genes Arc, c-fos, and zif268. The Journal of neuroscience: the official journal of the Society for Neuroscience, 21(14), 5089–5098.

Han, J. H., Kushner, S. A., Yiu, A. P., Cole, C. J., Matynia, A., Brown, R. A., Neve, R. L., Guzowski, J. F., Silva, A. J., & Josselyn, S. A. (2007). Neuronal competition and selection during memory formation. Science, 316(5823), 457–460.

Han, J. H., Yiu, A. P., Cole, C. J., Hsiang, H. L., Neve, R. L., & Josselyn, S. A. (2008). Increasing CREB in the auditory thalamus enhances memory and generalization of auditory conditioned fear. Learning & memory, 15(6), 443–453.

Han, J. H., Kushner, S. A., Yiu, A. P., Hsiang, H. L., Buch, T., Waisman, A., Bontempi, B., Neve, R. L., Frankland, P. W., & Josselyn, S. A. (2009). Selective erasure of a fear memory. Science, 323(5920), 1492–1496.

Hasan, M., Lei, Z., Akter, M., Iqbal, Z., Usaila, F., Ramkrishnan, A. S., & Li, Y. (2022). Chemogenetic activation of astrocytes promotes remyelination and restores cognitive deficits in visceral hypersensitive rats. iScience, 26(1), 105840.

Haustein, M.D., Kracun, S., Lu, X.-H., Shih, T., Jackson-Weaver, O., Tong, X., Xu, J., Yang, X.W., O'Dell, T.J., Marvin, J.S., et al. (2014). Conditions and constraints for astrocyte calcium signaling in the hippocampal mossy fiber pathway. Neuron 82, 413–429. 10.1016/j.neuron.2014.02.041.

Haydon, P. G. (2001). Glia: listening and talking to the synapse. Nature reviews neuroscience 2001 2:3, 2(3), 185–193.

Hebb, D. O., & Penfield, W. (1940). Human behavior after extensive bilateral removal from the frontal lobes. Archives of neurology & psychiatry, 43, 421–438.

Hebb, D. O. (1949). The Organisation of Behaviour. New York, NY: John Wiley & Sons.

Henke P. G. (1990). Hippocampal pathway to the amygdala and stress ulcer development. Brain research bulletin, 25(5), 691–695.

Henneberger, C., Bard, L., Panatier, A., Reynolds, J. P., Kopach, O., Medvedev, N. I., Minge, D., Herde, M. K., Anders, S., Kraev, I., Heller, J. P., Rama, S., Zheng, K., Jensen, T. P., Sanchez-Romero, I., Jackson, C. J., Janovjak, H., Ottersen, O. P., Nagelhus, E. A., Oliet, S. H. R., … Rusakov, D. A. (2020). LTP Induction Boosts Glutamate Spillover by Driving Withdrawal of Perisynaptic Astroglia. Neuron, 108(5), 919–936.e11.

Herry, C., Ciocchi, S., Senn, V., Demmou, L., Müller, C., & Lüthi, A. (2008). Switching on and off fear by distinct neuronal circuits. Nature, 454(7204), 600–606

Herry, C., Ferraguti, F., Singewald, N., Letzkus, J. J., Ehrlich, I., & Lüthi, A. (2010). Neuronal circuits of fear extinction. The European journal of neuroscience, 31(4), 599–612.

Howe, M., Ridouh, I., Mascaro, A. L. A., Larios, A., Azcorra, M., & Dombeck, D. A. (2019). Coordination of rapid cholinergic and dopaminergic signaling in striatum during spontaneous movement. ELife, 8.

Hsiang, H. L., Epp, J. R., van den Oever, M. C., Yan, C., Rashid, A. J., Insel, N., Ye, L., Niibori, Y., Deisseroth, K., Frankland, P. W., & Josselyn, S. A. (2014).

Manipulating a "cocaine engram" in mice. The Journal of neuroscience: the official journal of the Society for Neuroscience, 34(42), 14115–14127.

Ingiosi, A.M., Hayworth, C.R., Harvey, D.O., Singletary, K.G., Rempe, M.J., Wisor, J.P., and Frank, M.G. (2020). A Role for Astroglial Calcium in Mammalian Sleep and Sleep Regulation. Current biology, 30, 4373–4383.e7. 10.1016/j.cub.2020.08.052.

Janak, P. H., & Tye, K. M. (2015). From circuits to behaviour in the amygdala. Nature, 517(7534), 284–292.

Jarvis, E. D., Güntürkün, O., Bruce, L., Csillag, A., Karten, H., Kuenzel, W., Medina, L., Paxinos, G., Perkel, D. J., Shimizu, T., Striedter, G., Wild, J. M., Ball, G. F., Dugas-Ford, J., Durand, S. E., Hough, G. E., Husband, S., Kubikova, L., Lee, D. W., Mello, C. V., … Avian Brain Nomenclature Consortium (2005). Avian brains and a new understanding of vertebrate brain evolution. Nature reviews neuroscience, 6(2), 151–159.

Jean-Richard-dit-Bressel, P., Clifford, C. W. G., & McNally, G. P. (2020). Analyzing Event-Related Transients: Confidence Intervals, Permutation Tests, and Consecutive Thresholds. Frontiers in molecular neuroscience, 13, 14.

Jimenez, J. C., Berry, J. E., Lim, S. C., Ong, S. K., Kheirbek, M. A., & Hen, R. (2020). Contextual fear memory retrieval by correlated ensembles of ventral CA1 neurons. Nature communications, 11(1).

Johansen, J. P., Tarpley, J. W., LeDoux, J. E., & Blair, H. T. (2010). Neural substrates for expectation-modulated fear learning in the amygdala and periaqueductal gray. Nature neuroscience, 13(8), 979–986.

Josselyn S. A. (2010). Continuing the search for the engram: examining the mechanism of fear memories. Journal of psychiatry & neuroscience : JPN, 35(4), 221–228.

Josselyn, S. A., Köhler, S., & Frankland, P. W. (2017). Heroes of the Engram. The Journal of neuroscience: the official journal of the Society for Neuroscience, 37(18), 4647–4657.

Jung, M. W., Wiener, S. I., & McNaughton, B. L. (1994). Comparison of spatial firing characteristics of units in dorsal and ventral hippocampus of the rat. The Journal of neuroscience: the official journal of the Society for Neuroscience, 14(12), 7347–7356.

Kalman, R.E. (1960). A New Approach to Linear Filtering and Prediction Problems. J. Basic Eng, 82, 35–45. 10.1115/1.3662552.

Kang, S., Hong, S. I., Kang, S., Song, M., Yang, M. A., Essa, H., Baker, M., Lee, J., Bruce, R. A., Lee, S. W., & Choi, D. S. (2023). Astrocyte activities in the external globus pallidus regulate action-selection strategies in reward-seeking behaviors. Science advances, 9(24), eadh9239.

Kapp, B. S., Whalen, P. J., Supple, W. F., & Pascoe, J. P. (1992). Amygdaloid contributions to conditioned arousal and sensory information processing. In J. P. Aggleton (Ed.),

The amygdala: Neurobiological aspects of emotion, memory, and mental dysfunction (pp. 229–254).

Kappers, C. U. A., Huber, G. C., & Crosby, E. C. (1936). The comparative anatomy of the nervous system of vertebrates, including man. (2 Vols.). Macmillan.

Khalaf, O., Resch, S., Dixsaut, L., Gorden, V., Glauser, L., & Gräff, J. (2018). Reactivation of recall-induced neurons contributes to remote fear memory attenuation. Science, 360(6394), 1239–1242.

Kol, A., Adamsky, A., Groysman, M., Kreisel, T., London, M., & Goshen, I. (2020). Astrocytes Contribute to Remote Memory Formation by Modulating Hippocampal-Cortical Communication During Learning. Nature neuroscience, 23(10), 1229.

Kim, J. J., & Fanselow, M. S. (1992). Modality-specific retrograde amnesia of fear. Science, 256(5057), 675–677.

Kim, J., Pignatelli, M., Xu, S., Itohara, S., & Tonegawa, S. (2016). Antagonistic negative and positive neurons of the basolateral amygdala. Nature neuroscience, 19(12), 1636.

Kim, J., Zhang, X., Muralidhar, S., LeBlanc, S. A., & Tonegawa, S. (2017). Basolateral to Central Amygdala Neural Circuits for Appetitive Behaviors. Neuron, 93(6), 1464–1479.e5.

Kim, W. B., & Cho, J. H. (2020). Encoding of contextual fear memory in hippocampal-amygdala circuit. Nature communications, 11(1), 1382.

Kitamura, T., Ogawa, S.K., Roy, D.S., Okuyama, T., Morrissey, M.D., Smith, L.M., Redondo, R.L., and Tonegawa, S. (2017). Engrams and circuits crucial for systems consolidation of a memory. Science, 356, 73–78. 10.1126/science.aam6808.

Kjelstrup, K. B., Solstad, T., Brun, V. H., Hafting, T., Leutgeb, S., Witter, M. P., Moser, E. I., & Moser, M. B. (2008). Finite scale of spatial representation in the hippocampus. Science, 321(5885), 140–143.

Klüver, H., & Bucy, P. C. (1937). "Psychic blindness" and other symptoms following bilateral temporal lobectomy in Rhesus monkeys. American journal of physiology, 119, 352–353.

Koizumi, S., Fujishita, K., & Inoue, K. (2005). Regulation of cell-to-cell communication mediated by astrocytic ATP in the CNS. Purinergic signaling, 1(3), 211-217.

Kol, A., Adamsky, A., Groysman, M., Kreisel, T., London, M., and Goshen, I. (2020). Astrocytes contribute to remote memory formation by modulating hippocampal-cortical communication during learning. Nature neuroscience, 23, 1229–1239. 10.1038/s41593-020-0679-6.

LaBar, K. S., Gatenby, J. C., Gore, J. C., LeDoux, J. E., & Phelps, E. A. (1998). Human amygdala activation during conditioned fear acquisition and extinction: a mixed-trial fMRI study. Neuron, 20(5), 937–945.

Lacagnina, A. F., Brockway, E. T., Crovetti, C. R., Shue, F., McCarty, M. J., Sattler, K. P., Lim, S. C., Santos, S. L., Denny, C. A., & Drew, M. R. (2019). Distinct hippocampal engrams control extinction and relapse of fear memory. Nature neuroscience, 22(5), 753–761.

Lashley, K. S., & Franz, S. I. (1917). The Effects of Cerebral Destruction Upon Habit-Formation and Retention in the Albino Rat. Psychobiology, 1(2), 71–139.

Lashley, K. S. (1950). In search of the engram. In Society for Experimental Biology, Physiological mechanisms in animal behavior. (Society's Symposium IV.) (pp. 454–482). Academic Press.

LeDoux, J. E., Iwata, J., Cicchetti, P., & Reis, D. J. (1988). Different projections of the central amygdaloid nucleus mediate autonomic and behavioral correlates of conditioned fear. The Journal of neuroscience: the official journal of the Society for Neuroscience, 8(7), 2517–2529.

LeDoux, J. E., Cicchetti, P., Xagoraris, A., & Romanski, L. M. (1990). The lateral amygdaloid nucleus: sensory interface of the amygdala in fear conditioning. The Journal of neuroscience: the official journal of the Society for Neuroscience, 10(4), 1062–1069.

LeDoux, J. E. (1992). Emotion and the amygdala. In J. P. Aggleton (Ed.), The amygdala: Neurobiological aspects of emotion, memory, and mental dysfunction (pp. 339–351)

LeDoux J. E. (2000). Emotion circuits in the brain. Annual review of neuroscience, 23, 155–184.

Lee, J. H., Kim, W. B., Park, E. H., & Cho, J. H. (2023). Neocortical synaptic engrams for remote contextual memories. Nature neuroscience, 26(2), 259–273.

Lee, J., Yun, M., Cho, E., Lee, J.W., Lee, D., and Jung, M.W. (2019). Transient effect of mossy fiber stimulation on spatial firing of CA3 neurons. Hippocampus 29, 639–651. 10.1002/hipo.23066.

Lei, Z., Xie, L., Li, C. H., Lam, Y. Y., Ramkrishnan, A. S., Fu, Z., Zeng, X., Liu, S., Iqbal, Z., & Li, Y. (2022). Chemogenetic Activation of Astrocytes in the Basolateral Amygdala Contributes to Fear Memory Formation by Modulating the Amygdala & Prefrontal Cortex Communication. International Journal of Molecular Sciences 2022, Vol. 23, Page 6092, 23(11), 6092.

Lein, E. S., Hawrylycz, M. J., Ao, N., Ayres, M., Bensinger, A., Bernard, A., Boe, A. F., Boguski, M. S., Brockway, K. S., Byrnes, E. J., Chen, L., Chen, L., Chen, T. M., Chin, M. C., Chong, J., Crook, B. E., Czaplinska, A., Dang, C. N., Datta, S., Dee, N. R., … Jones, A. R. (2007). Genome-wide atlas of gene expression in the adult mouse brain. Nature, 445(7124), 168–176.

Leonardo, E. D., Richardson-Jones, J. W., Sibille, E., Kottman, A., & Hen, R. (2006). Molecular heterogeneity along the dorsal-ventral axis of the murine hippocampal

CA1 field: a microarray analysis of gene expression. Neuroscience, 137(1), 177–186.

Leutgeb, J. K., Leutgeb, S., Moser, M. B., & Moser, E. I. (2007). Pattern separation in the dentate gyrus and CA3 of the hippocampus. Science, 315(5814), 961–966.

Levy, W. B. (1989). A computational approach to hippocampal function. In Psychology of learning and motivation (Vol. 23, pp. 243-305). Academic Press.

Li, Y., Li, L., Wu, J., Zhu, Z., Feng, X., Qin, L., Zhu, Y., Sun, L., Liu, Y., Qiu, Z., Duan, S., & Yu, Y. Q. (2020). Activation of astrocytes in the hippocampus decreases fear memory through adenosine A1 receptors. ELife, 9, 1–25.

Liao, Z., Tao, Y., Guo, X., Cheng, D., Wang, F., Liu, X., & Ma, L. (2017). Fear conditioning downregulates rac1 activity in the basolateral amygdala astrocytes to facilitate the formation of fear memory. Frontiers in molecular neuroscience, 10, 396.

Liberzon, I., & Sripada, C. S. (2008). The functional neuroanatomy of PTSD: a critical review. Progress in brain research, 167, 151–169.

Lin, Z., You, F., Li, T., Feng, Y., Zhao, X., Yang, J., Yao, Z., Gao, Y., & Chen, J. F. (2022). Entrainment of Astrocytic and Neuronal Ca2+ Population Dynamics During Information Processing of Working Memory in Mice. Neuroscience bulletin, 38(5), 474–488.

Lines, J., Martin, E. D., Kofuji, P., Aguilar, J., & Araque, A. (2020). Astrocytes modulate sensory-evoked neuronal network activity. Nature communications, 2020 11:1, 11(1), 1–12.

Lines, J., Baraibar, A. M., Nanclares, C., Martin, E., Aguilar, J. L. R., Kofuji, P., Navarrete, M., & Araque, A. (2023). A spatial threshold for astrocyte calcium surge. Biorxiv: the preprint server for biology, 2023.07.18.549563.

Lipton, P. A., & Eichenbaum, H. (2008). Complementary roles of hippocampus and medial entorhinal cortex in episodic memory. Neural plasticity, 2008, 258467.

Liu, S., Wong, H. Y., Xie, L., Iqbal, Z., Lei, Z., Fu, Z., Lam, Y. Y., Ramkrishnan, A. S., & Li, Y. (2022). Astrocytes in CA1 modulate schema establishment in the hippocampal-cortical neuron network. BMC biology, 20(1), 250.

Liu, X., Ramirez, S., Pang, P.T., Puryear, C.B., Govindarajan, A., Deisseroth, K., and Tonegawa, S. (2012). Optogenetic stimulation of a hippocampal engram activates fear memory recall. Nature, 484, 381–385. 10.1038/nature11028.

Liu, J., Totty, M. S., Melissari, L., Bayer, H., & Maren, S. (2022). Convergent Coding of Recent and Remote Fear Memory in the Basolateral Amygdala. Biological psychiatry, 91(9), 832–840.

Lopes, G., Bonacchi, N., Frazão, J., Neto, J.P., Atallah, B.V., Soares, S., Moreira, L., Matias, S., Itskov, P.M., Correia, P.A., et al. (2015). Bonsai: an event-based

framework for processing and controlling data streams. Frontiers in neuroinform. 9, 7. 10.3389/fninf.2015.00007.

Luo, R., Zhou, B., Liao, P., Zuo, Y., & Jiang, R. (2023). Disrupting cortical astrocyte Ca2+ signaling in developing brain induces social deficits and depressive-like behaviors. Glia, 71(7), 1592–1606.

Maguire, E. A., Gadian, D. G., Johnsrude, I. S., Good, C. D., Ashburner, J., Frackowiak, R. S., & Frith, C. D. (2000). Navigation-related structural change in the hippocampi of taxi drivers. Proceedings of the National Academy of Sciences of the United States of America, 97(8), 4398–4403.

Malenka, R. C., & Nicoll, R. A. (1993). NMDA-receptor-dependent synaptic plasticity: multiple forms and mechanisms. Trends in neurosciences, 16(12), 521–527.

Maren, S., Poremba, A., & Gabriel, M. (1991). Basolateral amygdaloid multi-unit neuronal correlates of discriminative avoidance learning in rabbits. Brain research, 549(2), 311–316.

Maren, S., & Fanselow, M. S. (1995). Synaptic plasticity in the basolateral amygdala induced by hippocampal formation stimulation in vivo. The Journal of neuroscience: the official journal of the Society for Neuroscience, 15(11), 7548–7564.

Maren, S., Aharonov, G., & Fanselow, M. S. (1996). Retrograde abolition of conditional fear after excitotoxic lesions in the basolateral amygdala of rats: Absence of a temporal gradient. Behavioral neuroscience, 110(4), 718–726.

Maren, S., Aharonov, G., Stote, D. L., & Fanselow, M. S. (1996). N-methyl-D-aspartate receptors in the basolateral amygdala are required for both acquisition and expression of conditional fear in rats. Behavioral neuroscience, 110(6), 1365–1374

Maren, S., Aharonov, G., & Fanselow, M. S. (1997). Neurotoxic lesions of the dorsal hippocampus and Pavlovian fear conditioning in rats. Behavioral brain research, 88(2), 261–274.

Maren, S. (1999). Neurotoxic Basolateral Amygdala Lesions Impair Learning and Memory But Not the Performance of Conditional Fear in Rats. The Journal of neuroscience: the official journal of the Society for Neuroscience, 19(19), 8696–8703.

Maren S. (2000). Auditory fear conditioning increases CS-elicited spike firing in lateral amygdala neurons even after extensive overtraining. The European journal of neuroscience, 12(11), 4047–4054.

Maren S. (2001). Neurobiology of Pavlovian fear conditioning. Annual review of neuroscience, 24, 897–931.

Maren, S., & Holt, W. G. (2004). Hippocampus and Pavlovian fear conditioning in rats: muscimol infusions into the ventral, but not dorsal, hippocampus impair the

acquisition of conditional freezing to an auditory conditional stimulus. Behavioral neuroscience, 118(1), 97–110.

Maren, S., & Quirk, G. J. (2004). Neuronal signalling of fear memory. Nature reviews. Neuroscience, 5(11), 844–852.

Marr, D. (1971). Simple memory: a theory for archicortex. Philosophical transactions of the Royal Society of London. Series B, Biological sciences, 262(841), 23–81.

Martin-Fernandez, M., Jamison, S., Robin, L. M., Zhao, Z., Martin, E. D., Aguilar, J., Benneyworth, M. A., Marsicano, G., & Araque, A. (2017). Synapse-specific astrocyte gating of amygdala-related behavior. Nature neuroscience, 20(11), 1540.

Mathis, A., Mamidanna, P., Cury, K. M., Abe, T., Murthy, V. N., Mathis, M. W., & Bethge, M. (2018). DeepLabCut: markerless pose estimation of user-defined body parts with deep learning. Nature neuroscience, 21(9), 1281–1289.

Mau, W., Sullivan, D. W., Kinsky, N. R., Hasselmo, M. E., Howard, M. W., & Eichenbaum, H. (2018). The Same Hippocampal CA1 Population Simultaneously Codes Temporal Information over Multiple Timescales. Current biology: CB, 28(10), 1499–1508.e4.

McCullagh, P., and Nelder, J.A. (1989). Generalized Linear Models, Second Edition (CRC Press).

McHugh, S. B., Deacon, R. M., Rawlins, J. N., & Bannerman, D. M. (2004). Amygdala and ventral hippocampus contribute differentially to mechanisms of fear and anxiety. Behavioral neuroscience, 118(1), 63–78.

McNaughton, B. L., & Morris, R. G. (1987). Hippocampal synaptic enhancement and information storage within a distributed memory system. Trends in neurosciences, 10(10), 408–415.

McNaughton, B. L., Battaglia, F. P., Jensen, O., Moser, E. I., & Moser, M. B. (2006). Path integration and the neural basis of the 'cognitive map'. Nature reviews neuroscience, 7(8), 663–678.

Mederos, S., Hernández-Vivanco, A., Ramírez-Franco, J., Martín-Fernández, M., Navarrete, M., Yang, A., Boyden, E. S., & Perea, G. (2019). Melanopsin for precise optogenetic activation of astrocyte-neuron networks. Glia, 67(5), 915–934.

Mocle, A. J., Ramsaran, A. I., Jacob, A. D., Rashid, A. J., Luchetti, A., Tran, L. M., Richards, B. A., Frankland, P. W., & Josselyn, S. A. (2024). Excitability mediates allocation of pre-configured ensembles to a hippocampal engram supporting contextual conditioned threat in mice. Neuron, S0896-6273(24)00091-6.

Morris, J. S., Ohman, A., & Dolan, R. J. (1998). Conscious and unconscious emotional learning in the human amygdala. Nature, 393(6684), 467–470.

Moser, M. B., & Moser, E. I. (1998). Functional differentiation in the hippocampus. Hippocampus, 8(6), 608–619.

Moser, E., Moser, M. B., & Andersen, P. (1993). Spatial learning impairment parallels the magnitude of dorsal hippocampal lesions, but is hardly present following ventral lesions. The Journal of neuroscience: the official journal of the Society for Neuroscience, 13(9), 3916–3925.

Moser, M. B., Rowland, D. C., & Moser, E. I. (2015). Place cells, grid cells, and memory. Cold Spring Harbor perspectives in biology, 7(2), a021808.

Nabavi, S., Fox, R., Proulx, C. D., Lin, J. Y., Tsien, R. Y., & Malinow, R. (2014). Engineering a memory with LTD and LTP. Nature, 511(7509), 348–352.

Nagai, J., Rajbhandari, A. K., Gangwani, M. R., Hachisuka, A., Coppola, G., Masmanidis, S. C., Fanselow, M. S., & Khakh, B. S. (2019). Hyperactivity with Disrupted Attention by Activation of an Astrocyte Synaptogenic Cue. Cell, 177(5), 1280–1292.e20.

Nagai, J., Bellafard, A., Qu, Z., Yu, X., Ollivier, M., Gangwani, M. R., Diaz-Castro, B., Coppola, G., Schumacher, S. M., Golshani, P., Gradinaru, V., & Khakh, B. S. (2021). Specific and behaviorally consequential astrocyte Gq GPCR signaling attenuation in vivo with iβARK. Neuron, 109(14), 2256–2274.e9.

Nagel, G., Szellas, T., Huhn, W., Kateriya, S., Adeishvili, N., Berthold, P., Ollig, D., Hegemann, P., & Bamberg, E. (2003). Channelrhodopsin-2, a directly light-gated cation-selective membrane channel. Proceedings of the National Academy of Sciences of the United States of America, 100(24), 13940–13945.

Nam, M. H., Han, K. S., Lee, J., Won, W., Koh, W., Bae, J. Y., Woo, J., Kim, J., Kwong, E., Choi, T. Y., Chun, H., Lee, S. E., Kim, S. B., Park, K. D., Choi, S. Y., Bae, Y. C., & Lee, C. J. (2019). Activation of Astrocytic μ-Opioid Receptor Causes Conditioned Place Preference. Cell reports, 28(5), 1154–1166.e5.

Navarrete, M., & Araque, A. (2010). Endocannabinoids potentiate synaptic transmission through stimulation of astrocytes. Neuron, 68(1), 113–126.

Navarrete, M., Perea, G., Fernandez de Sevilla, D., Gómez-Gonzalo, M., Núñez, A., Martín, E. D., & Araque, A. (2012). Astrocytes mediate in vivo cholinergic-induced synaptic plasticity. PLoS biology, 10(2), e1001259.

Nguyen, R., Koukoutselos, K., Forro, T., & Ciocchi, S. (2023). Fear extinction relies on ventral hippocampal safety codes shaped by the amygdala. Science advances, 9(22), eadg4881.

Ohkawa, N., Saitoh, Y., Suzuki, A., Tsujimura, S., Murayama, E., Kosugi, S., Nishizono, H., Matsuo, M., Takahashi, Y., Nagase, M., Sugimura, Y. K., Watabe, A. M., Kato, F., & Inokuchi, K. (2015). Artificial association of pre-stored information to generate a qualitatively new memory. Cell reports, 11(2), 261–269.

O'Keefe J. (1976). Place units in the hippocampus of the freely moving rat. Experimental neurology, 51(1), 78–109.

O'Keefe, J., & Dostrovsky, J. (1971). The hippocampus as a spatial map. Preliminary evidence from unit activity in the freely-moving rat. Brain research, 34(1), 171–175.

O'Keefe, J., & Speakman, A. (1987). Single unit activity in the rat hippocampus during a spatial memory task. Experimental brain research, 68(1), 1–27.

Okuyama, T., Kitamura, T., Roy, D. S., Itohara, S., & Tonegawa, S. (2016). Ventral CA1 neurons store social memory. Science, 353(6307), 1536–1541.

Opalka, A. N., Huang, W. Q., Liu, J., Liang, H., & Wang, D. V. (2020). Hippocampal Ripple Coordinates Retrosplenial Inhibitory Neurons during Slow-Wave Sleep. Cell reports, 30(2), 432–441.e3.

Orsini, C. A., Kim, J. H., Knapska, E., & Maren, S. (2011). Hippocampal and prefrontal projections to the basal amygdala mediate contextual regulation of fear after extinction. The Journal of neuroscience: the official journal of the Society for Neuroscience, 31(47), 17269–17277.

Pan, S., Mayoral, S.R., Choi, H.S., Chan, J.R., and Kheirbek, M.A. (2020). Preservation of a remote fear memory requires new myelin formation. Nature neuroscience, 23, 487–499. 10.1038/s41593-019-0582-1.

Papouin, T., Ladépêche, L., Ruel, J., Sacchi, S., Labasque, M., Hanini, M., Groc, L., Pollegioni, L., Mothet, J. P., & Oliet, S. H. (2012). Synaptic and extrasynaptic

NMDA receptors are gated by different endogenous coagonists. Cell, 150(3), 633–646.

Papouin, T., Henneberger, C., Rusakov, D. A., & Oliet, S. H. R. (2017). Astroglial versus Neuronal D-Serine: Fact Checking. Trends in neurosciences, 40(9), 517–520.

Park, S., Kramer, E. E., Mercaldo, V., Rashid, A. J., Insel, N., Frankland, P. W., & Josselyn, S. A. (2016). Neuronal Allocation to a Hippocampal Engram. Neuropsychopharmacology: official publication of the American College of Neuropsychopharmacology, 41(13), 2987–2993.

Parpura, V., Basarsky, T. A., Liu, F., Jeftinija, K., Jeftinija, S., & Haydon, P. G. (1994). Glutamate-mediated astrocyte-neuron signaling. Nature, 369(6483), 744–747.

Pascual, O., Casper, K. B., Kubera, C., Zhang, J., Revilla-Sanchez, R., Sul, J. Y., Takano, H., Moss, S. J., McCarthy, K., & Haydon, P. G. (2005). Astrocytic purinergic signaling coordinates synaptic networks. Science, 310(5745), 113–116.

Pelluru, D., Konadhode, R. R., Bhat, N. R., & Shiromani, P. J. (2016). Optogenetic stimulation of astrocytes in the posterior hypothalamus increases sleep at night in C57BL/6J mice. The European journal of neuroscience, 43(10), 1298–1306.

Penfield, W., & Perot, P. (1963). The brain’s record of auditory and visual experience. A final summary and discussion. Brain: a journal of neurology, 86, 595–696.

Peng, W., Liu, X., Ma, G., Wu, Z., Wang, Z., Fei, X., Qin, M., Wang, L., Li, Y., Zhang, S., & Xu, M. (2023). Adenosine-independent regulation of the sleep-wake cycle by astrocyte activity. Cell discovery, 9(1), 16.

Penzo, M. A., Robert, V., Tucciarone, J., De Bundel, D., Wang, M., Van Aelst, L., Darvas, M., Parada, L. F., Palmiter, R. D., He, M., Huang, Z. J., & Li, B. (2015). The paraventricular thalamus controls a central amygdala fear circuit. Nature, 519(7544), 455–459.

Perea, G., & Araque, A. (2005). Glial calcium signaling and neuron–glia communication. Cell calcium, 38(3–4), 375–382.

Perea, G., Navarrete, M., & Araque, A. (2009). Tripartite synapses: astrocytes process and control synaptic information. Trends in neurosciences, 32(8), 421–431.

Petravicz, J., Boyt, K. M., & McCarthy, K. D. (2014). Astrocyte IP3R2-dependent Ca(2+) signaling is not a major modulator of neuronal pathways governing behavior. Frontiers in behavioral neuroscience, 8, 384.

Petravicz, J., Fiacco, T. A., & McCarthy, K. D. (2008). Loss of IP3 receptor-dependent Ca2+ increases in hippocampal astrocytes does not affect baseline CA1 pyramidal neuron synaptic activity. The Journal of neuroscience: the official journal of the Society for Neuroscience, 28(19), 4967–4973.

Phillips, R. G., & LeDoux, J. E. (1992). Differential contribution of amygdala and hippocampus to cued and contextual fear conditioning. Behavioral neuroscience, 106(2), 274–285.

Pinto-Duarte, A., Roberts, A. J., Ouyang, K., & Sejnowski, T. J. (2019). Impairments in remote memory caused by the lack of Type 2 IP3 receptors. Glia, 67(10), 1976–1989.

Pitkänen, A., Pikkarainen, M., Nurminen, N., & Ylinen, A. (2000). Reciprocal connections between the amygdala and the hippocampal formation, perirhinal cortex, and postrhinal cortex in rat. A review. Annals of the New York Academy of Sciences, 911, 369–391.

Pitkänen, A., Savander, V., & LeDoux, J. E. (1997). Organization of intra-amygdaloid circuitries in the rat: an emerging framework for understanding functions of the amygdala. Trends in neurosciences, 20(11), 517–523.

Polykretis, I., & Michmizos, K. P. (2022). The role of astrocytes in place cell formation: A computational modeling study. Journal of computational neuroscience, 50(4), 505–518.

Polyn, S. M., Natu, V. S., Cohen, J. D., & Norman, K. A. (2005). Category-specific cortical activity precedes retrieval during memory search. Science, 310(5756), 1963–1966.

Porter, J.T., and McCarthy, K.D. (1996). Hippocampal astrocytes in situ respond to glutamate released from synaptic terminals. The Journal of neuroscience: the

official journal of the Society for Neuroscience, 16, 5073–5081. 10.1523/JNEUROSCI.16-16-05073.1996.

Porter, J. T., & McCarthy, K. D. (1997). Astrocytic neurotransmitter receptors in situ and in vivo. Progress in neurobiology, 51(4), 439–455.

Poskanzer, K. E., & Yuste, R. (2016). Astrocytes regulate cortical state switching in vivo. Proceedings of the National Academy of Sciences of the United States of America, 113(19), E2675–E2684.

Pothuizen, H. H., Zhang, W. N., Jongen-Rêlo, A. L., Feldon, J., & Yee, B. K. (2004). Dissociation of function between the dorsal and the ventral hippocampus in spatial learning abilities of the rat: a within-subject, within-task comparison of reference and working spatial memory. The European journal of neuroscience, 19(3), 705–712.

Power, S.D., Stewart, E., Zielke, L.G., Byrne, E.P., Douglas, A., Ortega-de San Luis, C., Lynch, L., and Ryan, T.J. (2023). Immune activation state modulates infant engram expression across development. Sciences advances, 9, eadg9921. 10.1126/sciadv.adg9921.

Pratt, W. E., & Mizumori, S. J. (1998). Characteristics of basolateral amygdala neuronal firing on a spatial memory task involving differential reward. Behavioral neuroscience, 112(3), 554–570.

Pryce CR (2018) Comparative evidence for the importance of the amygdala in regulating reward salience. Current opinions behavioral science, 22:76–81.

Qin, H., He, W., Yang, C., Li, J., Jian, T., Liang, S., Chen, T., Feng, H., Chen, X., Liao, X., & Zhang, K. (2020). Monitoring Astrocytic Ca2+ Activity in Freely Behaving Mice. Frontiers in cellular neuroscience, 14, 603095.

Quirk, G. J., Repa, C., & LeDoux, J. E. (1995). Fear conditioning enhances short-latency auditory responses of lateral amygdala neurons: parallel recordings in the freely behaving rat. Neuron, 15(5), 1029–1039.

Quirk, G. J., & Mueller, D. (2008). Neural mechanisms of extinction learning and retrieval. Neuropsychopharmacology : official publication of the American College of Neuropsychopharmacology, 33(1), 56–72.

Rahsepar, B., Norman, J.F., Noueihed, J., Lahner, B., Quick, M.H., Ghaemi, K., Pandya, A., Fernandez, F.R., Ramirez, S., and White, J.A. (2023). Theta-phase-specific modulation of dentate gyrus memory neurons. ELife 12. 10.7554/eLife.82697.

Ramirez, S., Liu, X., Lin, P.-A., Suh, J., Pignatelli, M., Redondo, R.L., Ryan, T.J., and Tonegawa, S. (2013).Creating a false memory in the hippocampus. Science, 341, 387–391. 10.1126/science.1239073.

Ramirez, S., Liu, X., MacDonald, C.J., Moffa, A., Zhou, J., Redondo, R.L., and Tonegawa, S. (2015). Activating positive memory engrams suppresses depression-like behaviour. Nature, 522, 335–339. 10.1038/nature14514.

Rashid AJ, Yan C, Mercaldo V, Hsiang HL, Park S, Cole CJ, De Cristofaro A, Yu J, Ramakrishnan C, Lee SY, Deisseroth K, Frankland PW, Josselyn SA (2016) Competition between engrams influences fear memory formation and recall. Science, 353:383–387.

Redondo, R.L., Kim, J., Arons, A.L., Ramirez, S., Liu, X., and Tonegawa, S. (2014). Bidirectional switch of the valence associated with a hippocampal contextual memory engram. Nature, 513, 426–430. 10.1038/nature13725.

Reijmers, L.G., Perkins, B.L., Matsuo, N., and Mayford, M. (2007). Localization of a Stable Neural Correlate of Associative Memory. Science, 317, 1230–1233. 10.1126/science.1143839.

Repa, J. C., Muller, J., Apergis, J., Desrochers, T. M., Zhou, Y., & LeDoux, J. E. (2001). Two different lateral amygdala cell populations contribute to the initiation and storage of memory. Nature neuroscience, 4(7), 724–731.

Ressler, K. J., Mercer, K. B., Bradley, B., Jovanovic, T., Mahan, A., Kerley, K., Norrholm, S. D., Kilaru, V., Smith, A. K., Myers, A. J., Ramirez, M., Engel, A., Hammack, S. E., Toufexis, D., Braas, K. M., Binder, E. B., & May, V. (2011). Post-traumatic stress disorder is associated with PACAP and the PAC1 receptor. Nature, 470(7335), 492–497.

Risold, P. Y., & Swanson, L. W. (1996). Structural evidence for functional domains in the rat hippocampus. Science, 272(5267), 1484–1486.

Romanski, L. M., Clugnet, M. C., Bordi, F., & LeDoux, J. E. (1993). Somatosensory and auditory convergence in the lateral nucleus of the amygdala. Behavioral neuroscience, 107(3), 444–450.

Roozendaal, B., McEwen, B. S., & Chattarji, S. (2009). Stress, memory and the amygdala. Nature reviews neuroscience, 10(6), 423–433.

Roth B. L. (2016). DREADDs for Neuroscientists. Neuron, 89(4), 683–694.

Roy, D.S., Park, Y.-G., Kim, M.E., Zhang, Y., Ogawa, S.K., DiNapoli, N., Gu, X., Cho, J.H., Choi, H., Kamentsky, L., et al. (2022). Brain-wide mapping reveals that engrams for a single memory are distributed across multiple brain regions. Nature communications, 13, 1799. 10.1038/s41467-022-29384-4.

Royer, S., Sirota, A., Patel, J., & Buzsáki, G. (2010). Distinct representations and theta dynamics in dorsal and ventral hippocampus. The Journal of neuroscience : the official journal of the Society for Neuroscience, 30(5), 1777–1787.

Rugg, M. D., Johnson, J. D., Park, H., & Uncapher, M. R. (2008). Encoding-retrieval overlap in human episodic memory: a functional neuroimaging perspective. Progress in brain research, 169, 339–352.

Ryan, T. J., Roy, D. S., Pignatelli, M., Arons, A., & Tonegawa, S. (2015). Memory. Engram cells retain memory under retrograde amnesia. Science, 348(6238), 1007–1013.

Santello, M., Toni, N., & Volterra, A. (2019). Astrocyte function from information processing to cognition and cognitive impairment. Nature neuroscience, 22(2), 154–166.

Sardinha, V. M., Guerra-Gomes, S., Caetano, I., Tavares, G., Martins, M., Reis, J. S., Correia, J. S., Teixeira-Castro, A., Pinto, L., Sousa, N., & Oliveira, J. F. (2017). Astrocytic signaling supports hippocampal-prefrontal theta synchronization and cognitive function. Glia, 65(12), 1944–1960.

Scemes, E., & Spray, D. C. (2003). The astrocytic syncytium. Non-Neuronal Cells of the Nervous System: Function and Dysfunction, 165–179.

Scofield, M. D., Boger, H. A., Smith, R. J., Li, H., Haydon, P. G., & Kalivas, P. W. (2015). Gq-DREADD Selectively Initiates Glial Glutamate Release and Inhibits Cue-induced Cocaine Seeking. Biological psychiatry, 78(7), 441–451.

Scoville, W. B., & Milner, B. (1957). Loss of recent memory after bilateral hippocampal lesions. Journal of Neurology, Neurosurgery & Psychiatry, 20, 11–21.

Sengupta, A., Yau, J. O. Y., Jean-Richard-dit-Bressel, P., Liu, Y., Millan, E. Z., Power, J. M., & McNally, G. P. (2018). Basolateral Amygdala Neurons Maintain Aversive Emotional Salience. The Journal of neuroscience: the official journal of the Society for Neuroscience, 38(12), 3001.

Semon, R. W. (1921). The mneme. G. Allen & Unwin Limited

Semon, R. W. (1923). Mnemic psychology. London: Allen.

Shelkar, G. P., Liu, J., & Dravid, S. M. (2021). Astrocytic NMDA Receptors in the Basolateral Amygdala Contribute to Facilitation of Fear Extinction. International Journal of Neuropsychopharmacology, 24(11), 907–919.

Sheintuch, L., Rubin, A., Brande-Eilat, N., Geva, N., Sadeh, N., Pinchasof, O., & Ziv, Y. (2017). Tracking the Same Neurons across Multiple Days in Ca2+ Imaging Data. Cell reports, 21(4), 1102–1115.

Shigetomi, E., Patel, S., & Khakh, B. S. (2016). Probing the Complexities of Astrocyte Calcium Signaling. Trends in cell biology, 26(4), 300–312.

Squire, L. R. (2009). Memory and brain systems: 1969–2009. The Journal of neuroscience: the official journal of the Society for Neuroscience, 29(41), 12711–12716.

Srinivasan, R., Huang, B. S., Venugopal, S., Johnston, A. D., Chai, H., Zeng, H., Golshani, P., & Khakh, B. S. (2015). Ca(2+) signaling in astrocytes from Ip3r2(-/-) mice in brain slices and during startle responses in vivo. Nature neuroscience, 18(5), 708–717.

Steadman, P.E., Xia, F., Ahmed, M., Mocle, A.J., Penning, A.R.A., Geraghty, A.C., Steenland, H.W., Monje, M., Josselyn, S.A., and Frankland, P.W. (2020). Disruption of Oligodendrogenesis Impairs Memory Consolidation in Adult Mice. Neuron, 105, 150–164.e6. 10.1016/j.neuron.2019.10.013.

Stehberg, J., Moraga-Amaro, R., Salazar, C., Becerra, A., Echeverría, C., Orellana, J. A., Bultynck, G., Ponsaerts, R., Leybaert, L., Simon, F., Sáez, J. C., & Retamal, M. A. (2012). Release of gliotransmitters through astroglial connexin 43 hemichannels is necessary for fear memory consolidation in the basolateral amygdala. The FASEB Journal, 26(9), 3649–3657.

Steinman, M. Q., Gao, V., & Alberini, C. M. (2016). The role of lactate-mediated metabolic coupling between astrocytes and neurons in long-term memory formation. Frontiers in integrative neuroscience, 10(MAR2016), 10.

Stobart, J. L., Ferrari, K. D., Barrett, M. J. P., Stobart, M. J., Looser, Z. J., Saab, A. S., & Weber, B. (2018). Long-term In Vivo Calcium Imaging of Astrocytes Reveals Distinct Cellular Compartment Responses to Sensory Stimulation. Cerebral cortex, 28(1), 184–198.

Strange, B.A., Witter, M.P., Lein, E.S., and Moser, E.I. (2014). Functional organization of the hippocampal longitudinal axis. Nature reviews neuroscience. 15, 655–669. 10.1038/nrn3785.

Sun, X., Bernstein, M.J., Meng, M., Rao, S., Sørensen, A.T., Yao, L., Zhang, X., Anikeeva, P.O., and Lin, Y. (2020). Functionally Distinct Neuronal Ensembles within the Memory Engram. Cell, 181, 410–423.e17. 10.1016/j.cell.2020.02.055.

Suthard, R. L., Senne, R. A., Buzharsky, M. D., Diep, A. H., Pyo, A. Y., & Ramirez, S. (2024). Engram reactivation mimics cellular signatures of fear. Cell reports, 43(3), 113850.

Suthard, R.L., Senne, R.A., Buzharsky, M.D., Pyo, A.Y., Dorst, K.E., Diep, A.H., Cole, R.H., and Ramirez, S. (2023). Basolateral Amygdala Astrocytes Are Engaged by the Acquisition and Expression of a Contextual Fear Memory. The Journal of neuroscience: the official journal of the Society for Neuroscience, 43, 4997–5013. 10.1523/JNEUROSCI.1775-22.2023.

Swanson, L. W., & Cowan, W. M. (1977). An autoradiographic study of the organization of the efferent connections of the hippocampal formation in the rat. The Journal of comparative neurology, 172(1), 49–84.

Takata, N., Mishima, T., Hisatsune, C., Nagai, T., Ebisui, E., Mikoshiba, K., & Hirase, H. (2011). Astrocyte calcium signaling transforms cholinergic modulation to cortical plasticity in vivo. The Journal of neuroscience: the official journal of the Society for Neuroscience, 31(49), 18155–18165.

Takehara-Nishiuchi K. (2021). Neurobiology of systems memory consolidation. The European journal of neuroscience, 54(8), 6850–6863.

Tao, S., Wang, Y., Peng, J., Zhao, Y., He, X., Yu, X., Liu, Q., Jin, S., & Xu, F. (2021). Whole-Brain Mapping the Direct Inputs of Dorsal and Ventral CA1 Projection Neurons. Frontiers in neural circuits, 15, 643230.

Tanaka, M., Shih, P. Y., Gomi, H., Yoshida, T., Nakai, J., Ando, R., Furuichi, T., Mikoshiba, K., Semyanov, A., & Itohara, S. (2013). Astrocytic Ca2+ signals are required for the functional integrity of tripartite synapses. Molecular brain, 6, 6.

Tanaka, K. Z., Pevzner, A., Hamidi, A. B., Nakazawa, Y., Graham, J., & Wiltgen, B. J. (2014). Cortical representations are reinstated by the hippocampus during memory retrieval. Neuron, 84(2), 347–354.

Trouche, S., Perestenko, P. V., van de Ven, G. M., Bratley, C. T., McNamara, C. G., Campo-Urriza, N., Black, S. L., Reijmers, L. G., & Dupret, D. (2016). Recoding a cocaine-place memory engram to a neutral engram in the hippocampus. Nature neuroscience, 19(4), 564–567.

Trouche, S., Koren, V., Doig, N. M., Ellender, T. J., El-Gaby, M., Lopes-Dos-Santos, V., Reeve, H. M., Perestenko, P. V., Garas, F. N., Magill, P. J., Sharott, A., & Dupret, D. (2019). A Hippocampus-Accumbens Tripartite Neuronal Motif Guides Appetitive Memory in Space. Cell, 176(6), 1393–1406.e16.

Tsunematsu, T., Sakata, S., Sanagi, T., Tanaka, K. F., & Matsui, K. (2021). Region-Specific and State-Dependent Astrocyte Ca2+ Dynamics during the Sleep-Wake Cycle in Mice. The Journal of neuroscience: the official journal of the Society for Neuroscience, 41(25), 5440–5452.

Tulving, E. (1972). Episodic and semantic memory. In E. Tulving & W. Donaldson, Organization of memory. Academic Press.

Tulving, Endel (1983). Elements of Episodic Memory. Oxford University Press.

Turner, B. H., Mishkin, M., & Knapp, M. (1980). Organization of the amygdalopetal projections from modality-specific cortical association areas in the monkey. The Journal of comparative neurology, 191(4), 515–543.

Tye, K. M., Prakash, R., Kim, S. Y., Fenno, L. E., Grosenick, L., Zarabi, H., Thompson, K. R., Gradinaru, V., Ramakrishnan, C., & Deisseroth, K. (2011). Amygdala circuitry mediating reversible and bidirectional control of anxiety. Nature, 471(7338), 358–362.

Vaidyanathan, T. V., Collard, M., Yokoyama, S., Reitman, M. E., & Poskanzer, K. E. (2021). Cortical astrocytes independently regulate sleep depth and duration via separate GPCR pathways. eLife, 10, e63329.

Van Den Herrewegen, Y., Sanderson, T. M., Sahu, S., de Bundel, D., Bortolotto, Z. A., & Smolders, I. (2021). Side-by-side comparison of the effects of Gq- and Gi-DREADD-mediated astrocyte modulation on intracellular calcium dynamics and synaptic plasticity in the hippocampal CA1. Molecular brain, 14(1), 1–13.

Viana, J. F., Machado, J. L., Abreu, D. S., Veiga, A., Barsanti, S., Tavares, G., Martins, M., Sardinha, V. M., Guerra-Gomes, S., Domingos, C., Pauletti, A., Wahis, J., Liu, C., Calì, C., Henneberger, C., Holt, M. G., & Oliveira, J. F. (2023). Astrocyte structural heterogeneity in the mouse hippocampus. *Glia*, *71*(7), 1667–1682.

Vogel, J. W., La Joie, R., Grothe, M. J., Diaz-Papkovich, A., Doyle, A., Vachon-Presseau, E., Lepage, C., Vos de Wael, R., Thomas, R. A., Iturria-Medina, Y., Bernhardt, B., Rabinovici, G. D., & Evans, A. C. (2020). A molecular gradient along the longitudinal axis of the human hippocampus informs large-scale behavioral systems. Nature communications, 11(1), 960.

Volterra, A., & Meldolesi, J. (2005). Astrocytes, from brain glue to communication elements: the revolution continues. Nature Reviews Neuroscience 2005 6:8, 6(8), 626–640.

von Bartheld, C. S., Bahney, J., & Herculano-Houzel, S. (2016). The search for true numbers of neurons and glial cells in the human brain: A review of 150 years of cell counting. The Journal of comparative neurology, 524(18), 3865–3895.

Wang, C., Yue, H., Hu, Z., Shen, Y., Ma, J., Li, J., Wang, X.-D., Wang, L., Sun, B., Shi, P., et al. (2020). Microglia mediate forgetting via complement-dependent synaptic elimination. Science, 367, 688–694. 10.1126/science.aaz2288.

Weiskrantz, L. (1956). Behavioral changes associated with ablation of the amygdaloid complex in monkeys. Journal of comparative and physiological psychology, 49(4), 381–391.

Wilson, A., Brooks, D. C., & Bouton, M. E. (1995). The role of the rat hippocampal system in several effects of context in extinction. Behavioral neuroscience, 109(5), 828–836.

Wiltgen, B. J., Sanders, M. J., Anagnostaras, S. G., Sage, J. R., & Fanselow, M. S. (2006). Context fear learning in the absence of the hippocampus. The Journal of neuroscience: the official journal of the Society for Neuroscience, 26(20), 5484–5491.

Witter, M. P., Groenewegen, H. J., Lopes da Silva, F. H., & Lohman, A. H. (1989). Functional organization of the extrinsic and intrinsic circuitry of the parahippocampal region. Progress in neurobiology, 33(3), 161–253.

Yang, L., Lu, J., Guo, J., Chen, J., Xiong, F., Wang, X., Chen, L., & Yu, C. (2022). Ventrolateral Periaqueductal Gray Astrocytes Regulate Nociceptive Sensation and Emotional Motivation in Diabetic Neuropathic Pain. The Journal of neuroscience: the official journal of the Society for Neuroscience, 42(43), 8184–8199.

Yamashita, A., Hamada, A., Suhara, Y., Kawabe, R., Yanase, M., Kuzumaki, N., Narita, M., Matsui, R., Okano, H., & Narita, M. (2014). Astrocytic activation in the anterior cingulate cortex is critical for sleep disorder under neuropathic pain. Synapse, 68(6), 235–247.

Yiu, A. P., Mercaldo, V., Yan, C., Richards, B., Rashid, A. J., Hsiang, H. L., Pressey, J., Mahadevan, V., Tran, M. M., Kushner, S. A., Woodin, M. A., Frankland, P. W., & Josselyn, S. A. (2014). Neurons are recruited to a memory trace based on relative neuronal excitability immediately before training. Neuron, 83(3), 722–735.

Yoshii, T., Hosokawa, H., & Matsuo, N. (2017). Pharmacogenetic reactivation of the original engram evokes an extinguished fear memory. Neuropharmacology, 113(Pt A), 1–9.

Young, S. L., Bohenek, D. L., & Fanselow, M. S. (1994). NMDA processes mediate anterograde amnesia of contextual fear conditioning induced by hippocampal damage: immunization against amnesia by context preexposure. Behavioral neuroscience, 108(1), 19–29.

Yu, X., Nagai, J., Marti-Solano, M., Soto, J. S., Coppola, G., Babu, M. M., & Khakh, B. S. (2020). Context-Specific Striatal Astrocyte Molecular Responses Are Phenotypically Exploitable. Neuron, 108(6), 1146–1162.e10.

Yu, X., Taylor, A. M. W., Nagai, J., Golshani, P., Evans, C. J., Coppola, G., & Khakh, B. S. (2018). Reducing Astrocyte Calcium Signaling In Vivo Alters Striatal Microcircuits and Causes Repetitive Behavior. Neuron, 99(6), 1170–1187.e9.

Zaki, Y., Mau, W., Cincotta, C., Monasterio, A., Odom, E., Doucette, E., Grella, S. L., Merfeld, E., Shpokayte, M., & Ramirez, S. (2022). Hippocampus and amygdala fear memory engrams re-emerge after contextual fear relapse. Neuropsychopharmacology: official publication of the American College of Neuropsychopharmacology, 47(11), 1992–2001.

Zong, W., Obenhaus, H. A., Skytøen, E. R., Eneqvist, H., de Jong, N. L., Vale, R., Jorge, M. R., Moser, M. B., & Moser, E. I. (2022). Large-scale two-photon calcium imaging in freely moving mice. Cell, 185(7), 1240–1256.e30.

Zhang, J. M., Wang, H. K., Ye, C. Q., Ge, W., Chen, Y., Jiang, Z. L., Wu, C. P., Poo, M. M., & Duan, S. (2003). ATP released by astrocytes mediates glutamatergic activity-dependent heterosynaptic suppression. Neuron, 40(5), 971–982.

Zhang, Z. M., Chen, S., & Liang, Y. Z. (2010). Baseline correction using adaptive iteratively reweighted penalized least squares. The Analyst, 135(5), 1138–1146.

Zhang, X., & Li, B. (2018). Population coding of valence in the basolateral amygdala. Nature communications, 2018 9:1, 9(1), 1–14.

Zhang, X., Kim, J., & Tonegawa, S. (2020). Amygdala Reward Neurons Form and Store Fear Extinction Memory. Neuron, 105(6), 1077–1093.e7.

Zhao J, Wang D, Wang JH (2012) Barrel cortical neurons and astrocytes coordinately respond to an increased whisker stimulus frequency. Molecular brain, 5:12.

Zheng, J., Anderson, K. L., Leal, S. L., Shestyuk, A., Gulsen, G., Mnatsakanyan, L., Vadera, S., Hsu, F. P. K., Yassa, M. A., Knight, R. T., & Lin, J. J. (2017). Amygdala-hippocampal dynamics during salient information processing. Nature communications 2017 8:1, 8(1), 1–11.

Zhou, Y., Won, J., Karlsson, M. G., Zhou, M., Rogerson, T., Balaji, J., ... & Silva, A. J. (2009). CREB regulates excitability and the allocation of memory to subsets of neurons in the amygdala. Nature neuroscience, 12(11), 1438-1443.

Zhou, Y., Zhu, H., Liu, Z., Chen, X., Su, X., Ma, C., Tian, Z., Huang, B., Yan, E., Liu, X., & Ma, L. (2019). A ventral CA1 to nucleus accumbens core engram circuit mediates conditioned place preference for cocaine. Nature neuroscience, 22(12), 1986–1999.

**CURRICULUM VITAE**